

Dissertation  
submitted to the  
Combined Faculties for the Natural Science and for  
Mathematics  
of the Ruperto-Carola university of Heidelberg,  
Germany  
for the degree of Doctor of Natural Sciences

Put forward by  
Diplom-Physikerin: Marta Ubieto Díaz  
Born in: Tortosa  
Oral examination: 07.12.2011



**Off-line commissioning of a  
non-destructive FT-ICR detection  
system for monitoring the ion  
concentration in the KATRIN  
beamline**

Referees: Prof. Dr. Klaus Blaum  
PD Dr. Wolfgang Quint



**Zusammenfassung:** Jüngst haben Neutrinooszillationen die Existenz von massiven Neutrinos bewiesen. Seitdem ist die Messung der Ruhemasse der Neutrinos von großem Interesse. Das Ziel des Karlsruher Tritium Neutrino Experiments (KATRIN) ist es, die Ruhemasse des Anti-Elektron-Neutrinos mit einer Empfindlichkeit von 0,2 eV in einem Konfidenzintervall von 95% zu bestimmen. In der Strahlführung von KATRIN werden verschiedene positive Ionen ( $T^+$ ,  $He^+$ ,  $(^3HeT)^+$ ,  $T_2^+$ ) durch  $\beta$ -Zerfall und Ionisationsprozesse gebildet. Nachfolgend bilden sich über chemische Reaktionen  $T_3^+$ ,  $T_5^+$  und größere Cluster. Diese Kontaminationen werden überwiegend innerhalb des Transportabschnitts des Experiments entfernt. Zur Analyse des  $\beta$ -Spektrums müssen die Existenz und die Konzentration dieser Kontaminationen bekannt sein. Zur Identifikation und Messung der Konzentration der Verunreinigungen werden zwei identische Penningfallensysteme, die die Fourier-Transform Ionen-Zyklotron-Resonanz (FT-IZR) Methode anwenden, in der Strahlführung von KATRIN installiert. Der Fokus der vorliegenden Arbeit liegt auf der Offline-Inbetriebnahme dieser Penningfallen. Ein Testaufbau, welcher es ermöglichte, eine dreipolare zylindrische Penningfalle und die zugehörige Elektronik innerhalb eines 4.7-T supraleitenden Magneten zu testen, wurde am Max-Planck-Institut für Kernphysik in Heidelberg entwickelt und in Betrieb genommen. Teil der Charakterisierung sind Messungen der Kohärenzzeit der Ionenbewegung bei verschiedenen Drücken, die Ermittlung der Nachweisgrenze der getesteten Penningfalle und der Elektronik sowie eine Massenmessung zur Bestimmung der mit dieser Penningfalle erreichbaren Genauigkeit.

**Abstract:** Neutrino oscillations have recently proved the existence of massive neutrinos. Since then the measurement of the rest mass of the neutrino remains an open question. The Karlsruhe Tritium Neutrino KATRIN experiment aims to obtain the electron antineutrino rest mass with a sensitivity of 0.2 eV with a confident level of 95%. In the KATRIN beamline various positive ions are formed by  $\beta$ -decay and ionization processes ( $T^+$ ,  $He^+$ ,  $(^3HeT)^+$ ,  $T_2^+$ ), followed by chemical reactions which also produce  $T_3^+$ ,  $T_5^+$  and even larger cluster ions. The partial removal of these contaminations will be done along the transport section of the experiment. The presence and the concentrations of these contaminants have to be known when evaluating the  $\beta$  spectrum. To identify and measure these concentrations two identical Penning trap systems using the Fourier Transform-Ion Cyclotron Resonance (FT-ICR) method will be installed into the KATRIN beamline. The off-line commissioning of these Penning traps is the main topic of the work presented here. A test setup was built at the Max-Planck-Institute for Nuclear Physics in Heidelberg where a 3-pole cylindrical Penning trap and its electronics were tested inside a 4.7-T superconducting magnet. Measurements of the coherence time of the ion motion at different pressures, the detection limit of the tested Penning trap and its electronics, and a mass measurement for the determination of the accuracy of the tested Penning trap system are part of the characterization.

# Contents

<b>1</b>	<b>Introduction and motivation</b>	<b>1</b>
<b>I</b>	<b>Theory</b>	<b>5</b>
<b>2</b>	<b>Penning trap principles</b>	<b>7</b>
2.1	The ideal Penning trap . . . . .	7
2.2	The real Penning trap . . . . .	10
2.2.1	Magnetic field inhomogeneities . . . . .	11
2.2.2	Electric fields imperfections . . . . .	11
2.2.3	Ion-ion interactions . . . . .	11
2.3	Ion excitation methods . . . . .	12
2.3.1	Dipolar excitation . . . . .	12
2.3.2	Quadrupolar excitation . . . . .	13
2.3.3	Broad-band excitation . . . . .	14
2.3.4	Selected-ion-excitation mode . . . . .	14
2.4	Ion cooling techniques . . . . .	15
2.4.1	Buffer gas cooling . . . . .	15
2.4.2	Resistive cooling . . . . .	16
2.4.3	Evaporative cooling . . . . .	17
<b>3</b>	<b>Ion detection techniques</b>	<b>19</b>
3.1	Time-of-flight-ion cyclotron resonance detection . . . . .	19
3.2	Induced image charge detection . . . . .	20
3.2.1	Narrow-band FT-ICR detection . . . . .	21
3.2.2	Broad-band FT-ICR detection . . . . .	23
3.2.3	Dipolar detection . . . . .	23
3.2.4	Quadrupolar detection . . . . .	24
3.2.5	Selected-ion-detection mode . . . . .	24

<b>II Experiment</b>	<b>27</b>
<b>4 The Karlsruhe Tritium Neutrino experiment</b>	<b>29</b>
4.1 The KATRIN experiment . . . . .	29
4.2 Transport section and differential pumping section . . . . .	31
4.3 Expected ion contaminations in the KATRIN beamline . . . . .	32
<b>5 FT-ICR Penning trap setup in Heidelberg</b>	<b>35</b>
5.1 Superconducting magnet . . . . .	35
5.2 Ion production . . . . .	38
5.2.1 Surface ion source . . . . .	39
5.2.2 Electron impact ion source . . . . .	40
5.2.3 Photocathode ion source . . . . .	41
5.3 Ion optics . . . . .	42
5.4 The Penning trap . . . . .	43
5.5 Destructive and non-destructive ion detectors . . . . .	44
5.5.1 Faraday cup . . . . .	44
5.5.2 Microchannel-plate detector . . . . .	46
5.5.3 FT-ICR detector . . . . .	47
5.6 Control system . . . . .	50
5.6.1 Transient recorder control system . . . . .	50
5.6.2 Downconverter control system . . . . .	54
<b>6 Results from the commissioning setup in Heidelberg</b>	<b>57</b>
6.1 Preamplifier and postamplifier tests . . . . .	57
6.2 Excitation and detection scheme . . . . .	58
6.3 Characterization of the FT-ICR signals . . . . .	59
6.4 Magnetic field measurement with trapped ions . . . . .	61
6.5 Coherence time measurements . . . . .	63
6.6 Selected-ion-detection . . . . .	66
6.7 Detection limit for different ion species . . . . .	69
6.8 Mass measurements . . . . .	73
6.9 Residual gas analysis at cryogenic temperatures . . . . .	74
6.10 Conclusion . . . . .	77
<b>7 Future commissioning in KATRIN</b>	<b>79</b>
7.1 Position of the traps . . . . .	79
7.2 Magnetic field at the DPS . . . . .	82
7.3 Cabling . . . . .	82
7.4 Electronics . . . . .	84
7.4.1 Preamplifier . . . . .	84

7.4.2 Postamplifier . . . . .	86
7.5 Status and conclusion . . . . .	87
<b>8 Conclusion and outlook</b>	<b>89</b>



# List of Tables

4.1	Endpoint energies for different tritium decays . . . . .	33
4.2	Possible contaminations at KATRIN . . . . .	34
5.1	MCP specifications . . . . .	48
6.1	Experimental values for $B$ and $d$ . . . . .	63



# List of Figures

1.1	Electron energy spectrum of tritium $\beta$ -decay . . . . .	3
1.2	Overview of the KATRIN experiment . . . . .	3
2.1	Standard electrode configuration of a trap . . . . .	8
2.2	Schematic trajectory of the ion motion . . . . .	10
2.3	Quadrupolar and dipolar excitation with four segments . . . . .	12
2.4	Conversion of the ion motion . . . . .	14
2.5	Quadrupolar excitation with eight segments ring . . . . .	15
2.6	Broad-band excitation sketch . . . . .	16
3.1	Time-of-flight detection principle . . . . .	20
3.2	FT-ICR detection principle . . . . .	22
3.3	FT-ICR detection with four segments . . . . .	23
3.4	FT-ICR detection with eight segments . . . . .	24
4.1	Overview of the KATRIN experiment . . . . .	30
4.2	KATRIN transport section . . . . .	31
5.1	Experimental setup at the MPIK . . . . .	36
5.2	Magnetic field along the $z$ -axis . . . . .	37
5.3	NMR probe measurements . . . . .	38
5.4	Thermionic ion source . . . . .	40
5.5	Axial molecular beam ionizer . . . . .	41
5.6	Test ion source for the KATRIN experiment . . . . .	42
5.7	Triplet lens . . . . .	43
5.8	Front and side view of the Penning trap . . . . .	44
5.9	Faraday cup . . . . .	45
5.10	Quick charge amplifier test circuit . . . . .	46
5.11	Microchannel plate detector . . . . .	47
5.12	Diagram of the preamplifier . . . . .	48
5.13	Pre- and postamplifier . . . . .	50
5.14	Transient recorder control system . . . . .	51

---

5.15	Graphical users interface screenshot . . . . .	52
5.16	Downconverter control system . . . . .	54
5.17	Downconversion principle . . . . .	55
6.1	Amplification of the MPIK electronics . . . . .	58
6.2	Noise tests of the MPIK electronics . . . . .	59
6.3	Timing scheme . . . . .	60
6.4	Characterization of the FT-ICR signals . . . . .	61
6.5	Magnetic field measurement with ${}^4\text{He}^+$ ions . . . . .	62
6.6	Sketch for the coherence time measurements . . . . .	64
6.7	Coherence time at different excitation times . . . . .	65
6.8	Coherence time at low pressures . . . . .	66
6.9	Coherence time at high pressure . . . . .	67
6.10	FT-ICR spectrum for four ion species . . . . .	68
6.11	FT-ICR spectrum for two ion species . . . . .	69
6.12	Detection limit for ${}^4\text{He}^+$ ions . . . . .	70
6.13	Induced amplified signal from the Faraday cup . . . . .	71
6.14	Detection limit for ${}^6\text{Li}^+$ and ${}^7\text{Li}^+$ ions . . . . .	72
6.15	Spectrum for mass measurements . . . . .	74
6.16	Long term $\nu_c$ measurement . . . . .	75
6.17	Scheme of the cryogenic setup . . . . .	76
6.18	Results of the outgassing test . . . . .	77
7.1	Differential pumping section segment . . . . .	80
7.2	Asymmetric trap for the KATRIN experiment . . . . .	81
7.3	Magnetic field at the DPS . . . . .	83
7.4	Transfer function of the coaxial cable from Draka Fileca . . . . .	84
7.5	KATRIN preamplifier amplification . . . . .	85
7.6	KATRIN preamplifier noise . . . . .	86
7.7	KATRIN flange amplifier . . . . .	87

# Chapter 1

## Introduction and motivation

Neutrino physics is a relatively new field of fundamental physics which still has a lot of open questions, one of the most important ones is about the mass of the neutrino.

The existence of neutrinos was postulated for the first time in an open letter by Wolfgang Pauli in 1930 [1]. Pauli introduced this new particle in order to explain the continuous electron spectrum observed in the  $\beta$ -decay

$$n \longrightarrow p + e^- + \bar{\nu}_e. \quad (1.1)$$

Pauli postulated that this unobserved particle emitted in the  $\beta$ -decay process would be neutral, massless, with spin 1/2, and it should interact weakly with matter. The existence of neutrinos was confirmed in 1956 when reactor electron antineutrinos  $\bar{\nu}_e$  were observed by Cowan and Reines [2]. Neutrinos were, at this point, included in the standard model of particle physics as massless, neutral and left-handed spin 1/2 particles [3].

Ever since the neutrino discovery, it has been discussed whether neutrinos are really massless or if they have a small mass which could well explain the missing dark matter in the universe and some other observations showing that there is much more gravitational matter in the universe than what can be identified (e.g. [4]). Although there were theoretical predictions of neutrinos being massive particles and hence undergo oscillations since 1957 [5], it was not until 1998 when the Super-Kamiokande experiment [6] measured the first neutrino oscillations by measuring atmospheric neutrinos, and confirmed that neutrinos are massive. These results were confirmed by measuring solar neutrinos in the Sudbury Neutrino Observatory (SNO) in 2001 [7] and 2002 [8].

Experiments oriented to measure neutrino masses can be divided depending on the used method. Cosmological observations and neutrinoless double  $\beta$ -decay are very sensitive methods for neutrino mass measurements but they

are model-dependent methods. On the other hand, the direct determination of neutrino masses by kinematics is a model-independent method based on energy and momentum conservation.

Nowadays the precise investigation of a  $\beta$ -decay spectrum near its endpoint is the most sensitive method of neutrino mass determination as it was already pointed out by Fermi in 1934 [9]. Almost every neutrino mass measurement experiment based on  $\beta$ -decay studies is done using tritium as  $\beta$ -emitter



The reasons for preferring tritium  $\beta$ -decay for neutrino mass measurements are given in the following [10]:

- The  $\beta$ -spectrometer has better energy resolving power  $E/\Delta E$  at lower endpoint energies. Tritium  $\beta$ -decay has a low  $\beta$ -decay endpoint energy of  $E_0 \approx 18.6$  keV.
- Tritium  $\beta$ -decay has a rather short half-life of 12.3 years in comparison with other possible  $\beta$ -decay emitters such as  ${}^{187}\text{Re}$ , with a half-life of  $4.3 \times 10^{10}$  years.
- Tritium is the simplest molecule allowing quantitative calculation of its final state spectrum.

The signature of an electron neutrino with a mass of  $m(\nu_e) = 1$  eV is shown in figure 1.1 in comparison with the undistorted  $\beta$  spectrum for a massless  $\nu_e$ . The spectral distortion is statistically significant only in the region close to the  $\beta$  endpoint.

Since the study of the tritium  $\beta$ -decay endpoint is used for neutrino mass measurements, a precise measurement of the tritium  $Q$ -value, defined as the mass difference between  ${}^3H$  and  ${}^3He$ , is needed. The first tritium  $Q$ -value measurement using Penning traps was done by Van Dyck *et al.*, obtaining a value of 18 590.1 (1.7) eV [12]. This value was improved at SMILETRAP obtaining a value of 18 589.8 (1.2) eV [13]. An experiment to improve the tritium  $Q$ -value starts operating nowadays at the MPIK. This experiment is an upgraded version of the University of Washington-Penning Trap Mass Spectrometer (UW-PTMS) operated by Van Dyck [14]. This upgraded experiment, known as THe-Trap, plans to measure the  ${}^3H/{}^3He$  mass ratio with an uncertainty below  $10^{-11}$ , which translates into 30 meV of uncertainty for the  $Q$ -value [15].

One of the experiments being built nowadays in order to measure the neutrino rest mass is the **K**Arlsruhe **T**RItium Neutrino experiment (KATRIN) [11]. This experiment is based on the tritium  $\beta$ -decay and it aims to measure

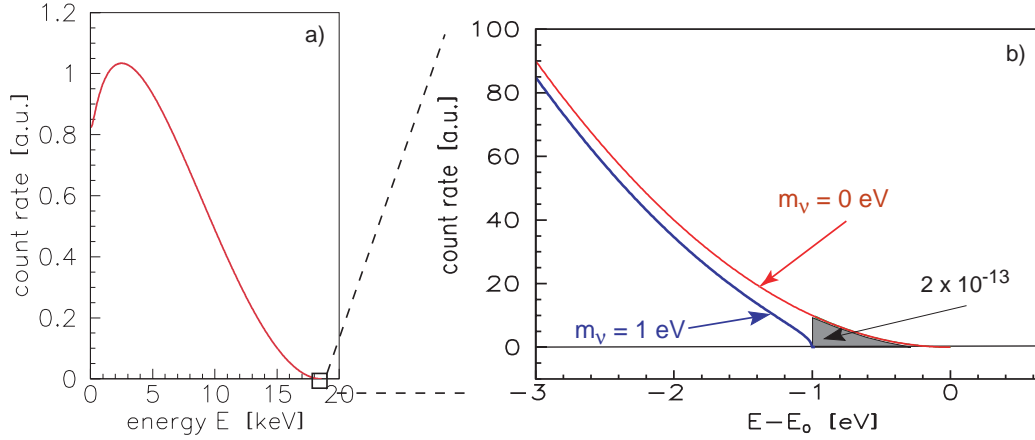


Figure 1.1: The electron energy spectrum of tritium  $\beta$ -decay: (a) complete and (b) narrow region around endpoint  $E_0$ . The expected  $\beta$  spectrum is shown for neutrino masses of 0 and 1 eV. Figure from [11].

the electron antineutrino mass with a sensitivity of  $0.2 \text{ eV}/c^2$  (95% c.l.) [10]. This experiment is based on the Mainz [16] and the Troitsk [17] neutrino mass experiments where, up to now, the most accurate upper limit of the electron antineutrino mass,  $2.0 \text{ eV}/c^2$  (95% c.l.), was measured. A schematic view of the KATRIN experiment can be seen in figure 1.2. It consists of: (1) a gaseous tritium source where the tritium  $\beta$ -decay occurs, (2) a transport section surrounded by superconducting coils used for guiding the  $\beta$ -electrons to the detector, (3) and (4) a tandem spectrometer used for Magnetic Adiabatic Collimation combined with an Electrostatic filter (MAC-E filters) and (5) a particle detector for counting the  $\beta$ -electrons.

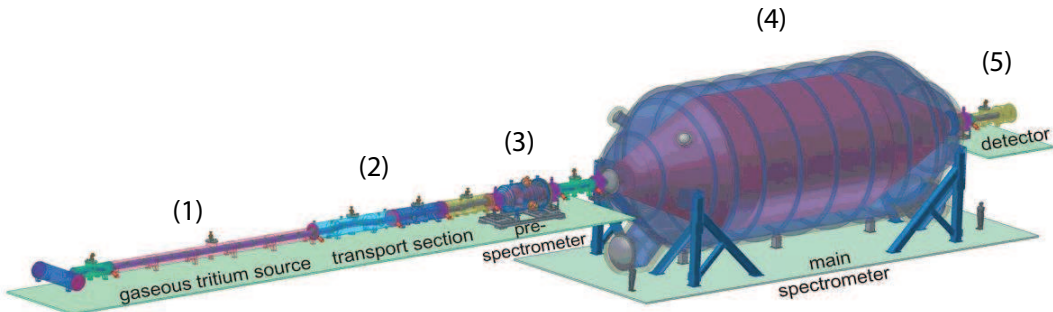


Figure 1.2: Overview of the KATRIN experiment [11].

One source of systematic uncertainties in the KATRIN experiment is the formation of ion clusters when tritium decays and decay products interact

with residual tritium molecules, such as  $T_2^+$  and  $T_3^+$ . These ion species and clusters are considered contaminants in the KATRIN beamline since they have different final state energies than tritium ions. Therefore the monitoring of these contaminants is essential for the final measurements in KATRIN. The removal of these contaminants is one of the main tasks of the transport section (labeled as (2) in figure 1.2). The transport section consists of two different subsections, the Differential Pumping Section (DPS) and the Cryogenic Pumping Section (CPS). The monitoring of the ion concentration is planned to be done with two identical Penning trap spectrometers. One of the Penning traps will be placed at the beginning of the DPS, right after the tritium source, and the other one will be placed at the end of the DPS, right before the CPS. These two Penning traps will be the only on-line monitoring devices in the KATRIN beamline. The Penning traps will be used applying the broad-band Fourier Transform-Ion Cyclotron Resonance (FT-ICR) detection method, in order to monitor simultaneously several ion species inside the KATRIN beamline. For this purpose, a prototype of a cylindrical Penning trap has been constructed and tested at the Max-Planck-Institute for Nuclear Physics in Heidelberg. The geometry of the tested Penning trap fulfills the KATRIN requirements of not to interfere with the  $\beta$ -electron flux. The off-line commissioning of one of these Penning trap systems is the main subject of this thesis.

Chapters 2 and 3 of this thesis will explain the principle of the Penning traps, as well as the possible excitation and detection methods to be applied. An overview of the KATRIN experimental setup and the possible contaminations that could be found in the beamline will be presented in chapter 4. Chapter 5 will explain in detail the experimental setup used for the presented tests, while chapter 6 will show the results obtained in this setup. The Penning trap system is planned to be installed into the KATRIN beamline in 2012, for that reason chapter 7 gives an overview on how the commissioning of the Penning trap systems will proceed. The thesis concludes with an outlook in chapter 8.

# Part I

## Theory



# Chapter 2

## Penning trap principles

Penning traps are well known storage devices used for the confinement of charged particles [18, 19, 20, 21]. The fundamental idea of Penning traps was conceived in the late 30's by F.M. Penning [22], later Hans G. Dehmelt and Wolfgang Paul received the Nobel Prize in 1989 for the development of the ion trap techniques [21, 23]. Penning traps are nowadays powerful tools used for high-accuracy mass measurements. Many facilities all around the world such as ISOLTRAP [24], SHIPTRAP [25] and TRIGA-TRAP [26] use Penning traps for high-precision measurements. The principles of Penning traps will be described in this chapter.

### 2.1 The ideal Penning trap

A moving particle of mass  $m$ , incident velocity  $\vec{v}$  and charge  $q$  in a magnetic field  $B$  is subjected to the Lorentz force  $\vec{F}_L = q\vec{v} \times \vec{B}$ . This causes the particle to move on a circular motion with the well-known cyclotron frequency

$$\nu_c = \frac{qB}{2\pi m}. \quad (2.1)$$

This frequency is the main observable when doing mass measurements in a Penning trap.

Standard ion traps consist of three electrodes; two endcaps and a ring electrode at the center. Figures 2.1(a) and (b) show traps with a hyperboloidal shape, the first one is a so called Paul trap (a complete description of these kind of trapping devices can be found in reference [27]) and the second is a Penning trap where the magnetic field is parallel to the symmetry axis. Figure 2.1(c) shows a Penning trap with cylindrical shape.

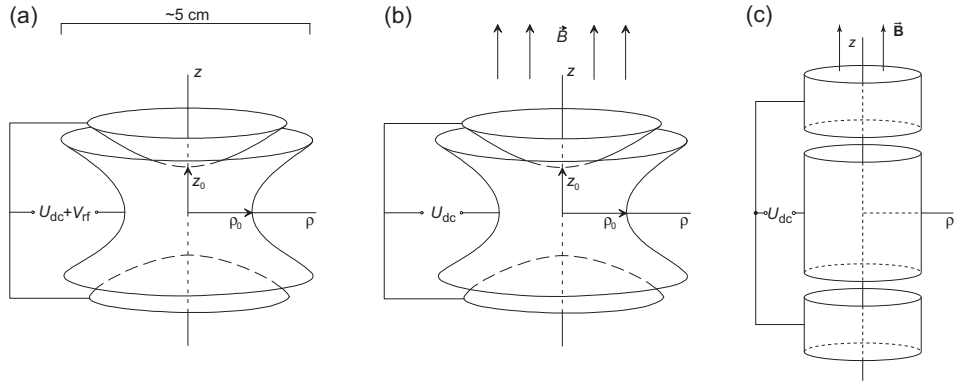


Figure 2.1: Standard electrode configuration of a trap. Panels (a) and (b) show traps with hyperboloidal electrode shape, where (a) sketches a Paul trap and (b) a Penning trap. Panel (c) shows the configuration of a Penning trap with cylindrical shape. Figure from [18].

For the three-dimensional confinement of a charged particle, the superposition of a strong homogeneous magnetic field along the  $z$ -axis, and a weak quadrupole electric field is needed.

The electrostatic quadrupole potential in a hyperbolic Penning trap (figure 2.1(b)) in cylindrical coordinates with  $\rho$  and  $z$  is given by:

$$V(\rho, z) = \frac{U_0}{2d^2}(z^2 - \frac{\rho^2}{2}) \quad (2.2)$$

where  $U_0$  is the trapping potential (potential difference between the ring electrode and the endcap electrodes) and  $d$  is a characteristic parameter of the trap defined by

$$d^2 = \frac{1}{2}(z_0^2 + \frac{\rho_0^2}{2}) \quad (2.3)$$

where  $z_0$  and  $\rho_0$  are given by the minimum distance from the center of the trap to the endcaps and the ring electrode, respectively (see figure 2.1).

The superposition of the electrostatic potential given in equation (2.2) and the homogeneous magnetic field in  $z$  direction leads to the equation of motion for the confined particles:

$$\vec{F} = m\ddot{\vec{r}} = q(\vec{E} + \dot{\vec{r}} \times \vec{B}) = q(-\nabla V + \dot{\vec{r}} \times \vec{B}), \quad (2.4)$$

from where the following three differential equations are deduced

$$\ddot{x} = \frac{qU_0}{2md^2}x + \frac{qB}{m}\dot{y}, \quad (2.5)$$

$$\ddot{y} = \frac{qU_0}{2md^2}y - \frac{qB}{m}\dot{x}, \quad (2.6)$$

$$\ddot{z} = -\frac{qU_0}{md^2}z. \quad (2.7)$$

Equations (2.5)-(2.7) can be combined using the complex variable  $u = x + iy$  to obtain:

$$\ddot{u} + i\omega_c\dot{u} - \frac{1}{2}\omega_z^2u = 0 \quad (2.8)$$

where the cyclotron frequency  $\omega_c$  and the axial frequency  $\omega_z$  are given by the expressions:

$$\omega_c = \frac{qB}{m}, \quad (2.9)$$

$$\omega_z = \sqrt{\frac{qU_0}{md^2}}. \quad (2.10)$$

Solving the equations of motion for all three coordinates the two characteristic eigenfrequencies  $\omega_{\pm}$  can be found:

$$\omega_{\pm} = \frac{1}{2}(\omega_c \pm \sqrt{\omega_c^2 - 2\omega_z^2}). \quad (2.11)$$

These equations show that the motion of a trapped charged particle is a superposition of three eigenmotions: a harmonic motion along the trap axis with the oscillation frequency  $\omega_z$ , a circular cyclotron motion with the modified cyclotron frequency  $\omega_+$ , and a circular motion at the magnetron frequency  $\omega_-$ . A scheme of these three motions can be seen in figure 2.2.

In order to achieve a bound ion motion, the root of equations (2.11) must be real and this leads to the trapping condition

$$\omega_c^2 - 2\omega_z^2 > 0. \quad (2.12)$$

This condition combined with equations (2.9) and (2.10) defines the conditions for a stable confinement of charged particles in a Penning trap as a function of the applied external fields as follows:

$$\frac{|q|}{m}B^2 > \frac{2|U_0|}{d^2}, \quad qU_0 > 0. \quad (2.13)$$

A series expansion of the two radial eigenfrequencies (equations (2.11)) gives two approximations:

$$\omega_- = \frac{U_0}{2d^2B} \quad \text{and} \quad \omega_+ = \omega_c - \frac{U_0}{2d^2B}. \quad (2.14)$$

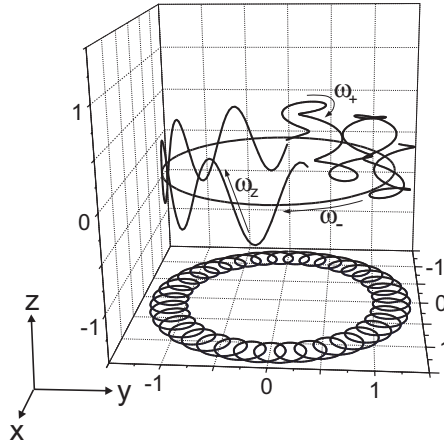


Figure 2.2: Schematic trajectory of the three eigenmotions of an ion confined inside an ideal Penning trap with the magnetic field in the  $z$ -direction [18].

It becomes obvious that the magnetron frequency  $\omega_-$  is mass independent in first order approximation.

The magnitudes of the eigenfrequencies follow the order  $\omega_- < \omega_z < \omega_+$  and fulfill in an ideal trap the conditions:

$$\omega_c = \omega_+ + \omega_- \quad (2.15)$$

$$2\omega_+\omega_- = \omega_z^2 \quad (2.16)$$

$$\omega_c^2 = \omega_+^2 + \omega_-^2 + \omega_z^2. \quad (2.17)$$

The latter is called the *invariance theorem* [28] since this equation holds in first order also for a real trap with *e.g.* field imperfections and misalignments. A review of the principles of the Penning trap technique is given by Brown and Gabrielse in [20].

## 2.2 The real Penning trap

In reality the ion motion described in the previous section deviates from the real ion motion inside a Penning trap. The magnetic field inhomogeneities, the electric field imperfections and the ion-ion interactions, among others, produce a shift in the measured frequency and thus in the measured mass. The most important causes of the shifts will be discussed in the following.

### 2.2.1 Magnetic field inhomogeneities

The magnetic field instabilities and imperfections could be considered the biggest source of uncertainties nowadays in the field of high-accuracy mass spectrometry. The magnetic field created from a superconducting magnet can fluctuate due to several reasons.

Due to the flux creep phenomenon [29, 30] the current in the coils of the magnet decreases. The magnetization of ferromagnetic or paramagnetic materials placed in the surroundings of the magnet distorts the magnetic field created in the magnet. Finally the temperature and pressure fluctuations inside the nitrogen and the helium vessels of the superconducting magnet cause also changes in the magnetic permeabilities of the materials surrounding and composing the Penning trap. These magnetic permeabilities fluctuations induce fluctuations in the magnetic field homogeneity and strength.

The magnetic field perturbations can be expressed as a series expansion. The lowest multipole term of interest in this series expansion, is a magnetic hexapole component  $B_2$ , which creates a frequency shift of  $\Delta\omega_c = B_2 \cdot \omega_c (\rho_z^2 - \rho_-^2)$  [20]. The determination of the  $B_2$  term of the magnet used for the tests presented in this thesis will be discussed in section 5.1.

### 2.2.2 Electric fields imperfections

Geometrical imperfections in the Penning trap construction cause deviations from the pure quadrupolar field defined in equation (2.2). These deviations from the ideal quadrupolar field are expressed in terms of a multipolar expansion of the trapping potential. In this case the frequency shift for the sum frequency  $\omega_c = \omega_+ + \omega_-$  depends on the amplitudes of the individual eigenmotions and is given by

$$\Delta\omega_c = \Omega_c \left[ \frac{3}{2} \frac{C_4}{d^2} (\rho_-^2 - \rho_+^2) + \frac{15}{4} \frac{C_6}{d^4} (\rho_z^2 (\rho_-^2 - \rho_+^2) - (\rho_-^4 - \rho_+^4)) \right]. \quad (2.18)$$

More details about this expression can be found in [20]. In this equation  $\Omega_c = \frac{\omega_-}{1 - (\omega_-/\omega_+)} \approx \omega_- \approx \frac{U}{2d^2B}$ , assuming  $\omega_+ \gg \omega_-$ . And  $C_4$  and  $C_6$  are the coefficients of the octupole and dodecapole components of the electric field, respectively. In order to minimize these imperfections, correction electrodes are usually added to the Penning traps.

### 2.2.3 Ion-ion interactions

Coulomb interaction among the ions stored inside a Penning trap affects the ion motion and thus the measured frequency. For that reason, high-precision

trap experiments use one single ion in the Penning trap for their measurements. When several ions from the same ion species are simultaneously stored, the driving frequency acts on the  $q/m$  center of the ion cloud and then no frequency shift is observed [31]. When ions of different species are stored at the same time they produce, in case of sufficient resolution, several resonances.

### 2.3 Ion excitation methods

In order to find a coherent motion of the trapped ions, and thus enable their resonant detection, an excitation of the ion motion with an external radiofrequency (rf) field has to be applied. The ion motion excitation makes the manipulation of individual eigenmotions possible, which can be used for ion detection and also for removing contaminations.

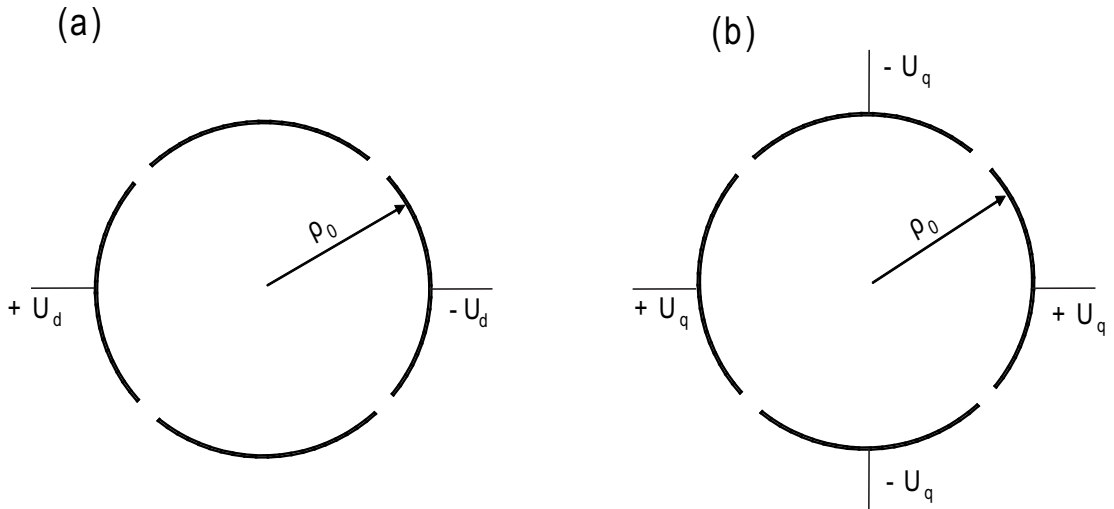


Figure 2.3: Configuration of the electrodes for creating a dipolar (a) or a quadrupolar (b) field using a four fold segmented ring electrode.

#### 2.3.1 Dipolar excitation

A dipolar excitation can be used for the manipulation and preparation of the trapped ions. This excitation signal at one of the ion's eigenfrequencies is applied to two opposite segments of a four fold segmented ring electrode of a Penning trap with a  $180^\circ$  phase-shift, see figure 2.3(a). Due to the

mass independence of the magnetron frequency,  $\omega_-$ , (see equation (2.14)) an excitation of all the trapped ion species can be done simultaneously. A dipolar excitation with the reduced cyclotron frequency,  $\omega_+$ , allows one to excite only a specific ion of interest and also can be used for the cleaning of the known contaminations that can shift the frequency of the studied ions [32]. The driving field in the  $x$ -direction is given by

$$\vec{E}_x = \frac{U_d}{a} \cdot \cos(\omega_d t + \phi_d) \cdot \vec{e}_x \quad (2.19)$$

where  $U_d$  is the rf voltage amplitude applied at a certain radius  $a$ ,  $\phi_d$  is a phase constant, and  $\omega_d$  is the applied excitation frequency.

### 2.3.2 Quadrupolar excitation

The coupling of two radial eigenmotions can be achieved using a quadrupolar excitation field around the sum frequency  $\omega_q = \omega_c = \omega_+ + \omega_-$ . In this case, the excitation is applied to four segments of the ring electrode, see figure 2.3(b), with the form:

$$\vec{E}_x = \frac{2U_q}{a^2} \cdot \cos(\omega_q t + \phi_q) \cdot y\vec{e}_x, \quad (2.20)$$

$$\vec{E}_y = \frac{2U_q}{a^2} \cdot \cos(\omega_q t + \phi_q) \cdot x\vec{e}_y, \quad (2.21)$$

thus enabling a conversion between the two radial motions as shown in figure 2.4. A complete conversion between the magnetron motion and the cyclotron motion is achieved after the conversion time:

$$T_{conv} = \pi \frac{m}{q} \frac{a^2}{2U_q} (\omega_+ - \omega_-) \approx \pi \frac{a^2}{2U_q} B. \quad (2.22)$$

considering  $\omega_+ \gg \omega_-$  and  $\omega_+ \approx \omega_c$ .

A quadrupolar excitation can be done using a Penning trap with a ring electrode split in eight segments instead of in four. In this case, the excitation of the ion motion is done in such a way that each of the polarities is applied to opposite segments of the ring. Figure 2.5 shows a schematic explanation of this excitation method. A  $+U_q$  potential is applied to segments 1 and 3 while the same potential with a  $180^\circ$  phase difference,  $-U_q$ , is applied to segments 2 and 4. The other four electrodes are used for detection.

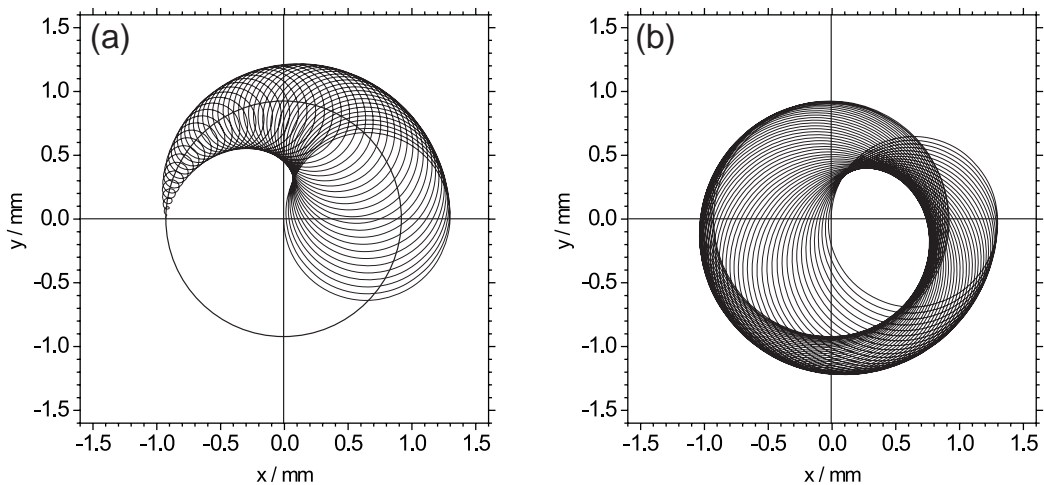


Figure 2.4: Conversion of a pure magnetron motion into a pure cyclotron motion at  $\omega_q = \omega_c$ . The motion starts with a pure magnetron motion (solid circle), then starts the cyclotron motion (increasing circles) (a) and the motion ends with a pure cyclotron motion (b). The first half of the conversion is shown in (a), the second one in (b). Figure from [18].

### 2.3.3 Broad-band excitation

Broad-band excitation of the ions is mainly used in chemistry, and it was invented in 1974 by M. B. Comisarow and A. G. Marshall [33, 34]. Broad-band ion cyclotron excitation, as shown in figure 2.6(a), is performed when the motion of ions with different  $q/m$  is excited simultaneously, instead of performing an excitation of the individual motion of a single ion species. Broad-band excitation is commonly performed by frequency sweep excitation [35, 36], which achieves the excitation of a relatively flat magnitude over a broad frequency range by use of a relatively low excitation amplitude [37].

### 2.3.4 Selected-ion-excitation mode

In the selected-ion-excitation mode, shown in figure 2.6(b), only the desired ion species are excited. One technique used to apply this method is the Stored Waveform Inverse Fourier Transformation (SWIFT) [38]. In this method, the excitation waveform is created reversing the usual process, *i.e.*, first the excitation profile is defined in the mass-to-charge domain, then converted into the frequency domain and finally the generation of the corresponding time domain excitation waveform is done via the application of the inverse Fourier transform [39].

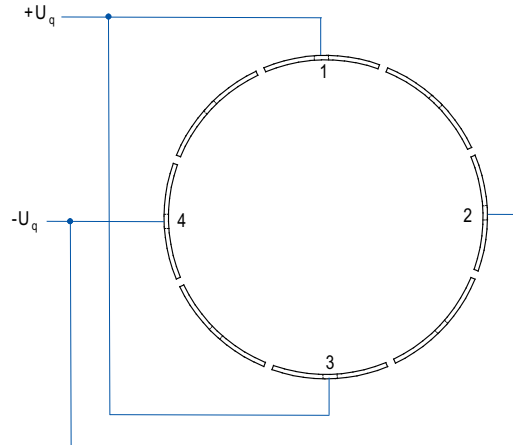


Figure 2.5: Quadrupolar excitation scheme with an eight segmented ring electrode in a Penning trap. The segments not numerated are used for detection.

Applying the SWIFT excitation method has the advantage that only the ion species of interest are excited, and thus is possible to detect these species while the rest of the trap content remains unseen. This method will be used in the KATRIN experiment. Results will be shown in section 6.6.

## 2.4 Ion cooling techniques

In order to diminish the amplitudes of the stored ions and thus to reduce the effects of trap imperfections on the determination of the individual eigenfrequencies, different ion cooling techniques can be used [18]. In the project presented within this thesis, no cooling of the ions was performed but a general review on some of those techniques will be presented here since one or the other might be applied in the future.

### 2.4.1 Buffer gas cooling

The buffer gas cooling technique is the most common one used for radioactive ions stored in a Penning trap [40]. The buffer gas injected in the trap provides the sufficient damping environment to decrease the energy of the ions and cool them down until a thermal equilibrium with the gas molecules is reached. The effect of the buffer gas on the ion motion can be expressed as a viscous

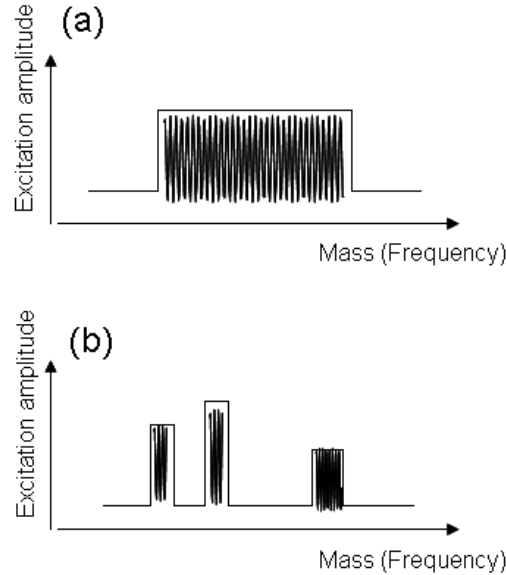


Figure 2.6: Two different ways of exciting several ion species are shown. The broad-band excitation (a) makes a sweep and excite all frequencies inside a given range. The selected-ion-excitation mode (b) applies excitation only in the chosen frequency spans, exciting only the desired ion species.

force

$$\vec{F} = -\delta m \vec{v}, \quad (2.23)$$

where  $m\vec{v}$  is the momentum of an ion with mass  $m$  and velocity  $\vec{v}$  and  $\delta$  is the damping parameter which can be written as a function of the ion mobility,  $K_{ion}$ , as

$$\delta = \frac{q}{m} \frac{1}{K_{ion}} \frac{p/p_N}{T/T_N}. \quad (2.24)$$

With  $p$  and  $T$  the pressure and the temperature of the gas in units of the normal temperature and pressure,  $T_N$  and  $p_N$ , respectively.

The damping of the ion cyclotron motion can be described as

$$\rho(t) = \rho_0 e^{-\delta t}. \quad (2.25)$$

### 2.4.2 Resistive cooling

In this case the ion amplitude is reduced by the use of an external circuit that is continuously kept in resonance with the ion motion eigenfrequency. The external resistance dissipates the energy of the ions detected via the induced image current method and finally a thermal equilibrium with the

environment is reached. Resistive cooling is especially efficient for ions with a large charge-to-mass ratio [41].

### 2.4.3 Evaporative cooling

This technique was first developed in order to achieve Bose-Einstein condensation in gaseous hydrogen [42]. Within this method the energetic ions are removed from the trap by lowering the trapping potential, collisions then readjust the remaining ions into a lower temperature thermal distribution. The ions remaining in the trap have then a lower energy once the trapping voltage is back to normal value. This procedure can be continued until just a few ions are remaining in the trap. This method is widely used for magnetically trapped atoms [43]. So far only one high-precision Penning trap mass spectrometer employed evaporative cooling, namely SMILETRAP [44] to cool highly charged ions [45].



# Chapter 3

## Ion detection techniques

Two different ion detection techniques shall be described for stored ions in a Penning trap. The destructive **T**ime-of-**F**light-**I**on **C**yclotron **R**esonance (TOF-ICR) and the non-destructive **F**ourier **T**ransform-**I**on **C**yclotron **R**esonance (FT-ICR) detection. The term non-destructive and destructive indicates whether or not the ions are destroyed after its detection.

### 3.1 Time-of-flight-ion cyclotron resonance detection

The Time-of-Flight-Ion Cyclotron Resonance (TOF-ICR) method is a destructive method since the ion is lost after hitting the particle detector. In a first step ions are prepared in a coherent motion on a specific radius by applying a dipolar excitation at the magnetron frequency with the radial energy  $E_r(t) \approx \omega_-^2 \rho_-^2(t)$ . After this, the magnetron motion is converted into a cyclotron motion by applying a quadrupolar excitation with a frequency near or at  $\omega_{rf} = \omega_c$ , with the radial energy  $E_r(t) \approx \omega_+^2 \rho_+^2(t)$  when no axial motion is assumed. After a certain excitation time, defined by one full conversion from pure magnetron to pure cyclotron motion at resonance and with suitable amplitude (see equation (2.22)), the trapping voltage is switched off and the ions are ejected from the trap following the magnetic field gradient towards a detector, as shown in figure 3.1(a). The force that the ion feels due to the magnetic field gradient is proportional to the magnetic moment  $\vec{\mu}$  and hence to the radial energy:

$$\vec{F} = -\vec{\mu}(\vec{\nabla}B) = -\frac{E_r}{B} \frac{\partial B}{\partial z} \vec{e}_z. \quad (3.1)$$

The ions with initially higher radial energy lead to a minimum flight time. The time of flight from the center of the trap to the detector can be calculated by [46]:

$$T_{tot}(\omega_q) = \int_0^z \sqrt{\frac{m}{2(E_0 - qU(z) - \mu(\omega_q)B(z))}} dz, \quad (3.2)$$

where  $E_0$  is the initial axial energy of the ion and  $U(z)$  and  $B(z)$  the electric and magnetic potential differences, respectively.

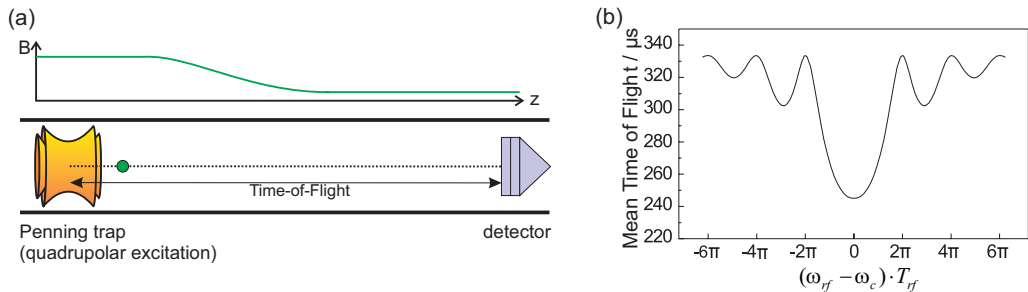


Figure 3.1: (a) Scheme of the time-of-flight-ion cyclotron resonance detection technique [47]. (b) Theoretical time-of-flight resonance curve as a function of the frequency showing a minimum for  $\omega_{rf} = \omega_c$ . Figure adapted from [18].

When the excitation frequency is matching exactly the free cyclotron frequency and the excitation time is the same as the conversion time, a minimum in the time of flight is observed, as shown in figure 3.1(b). When the excitation frequency is not matching the resonant frequency the full conversion is not achieved and thus the time of flight is longer. A scan around the center  $\omega_c$  produces a time-of-flight resonance curve. The theoretical line shape expected for such a resonance is determined by the Fourier transformation of the rectangular shaped time excitation pulse which presents side bands due to the finite excitation time.

In our setup this technique is used for counting the ion number, as it will be shown in chapter 5.

## 3.2 Induced image charge detection

The induced image charge detection method allows for keeping the ions stored in the trap after being detected, thus several measurements can be done using the same sample of particles [48]. This method is based on the detection of the ion image current induced on the ring electrode. A charged particle  $q$ , with a velocity  $\vec{v}$ , absorbs the power from an electric field  $\vec{E}$  which is

generated by a voltage  $U$  applied to a pair of electrodes perpendicular to the ion motion. The current supplied is given by

$$i = \frac{P}{U} = \frac{q\vec{v} \cdot \vec{E}}{U}. \quad (3.3)$$

In case an external resistor is connected to the plates, the energy is dissipated from the ion. Thus, the image current induced by an ion in the electrodes of the trap is determined by its velocity and the electric field  $\vec{E}/U$ . If the detection electrodes are considered to be two parallel plates, the image current is

$$i = q \frac{2\pi\nu_{ion}r_{ion}(t)}{D}, \quad (3.4)$$

where  $\nu_{ion}$  is the frequency of the detected ion motion,  $r_{ion}(t)$  is the projection of the radius perpendicular to the electrodes and  $D$  is approximately the distance between the two electrodes. Figure 3.2 shows schematically the general detection and excitation scheme for a four segmented ring electrode Penning trap. A two stage amplification is done before a fast Fourier transformation (FFT) is used for converting the time domain signal into the frequency domain spectrum.

This induced image charge detection method is commonly called the Fourier Transform-Ion Cyclotron Resonance (FT-ICR) detection method.

### 3.2.1 Narrow-band FT-ICR detection

When using a narrow-band detection setup the image current generated by the trapped particles is not directly investigated, but a tuned circuit is used for converting the current into a voltage. The attached tuned circuit acts as a narrow-band pass filter around the expected ion frequency. The ring segments used to pick up the ion signal are connected in parallel with an inductance. This, together with the intrinsic capacitance of the elements forming the detection system, creates a parallel LC circuit that converts the small current signal into a voltage drop. The narrow band width implies that the impedance  $Z(\omega)$  of the circuit depends on the frequency and has a maximum around its center frequency  $\omega_{LC}$ . The quality factor of the circuit depends on the center frequency and on  $\Delta\omega$ . The quality factor  $Q$  is defined as

$$Q = \frac{\omega_{LC}}{\Delta\omega}. \quad (3.5)$$

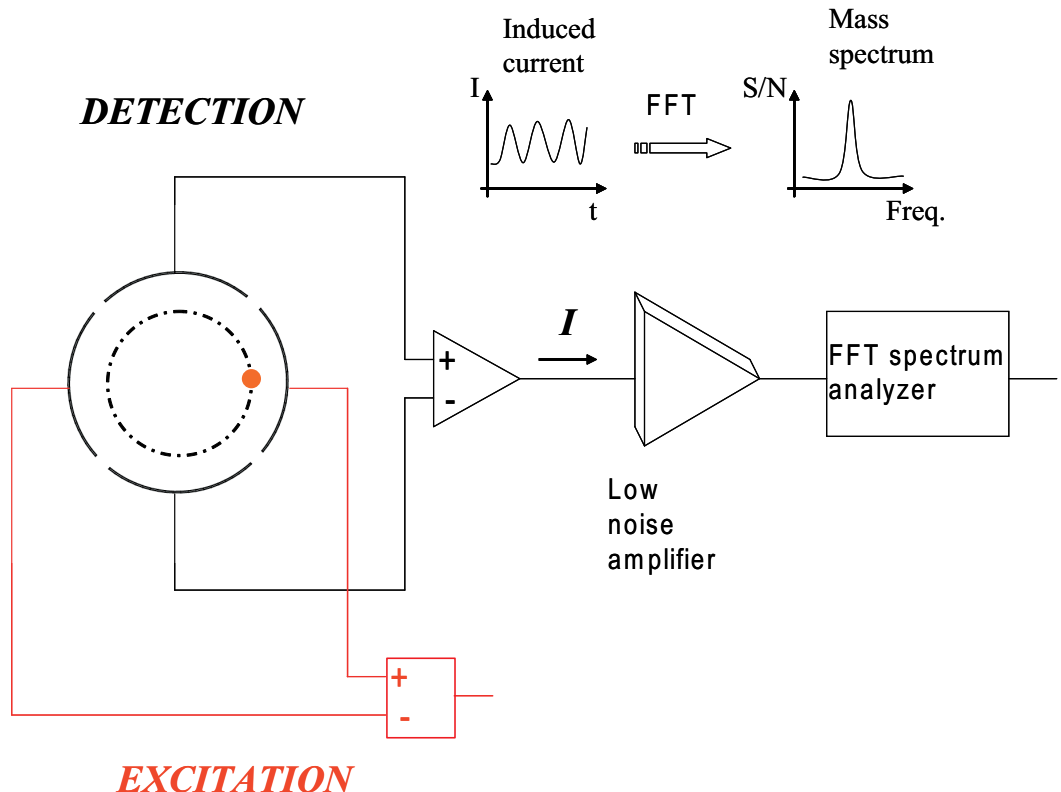


Figure 3.2: Typical configuration for FT-ICR excitation and detection. Two opposing ring electrode segments of the trap are used for the ion excitation while the other two are used for the induced image current detection. The frequency spectrum is obtained by a Fourier transformation of the amplified image current. For more details see text.

The impedance  $Z(\omega)$  of the tuned circuit has a value of <sup>1</sup>

$$Z(\omega) = \frac{1}{\frac{1}{R} + i(\omega C - \frac{1}{\omega L})}. \quad (3.6)$$

And the absolute value of the impedance shows a maximum around the frequency

$$\omega_{LC} = \frac{1}{\sqrt{LC}}. \quad (3.7)$$

---

<sup>1</sup>The symbol  $\hat{i}$  is used for the imaginary number ( $\hat{i} = \sqrt{-1}$ ).

### 3.2.2 Broad-band FT-ICR detection

In broad-band detection the image current induced by the trapped ions into the electrodes is directly amplified by a low noise preamplifier, without any circuit in between in contradiction to the narrow-band detection.

An ion cloud stored in a trap with a large number of ions ( $10^3 - 10^6$  charges) will induce a current in the detection segments of the ring electrode. This signal in the time domain is amplified by a low-noise amplifier and converted to the frequency domain by a Fourier transformation, see figure 3.2. Using this method a broad range of frequencies can be detected. This method is not used for high-precision mass measurements due to the large number of ions needed to have a measurable signal which is limited to  $\approx 200$  ions in a room temperature setup [37].

### 3.2.3 Dipolar detection

The dipolar detection method is commonly used in Penning traps with a ring electrode split in four segments. In such a case two opposing segments of the ring are used for excitation and the other two opposing ones are used for detection. The detected signals are then individually amplified and after that subtracted to each other, as it is shown in the sketch in figure 3.3, indicated with the symbol  $\Delta$ .

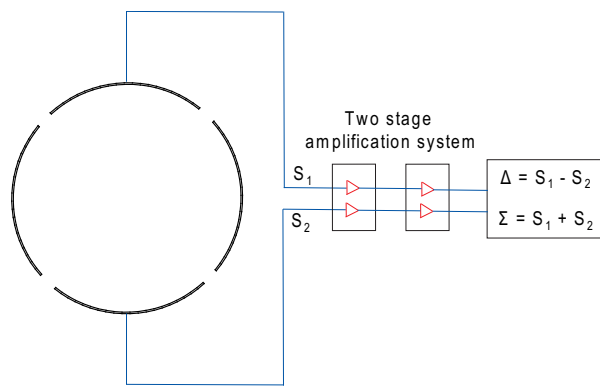


Figure 3.3: Dipolar, shown with  $\Delta$ , and quadrupolar,  $\Sigma$ , detection method when using a Penning trap with a four-fold segmented ring electrode.

Within this method typically the excited eigenmotion is also the detected one, and the induced image current is proportional to the magnetron or the cyclotron radius. When doing mass measurements using dipolar detection the eigenfrequency  $\nu_+$  is detected.

### 3.2.4 Quadrupolar detection

When quadrupolar detection is performed using a ring electrode split in four segments, the induced currents from each of the opposite trap segments are added to each other, as shown in figure 3.3 with the symbol  $\Sigma$ . When a quadrupolar excitation is used and a quadrupolar detection is applied it is possible to detect the sum frequency ( $\nu_+ + \nu_-$ ) of interest for mass measurements. In this case the detected signal is proportional to the product of the magnetron and the cyclotron radius.

A proper quadrupolar detection is done using a ring electrode split in eight segments, instead of four. When having an eight segmented ring electrode the detection is done in the following way (see figure 3.4 for clarification): the signals induced in two alternate segments of the ring electrode (e.g.  $S_1$  and  $S_2$  from 3.4) are added to each other, and the induced signal into other two opposite segments ( $S_3$  and  $S_4$ ) are also added to each other. The resulting currents,  $S'_1$  and  $S'_2$ , are subtracted and afterwards fast Fourier transformed and monitored. Figure 3.4 shows us the schematic explanation of this kind of detection.

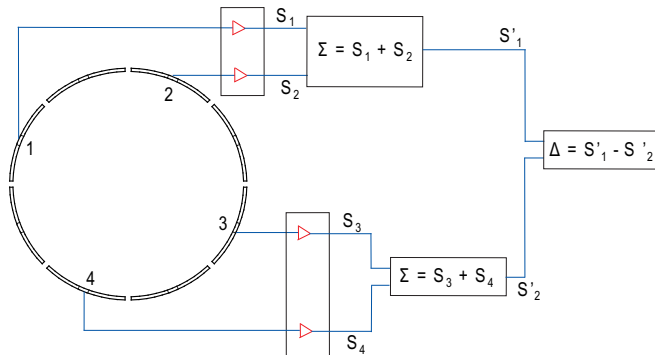


Figure 3.4: Quadrupolar detection method scheme using an eight segmented ring electrode. See text for details.

### 3.2.5 Selected-ion-detection mode

The selected-ion-excitation mode was explained in section 2.3.4. Analogously this same technique can be used for detection. Within this method several small frequency ranges are checked, and not the full spectra. This detection method will be the one used in the KATRIN experiment with a four fold segmented Penning trap, some results will be shown in section 6.6. This technique can be used by applying either dipolar or quadrupolar detection as it has more to do with the signal treatment than with the detection itself.

Within this method, after the detection and amplification of the signal, the desired fragment of the time domain signal is fast Fourier transformed and monitored. In our experimental setup this is done using a downconverter, which allows us to isolate up to eight different segments of the transient and thus look for the eight desired ion species. A more detailed explanation about how this detection method is used in our experiment will be given in section 5.6.2.



# Part II

## Experiment



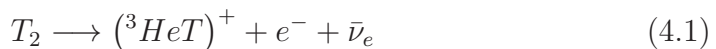
# Chapter 4

## The Karlsruhe Tritium Neutrino experiment

Within this chapter a general overview on the **K**Arlsruhe **TRI**tium **N**eutrino (KATRIN) experiment will be given, explaining the basis of the KATRIN setup. A focus will be set on the beamline section where two Penning trap systems will be installed.

### 4.1 The KATRIN experiment

The **K**Arlsruhe **TRI**tium **N**eutrino (KATRIN) experiment, which is an experiment based on the tritium  $\beta$ -decay



has as a main purpose the improvement of the upper limit for the electron antineutrino rest mass. KATRIN aims for the measurement of the electron antineutrino rest mass with a sensitivity of  $0.2\text{ eV}/c^2$  (95% c.l.) [10], one order of magnitude better than the present best value from the Mainz [16] and the Troisk [17] experiments .

An overview of the KATRIN experiment is shown in figure 4.1. A 70 m long linear configuration with about 40 superconducting solenoids which adiabatically guide  $\beta$ -decay electrons from the source to the detector.

The experiment can be divided in five main parts [11]:

1. The *Windowless Gaseous Tritium Source* (WGTS) consists of a 10 m long cylindrical tube of 90 mm diameter. The gaseous tritium is inserted in the middle and pumped out at both ends.

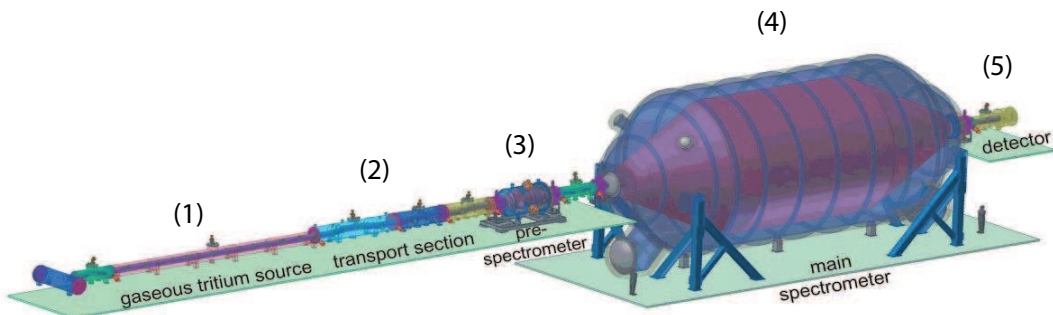


Figure 4.1: Overview of the KATRIN experiment [11]. Each of the five sections of the experiment is labeled, see text for more details.

2. Beta-decay electrons and remaining tritium molecules enter the *transport section*, which has the purpose of eliminating the tritium while guiding the electrons towards the two spectrometers. This is achieved by a combination of turbo molecular and cryogenic pumps and superconducting magnets. A more detailed description of this section will be given in chapter 4.2 since the MPIK traps will be installed therein.
3. The *pre-spectrometer* is a smaller version of the main spectrometer. A static electric field provides a retardation energy of about 100 eV below the endpoint  $E_0$  and removes all but a fraction of  $10^{-7}$  electrons at the highest energies.
4. The *main spectrometer* is 23 m in length and 10 m in diameter. Both main and pre-spectrometer (also called tandem spectrometer) will be operated as MAC-E-filters (Magnetic Adiabatic Collimation combined with an Electrostatic Filter) [49, 50], *i.e.* the  $\beta$ -electrons are guided magnetically on a cyclotron motion around the magnetic field lines into the spectrometer, thus resulting in an accepted solid angle of up to  $2\pi$ . Therefore the spectrometer acts as an integrating high-energy pass filter. Magnetic fields are provided by superconducting magnets on both sides of the spectrometers. Electrons are counted in an integral fashion above the retarding potential, which is varied in small steps just below  $E_0$ . The spectrometers will operate at a temperature down to -20°C to reduce outgassing. To minimize background, an ultra-high vacuum of better than  $10^{-11}$  mbar is needed.
5. The electrons leaving the main spectrometer are guided to a *detector*, which is needed as a counting device.

## 4.2 Transport section and differential pumping section

The background generated by tritium decay within the spectrometers must be less than  $10^{-3}$  counts/s, which limits the amount of tritium allowed in the main spectrometer equivalent to a partial pressure of tritium of about  $10^{-20}$  mbar. This leads to a maximal allowed tritium flow rate into the pre-spectrometer of the order of  $10^{-14}$  mbar l/s. This design criterion requires that the tritium flow is suppressed by about a factor of  $10^{11}$  between the outlet of the WGTS tube and the entrance of the pre-spectrometer. This very large suppression factor will be achieved by an effective tritium pumping system, based on a combination of differential (DPS) and cryogenic (CPS) pumping sections [11]. Both segments of this transport section are shown in figure 4.2. In the following only the differential pumping section inside the transport system will be explained, because of its interest for the measurements presented in this thesis.

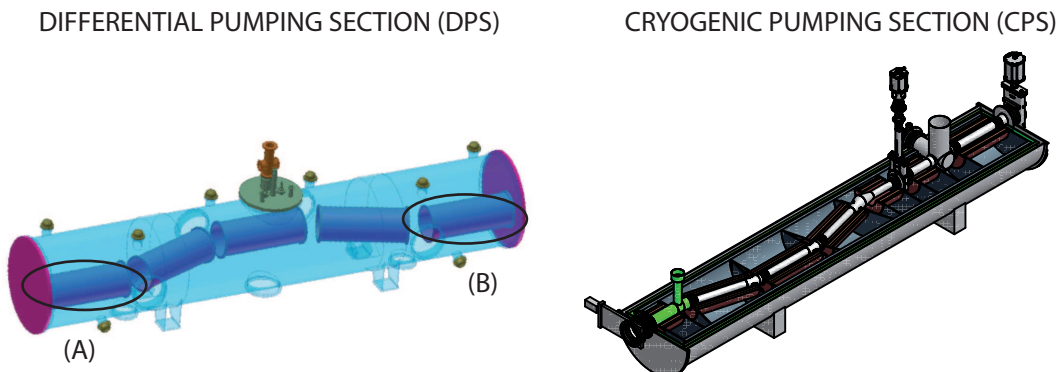


Figure 4.2: Transport system, where the two parts — differential pumping section (DPS, left) and cryopumping section (CPS, right) — can be seen. The position of the two Penning traps is marked at the DPS figure with (A) and (B). For more details see [11].

The differential pumping section has two main tasks: the guiding of the  $\beta$ -electrons towards the tandem spectrometer and the removal of unwanted particles which are considered as contaminations that can disturb the  $\beta$ -decay endpoint measurement. The DPS is a beamline consisting of five segments of 1 m, each tilted by  $20^\circ$  with respect to each other. It is operated at liquid nitrogen temperature (77 K). It has four pumping ports and five solenoids that produce a magnetic field of  $B \approx 5.6$  T.

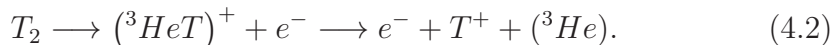
Besides of the differential pumping itself, the DPS will contain three electrical dipole elements which will be used for ion removal. This will be done by applying an orthogonal electric gradient which pushes the charged particles via an  $E \times B$ -drift (where  $E$  is the applied electric field and  $B$  is the magnetic field induced by the solenoids) towards the walls of the vacuum chamber. Such a process will neutralize the charged particles making them possible their pumping [51].

Inside the beam tube of this section two Penning traps will be installed. Figure 4.2(left) shows the position of each trap: the first Penning trap will be placed at the entrance of the DPS (A) and the second one will be placed at the exit (B), right before the CPS. These two Penning trap systems build the only on-line monitoring devices between the tritium source and the detector, and will provide not only an estimate of the pumping rate of the DPS by comparing the ion concentration in the first and the second trap but also important information on the beamline content. The latter will allow for the correction of possible shifts that contaminations can produce at the  $\beta$ -decay endpoint. This monitoring will be done using the FT-ICR method already described in chapter 3.2. The off-line characterization of this Penning trap system is the main topic of this thesis. In chapter 5 the setup used to this purpose will be explained in detail. Finally chapter 6 will show the obtained results of this off-line characterization.

### 4.3 Expected ion contaminations in the KA-TRIN beamline

Molecules or ions containing tritium could occur in the *windowless gaseous tritium source* (WGTS), giving rise to contributions to the overall  $\beta$  spectrum with different endpoint energies  $E_0$ . Table 4.3 shows the endpoint energies for various tritium decays relative to the atomic mass difference between  ${}^3\text{He}$  and  ${}^3\text{H}$ ,  $\Delta M({}^3\text{He}, {}^3\text{H}) = 18.5898(12)$  keV [13].

The tritium  $\beta$ -decay itself as well as the  $\beta$ -electrons interacting with the source molecules lead to the creation of several types of tritium ions and atomic tritium:  $\text{T}$ ,  $\text{T}^+$ ,  $\text{T}_3^+$ ,  $\text{T}_5^+$  or  $\text{T}^-$  [52]. Primary ions from the  $\beta$ -decay lead to the formation of  $\text{T}^+$



The  $({}^3\text{HeT})^+$  ions are then transformed to  $\text{T}_3$  by the following reaction

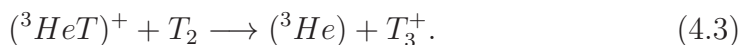
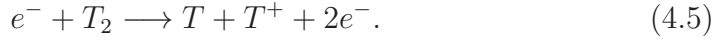


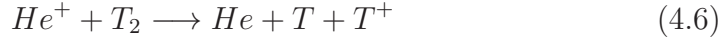
Table 4.1: Endpoint energies  $\tilde{Q}$  with respect to the mass difference  $\Delta M(^3\text{He}, ^3\text{H})$  for different atomic and molecular decays.

Decay process	$\tilde{Q} = E_0 - \Delta M(^3\text{He}, ^3\text{H})$
$^3\text{H} \rightarrow ^3\text{He}^+ + e^- + \bar{\nu}_e$	-24.6 eV
$^3\text{H}^- \rightarrow ^3\text{He} + e^- + \bar{\nu}_e$	-0.75 eV
$^3\text{H}^+ + e^- \rightarrow ^3\text{He}^{++} + 2e^- + \bar{\nu}_e$	-65.4 eV
$^3\text{H}_2 \rightarrow ^3\text{He}^3\text{H} + e^- + \bar{\nu}_e$	-16.5 eV
$^3\text{H}_2^+ + e^- \rightarrow (^3\text{He} ^3\text{H})^{++} + 2e^- + \bar{\nu}_e$	-48.9 eV
$^3\text{H}_3^+ + ^3\text{H} + e^- \rightarrow (^3\text{He} ^3\text{H}_2)^{++} + 2e^- + \bar{\nu}_e$	-35.1 eV

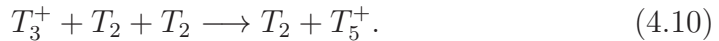
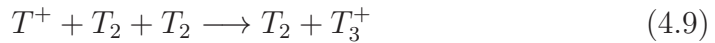
Secondary ionization forms mainly  $T_2^+$  and in a lower rate  $T^+$  through the following reactions



Due to the high ion density inside the WGTS (planned column density:  $5 \cdot 10^{17} \text{ T}_2/\text{cm}^2$ ), the next chemical reactions could also happen



Three body collisions can create  $T_5^+$  and  $T_3^+$  by the reactions



The formation of  $T^-$  from the ground state of  $T_2$  can occur by dissociative attachment



Possible contaminations that can be created in the KATRIN beamline and their cyclotron frequencies at a certain magnetic field are shown in table 4.3.

Table 4.2: Possible contaminations in the KATRIN beamline and their cyclotron frequencies calculated for a magnetic field strength of 5.6 T.

Possible contamination	Cyclotron frequency at $B=5.6\text{ T}$ (MHz)
$\text{H}_2^+$	38.39
${}^3\text{He}^+$ , ${}^3\text{T}^+$	25.59
$\text{DT}_2^+$	9.60
$\text{T}_3^+$	8.53
$\text{T}_5^+$	5.12

# Chapter 5

## FT-ICR Penning trap setup in Heidelberg

The characterization of the Penning trap system that will be implemented in the KATRIN beamline has been done at a setup built at the Max-Planck-Institute for Nuclear Physics (MPIK) in Heidelberg. The experimental setup, shown schematically in figure 5.1, consists of an ion source, a set of quadrupole lenses for focusing the ions, a cylindrical Penning trap with its electronics and a Faraday cup or a microchannel-plate detector used as destructive ion counting devices. The setup is completed with a 4.7 T superconducting magnet, which provides the strong homogeneous magnetic field needed for the trapping of the ions under investigation. Each of these components of the setup will be explained within this chapter.

### 5.1 Superconducting magnet

The superconducting magnet used for the experiments presented within this thesis has a length of 102 cm and a field strength of 4.7 T in its homogeneous region. The magnet was manufactured by *Bruker*<sup>1</sup>. In order to store the ions inside the Penning trap the magnetic field has a crucial role, therefore the first test performed in the laboratory was the measurement of the magnetic field along the magnet bore using both a Nuclear Magnetic Resonance (NMR) and a Hall probe.

The Nuclear Magnetic Resonance [53] (NMR) probe (PT2025 NMR Teslameter by Metrolab) was used for measurements in the homogeneous region of the magnet, a region with a very low field gradient. To complete the magnetic field map, a Hall probe (7010 Gauss/Teslameter by Sypris) was used to

---

<sup>1</sup>Bruker BioSpin GmbH. Silberstreifen 4. 76287 Rheinstetten. Germany.

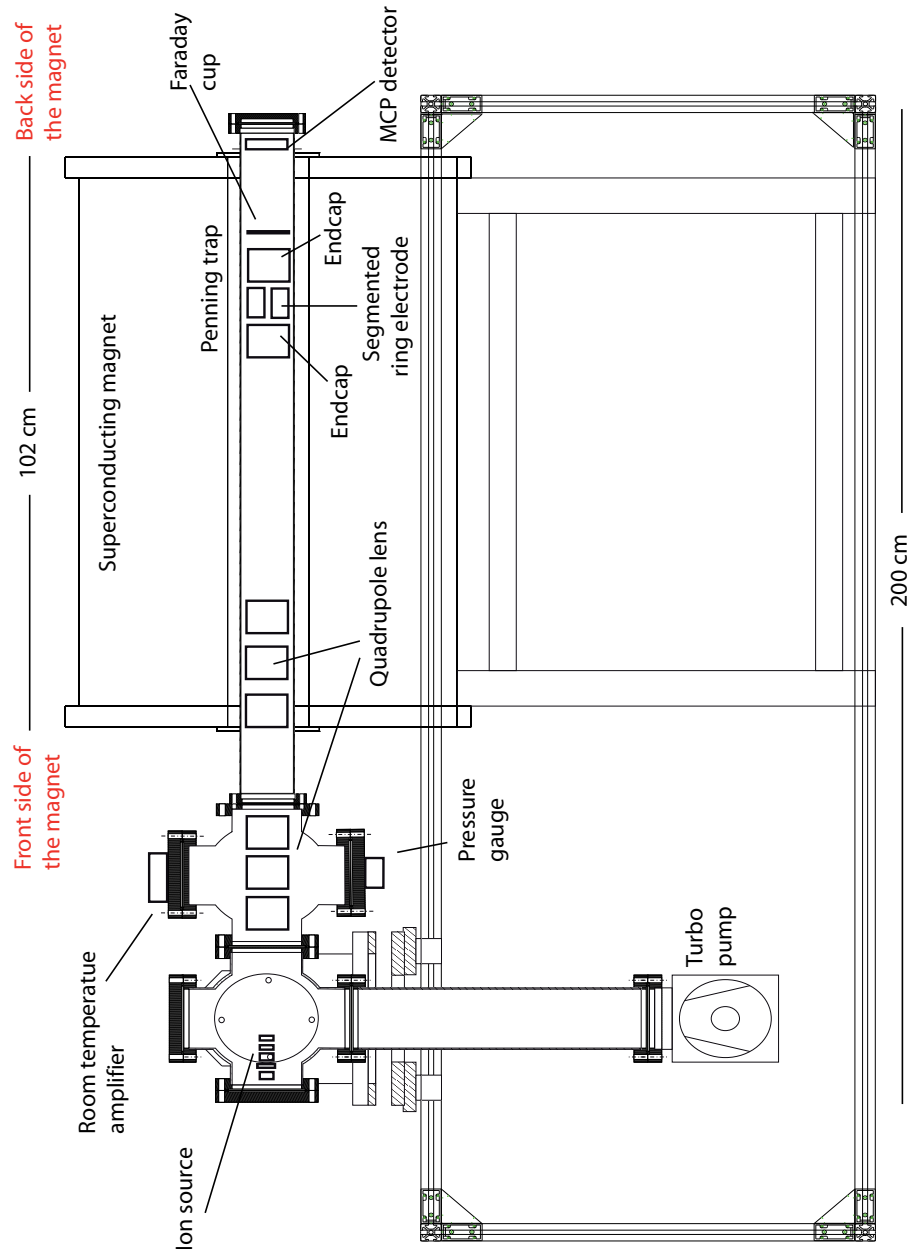


Figure 5.1: Side view of the experimental setup. Ions created in the ion source are guided by a set of quadrupole lenses towards the Penning trap which is placed at the homogeneous region of a 4.7 T superconducting magnet. After the ion excitation and FT-ICR detection the ions are released and can be detected with a Faraday cup or an MCP detector for further analysis.

measure the magnetic field in the inhomogeneous field region of the magnet. Hall probes are based on the Hall effect [54].

The measurement results of the magnetic field on the  $z$ -axis is shown in figure 5.2. The dashed red rectangle in the plot shows the magnet position, the magnetic field was measured not only in the magnet bore but also in a region  $\approx 125$  cm away from the magnet's homogeneous region.

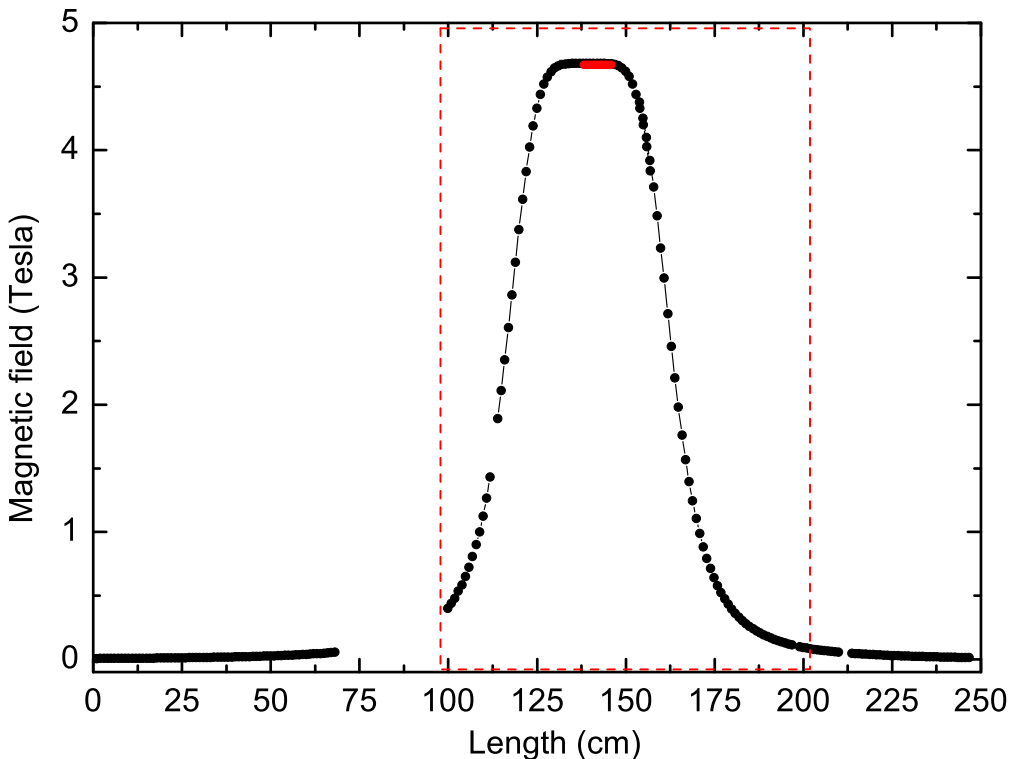


Figure 5.2: Magnetic field along the  $z$ -axis. The magnet position is shown by a red dashed rectangle.

The points in the homogeneous region (covered by the red line in figure 5.2) were measured with the NMR probe. Figure 5.3 shows the measurement done with the NMR probe, in this case the measurement was done starting from the back side of the magnet. The homogeneous region can be considered as a cylinder of 1 cm in diameter and 10 cm in length at about 38 cm distance from the back side of the magnet. The average value of the field in these ten centimeters is  $B = 4.699\ 3(2)$  T. The homogeneity of the magnetic field in a  $\approx 1\ \text{cm}^3$  volume was calculated from these measurements and results in,  $\delta B/B = 5.42 \cdot 10^{-6}$ . The correction coefficient  $B_2$  for the magnetic field

inhomogeneities was also calculated in this region, yielding to a value of  $B_2 = -1.82(11) \cdot 10^{-6} \text{ mT/mm}^2$ .

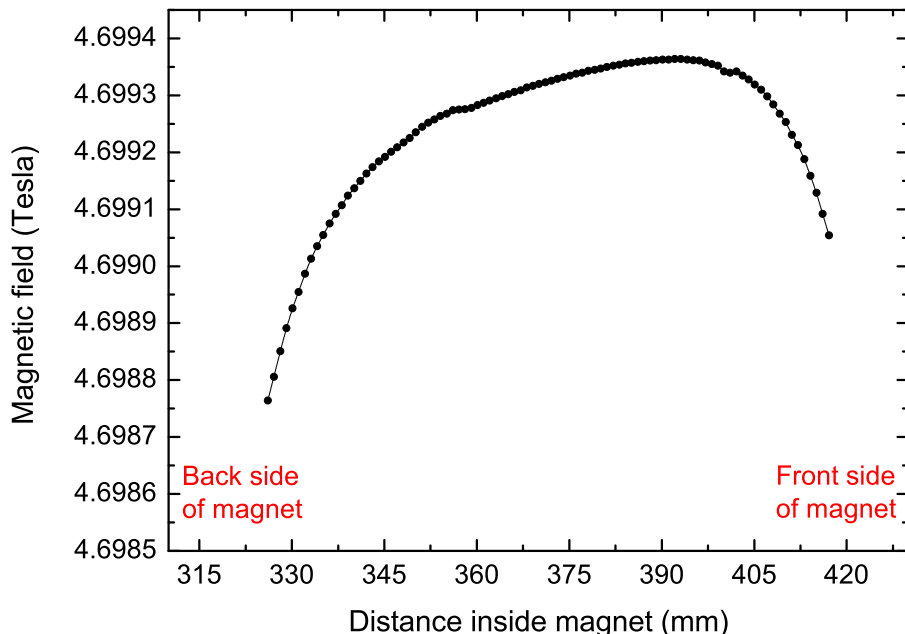


Figure 5.3: Magnetic field along the homogeneous region measured with the NMR probe.

In order to have an idea about the stability of our magnetic field some long time measurements were performed as well. The current in the superconducting coils of the magnet decreases with time due to the so-called *flux creep* phenomenon [30, 55]. This decay happens in an exponential way on a time scale of years, but can be approximated linearly within a few days or shorter. In the case of our magnet the decay time was calculated from a measurement done during 96 hours, from there we can make a rough estimation of the magnetic field decay, which yields to a value of  $(\delta B/B) \cdot (1/\delta t) = 2.50 \cdot 10^{-11} \text{ min}^{-1}$ .

The obtained results for the homogeneity and stability of the used magnet does not suppose a limitation for the studies performed within this thesis.

## 5.2 Ion production

Three different kind of ion sources for the ion production were used for the results presented within this thesis. A surface ion source was used in order to provide a clean ion beam, the ion species extracted from this ion source

depend on the pellet installed on it. In order to perform a broad-band measurement and to ionize a gas injected into the vacuum chamber (or the rest gas inside of it), a commercial electron impact ion source was used. The third used ion source was a UV cathode ion source which will be used for testing the KATRIN beamline [56]. This source was characterized in the setup built at the MPIK.

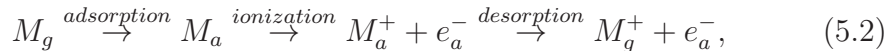
All three ion sources will be described in the following.

### 5.2.1 Surface ion source

The process of surface ionization is done by generating low energy and low temperature ions with a narrow distribution of energy. The ionization efficiency,  $\alpha$ , is written by the Saha-Langmuir equation as [57]

$$\alpha = \frac{n_+}{n_0} = \frac{g_+}{g_0} \cdot e^{\frac{-(\phi_i - W_s)}{kT_s}} \quad (5.1)$$

where  $n_{0,+}$  are the number densities of the neutral and its ion respectively, and  $g_{0,+}$  are the statistical weights of the neutral and its ion, respectively.  $\phi_i$  is the ionization potential of the neutral.  $W_s$  is the work function and  $T_s$  is the temperature of the ionization surface. And  $e$  and  $k$  are the electron charge and the Boltzmann's constant, respectively. The ionization process is schematically represented by



where the subscripts  $g$  and  $a$  indicate the gaseous and the adsorbed species on the hot surface, respectively. A general description of the process would be the following: first the metal vapor is adsorbed when contacting the hot surface; then due to the high working function an electron is dragged into the surface ionizing the metal atom; and finally by applying a positive bias voltage the ion is released from the surface.

Our surface ion source consists of a set of electrodes used for focusing the ions produced by the pellet. The substrate attached on the pellet surface is heated by applying a DC current on it. The applied heat ionizes the substrate. Once the ions are created they are extracted from the ion region and focused by a set of lenses. After that stage, four deflectors are used for centering the beam at the desired position. In between the electrodes 4 mm sapphire balls are used to isolate them from each other. The custom ion source used is shown in figure 5.4. The ion source is directly attached to a custom flange where the SHV connectors are included. A floating voltage must be applied to the pellet in order to extract the ions.

For almost all results presented here, a pellet with a mixture of  ${}^6\text{Li}^+$  and  ${}^7\text{Li}^+$  in its natural abundance, 7.59 % and 92.41 %, respectively, was used.



Figure 5.4: Surface ion source used in the Penning trap setup at the MPIK. It consists of a pellet and several sets of electrodes used for focusing and deflecting the ions.

### 5.2.2 Electron impact ion source

The Axial Molecular Beam Ionizer, see figure 5.5, is a commercial system from ABB Extrel [58], designed specifically for high-efficiency electron impact ionization of molecular beams. This ionizer consists of an ion region (a volume surrounded by a metallic mesh) where free electrons are created by a hot tungsten filament, an extraction plate where a negative voltage is applied to extract positive ions, and an einzel lens where the first and the third electrode are connected to a negative voltage and the second one to ground. The einzel lens is used to focus the beam. In order to avoid that the filament breaks due to the Lorentz force (when the source is placed in the magnetic field) an AC current is needed.

This molecular beam ionizer is designed for Electron Impact Ionization (EII). EII occurs when an energetic electron (10-100 eV) removes an electron from a molecular or atomic orbital as follows [58]:



This collision can exceed the molecular binding energy, producing molecular ionization and dissociation. When the excess energy on the ion ex-



Figure 5.5: Electron impact ion source from ABB Extrel [58] for the ionization of atomic or molecular beams and gaseous species.

ceeds the binding energies that hold the molecular ion  $AB^+$ , fragmentation ( $AB^+ \rightarrow A + B^+$  or  $AB^+ \rightarrow A^+ + B$ ) occurs. Applying an electrostatic field, the electrons are extracted from the filament and accelerated into the ionization volume. These electrons interact with analyte molecules in the ion volume and create ions. The ion energy is determined by a potential difference between the ion volume and the potential applied to the filament.

### 5.2.3 Photocathode ion source

A photocathode ion source was designed and built at the Karlsruhe Institute of Technology (KIT) in order to test the KATRIN beamline before attaching it to the tritium source [56].

The ion source was designed to simulate the ion flux emitted from the Windowless Gaseous Tritium Source (WGTS) of the KATRIN experiment. The next requirements must be then fulfilled, it must be able to ionize gas at pressures in the range of  $10^{-5}$  to  $10^{-4}$  mbar, corresponding to the pressure at the entrance of the KATRIN beamline. It should be able to operate in an axial magnetic field of around 5 T, as it will be in the KATRIN beamline. No rf fields can be used, in order to avoid interference with the electronics of the Penning trap system. A production of several tenths of nanoamperes in continuous mode is needed in order to imitate the WGTS.

The design of the source can be seen in figure 5.6. The electrons that are emitted from the photocathode are accelerated due to the potential difference between the cathode and the accelerator plate. The next electrode has a cylindrical shape and it works as a volume for ionization. The last electrode

is a grid used as an extractor for the created ions. This ion source, same as the previous one, ionizes the rest gas or the injected gas inside the vacuum chamber.

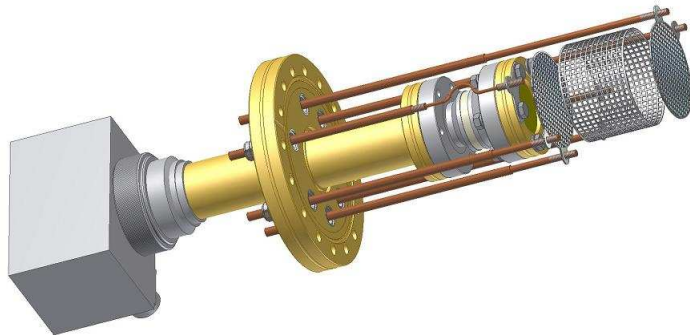


Figure 5.6: Design of the ion source based on photoelectric emission that will be used for testing the beamline in the KATRIN experiment. Courtesy of the Karlsruhe Institute of Technology.

The results of the off-line characterization of this ion source can be found in [56]. Part of the results of the characterization of this ion source together with the KATRIN Penning trap system will be presented in this thesis (see chapter 6).

### 5.3 Ion optics

An important element in the described setup are the einzel lenses. Since the ion source is placed about 130 cm away from the strong side of the magnet (labeled as back side in figure 5.1), the ions need to be guided into the trap region in order to avoid the mirroring caused by the magnetic field gradient. In the setup described here two einzel lenses are used, one of them is at the exit of the ions from the ion source and the second one is at the entrance of the magnet where the magnetic field gradient is larger. An actual photo of one of the lenses can be seen in figure 5.7.

The quadrupole lens is a commercial system designed and manufactured by RoentDek Handels GmbH<sup>2</sup>. The non-magnetic quadrupole lens system is delivered as a full piece with the desired length and diameter, which makes its installation easier.

---

<sup>2</sup> RoentDek Handels GmbH. c/o Institut für Kernphysik. Max-von-Laue-Str. 1.D-60438 Frankfurt am Main. Germany



Figure 5.7: Commercial quadrupole lens from Roentdek Handels GmbH used in the experiment for guiding the ions from the source to the trapping region.

The einzel lens consists of a set of three electrodes each of them split in four segments. In our configuration the four segments in the first and third set of electrodes are connected and thus a single voltage is applied. However, in the middle, since two of the electrodes are connected with its respective neighbors, two different voltages can be applied to deflect the beam.

## 5.4 The Penning trap

A three-pole cylindrical Penning trap, see figure 5.8, originally designed by *Stahl-Electronics*<sup>3</sup> and modified and adapted within this work, will be used as a monitoring device for examining the ion density at a certain beam position in the KATRIN experiment. The trap dimensions feature a so-called Gabrielse-type design [59], which provides a well-known electrostatical behavior [60].

The trap, shown in figure 5.8, consists of two endcaps and a central ring electrode which is split into four segments for allowing the ion excitation by applying a dipolar rf field as well as for image charge detection. The trap has an outer diameter of 83 mm, an inner diameter of 71 mm, and a length of 310 mm. This geometry fulfills the requirement to not diminish the KATRIN

---

<sup>3</sup>STAHL-ELECTRONICS, Dr. Stefan Stahl, Kellerweg 23, 67528 Mettenheim, Germany.

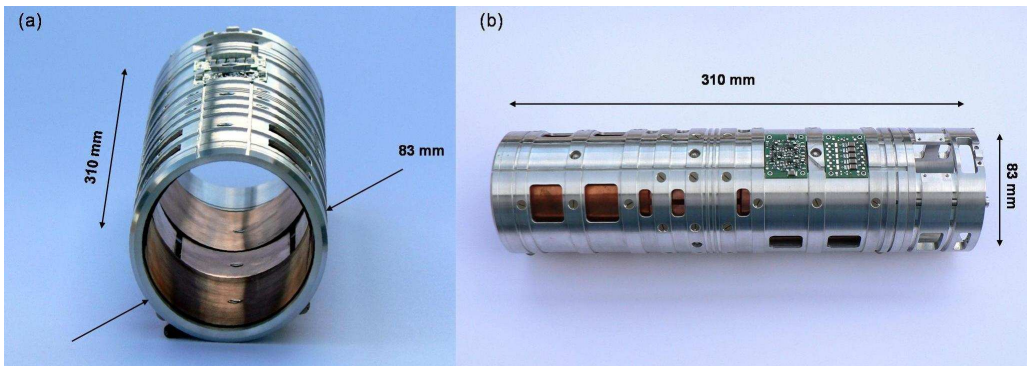


Figure 5.8: (a) Front view of the Penning trap in use. (b) Side view of the Penning trap where the preamplifier and the DC-filter can be seen attached to the trap structure.

flux tube diameter and thus do not restrict the flow of tritium-emitted  $\beta$ -decay electrons. Some modifications of the outer structure were done for solving last minute issues concerning the KATRIN beamline diameter, more details will be given in section 7.1.

The material for the outer structure of the trap is a magnesium-aluminum-alloy and the electrodes are made of oxygen-free copper and have a thickness of 1 mm. The electrodes were covered first with a  $50\ \mu\text{m}$  layer of silver and then with a  $0.5\text{-}1\ \mu\text{m}$  layer of gold. This treatment to the electrodes is done in order to avoid surface oxidation and achieve a better conductivity. The spacers used as isolators between the aluminum support and the electrodes as well as the screws are made of PEEK (Polyetheretherketone), an organic polymer thermoplastic. Outgassing tests at cryogenic temperatures of the Penning traps and all the materials composing it will be presented in section 6.9. Attached to the trap structure a DC filter and a preamplifier are installed. A detailed description will be given in section 5.5.3, as well as for the postamplifier.

## 5.5 Destructive and non-destructive ion detectors

### 5.5.1 Faraday cup

A home made Faraday cup was used at the exit of the Penning trap to count the ions, see figure 5.9. The idea of using a Faraday cup came up in order to be able to count the total number of trapped ions. The advantage of the Faraday cup (FC) compared to the microchannel-plate detector (MCP) is that the first one can be used close to the homogeneous region of the

superconducting magnet, avoiding thus that the ions get lost by following the magnetic field lines and hence not reaching the detector. However, for some other tests an MCP detector was also installed at the exit of the magnet.

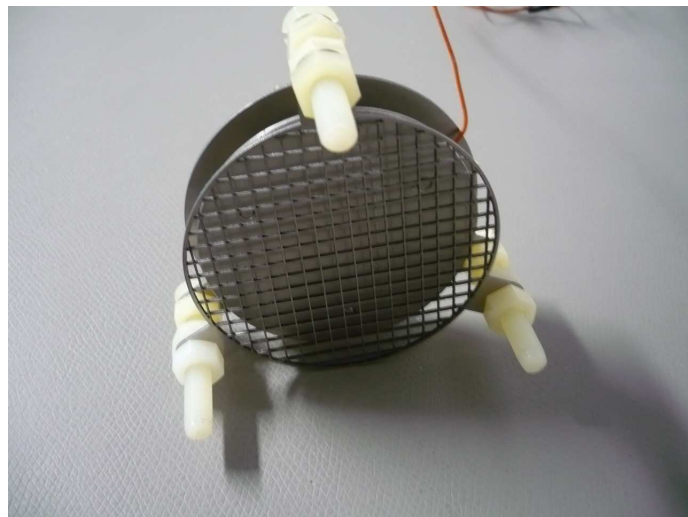


Figure 5.9: Home made Faraday cup, with a grid in front of it, used for ion counting.

The designed Faraday cup has a diameter of 65 mm, a bit smaller than the inner diameter of the Penning trap. In front of the Faraday cup, a grid was mounted to repel the secondary electrons. The electron current was amplified by a quick charge amplifier which amplifies the received pulsed ion current (QCP from Stahl Electronics) since ions were released as bunches from the trap.

The charge amplifier was calibrated measuring first the amplification with a  $4 \text{ mV}_{pp}$  sinusoidal signal, which results in an amplification of 525. In order to perform the calibration, parallel to the Faraday cup and to the amplifier a  $1.15 \text{ pF}$  capacitor with a function generator in line is inserted, the circuit is shown in figure 5.10. A  $5 \text{ kHz}$  sinusoidal signal with  $600 \text{ mV}_{pp}$  was applied resulting in a charge of  $Q = C \cdot U = 0.69 \text{ pC}$  on the capacitor. The output voltage of the amplifier ( $2.324 \text{ V}_{pp}$ ) was measured and divided by the amplification. Using  $C = \frac{Q}{U}$  the capacity of the Faraday cup was determined to be  $155.4 \text{ pF}$ . Finally the resulting sensitivity of the amplifier is  $5.34 \text{ mV}$  per  $10^3$  ions.

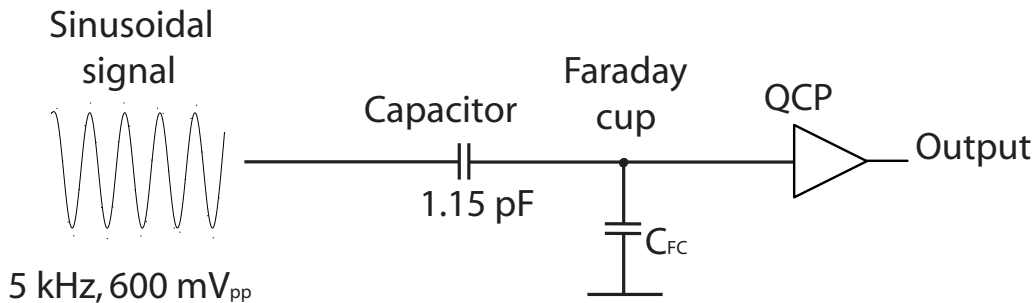


Figure 5.10: Sketch of the circuit used for calibrating the QCP.

### 5.5.2 Microchannel-plate detector

A microchannel-plate detector (MCP) [61] was used in the setup as an ion counting device. This kind of detector is based on secondary electron multipliers, meaning that the signal is originated by the multiplication of the secondary electrons coming from the collision of the ions with the coated surface of a lead silicate glass of a microchannel.

A microchannel-plate detector is composed of several millions of individual channels that work independently as secondary electron multipliers. This two-dimensional periodic array of very-small glass capillaries (channels) is fused together and sliced in a thin plate. A single incident particle enters a channel and emits an electron when hitting the channel wall. Secondary electrons are accelerated by a voltage applied across both ends of the microchannel plate. They travel along their parabolic trajectories until they strike the channel surface, thus producing more secondary electrons. This process is repeated many times along the channel; as a result, this cascade process yields to a cloud of several thousand electrons, which emerge from the rear of the plate. The resulting amplification factor is typically around  $10^4$  [62]. Figure 5.11 shows the structure of the multichannel plate and its operation. Since a typical gain of  $10^6\text{-}10^8$  is needed to obtain a clear signal at the anode two MCP plates are typically used on top of each other in a so-called Chevron-type configuration.

The used MCP, a DLD 40/2 from Roentdek, has an outer diameter of 46 mm and an active diameter of 42 mm, it was mounted onto a CF-160 flange. The detector consists of a pair of MCPs in Chevron configuration, where ceramic isolators are used in between plates to avoid contact. The set of voltages applied to the detector were: -2.8 kV to the front MCP, -1.5 kV to the middle MCP and 450 V to the anode plate. The full specifications of the used MCP given by the manufacturer can be seen in table 5.1.

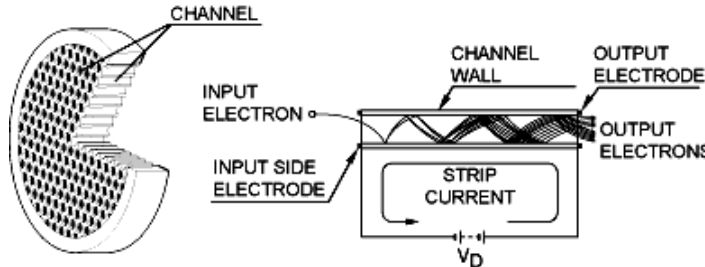


Figure 5.11: Sketch of an MCP detector with its honeycomb channel structure. A schematic of the electron cascade is also shown. Picture from [63].

### 5.5.3 FT-ICR detector

For detecting the induced image current of the trapped ions via the FT-ICR method an amplifying system is needed. The trapped ions induce a current on the electrodes in the order of picoamperes depending on the number of ions and the ions' oscillation amplitude, which is not possible to observe without any amplification. To this purpose the system described here has a two stage amplification system. The first stage amplifier, a preamplifier, is directly attached to the housing of the trap and then wired to the detection segment of the ring electrode. The second amplification is done via a postamplifier, which is attached to the outer side of a vacuum flange.

#### Preamplifier

A two channel preamplifier is implemented directly on top of each trap structure, being attached to the corresponding ring electrodes. They are located inside a UHV vacuum chamber and are designed to operate at KATRIN in an environmental temperature of roughly  $T = 77\text{ K}$ . The purpose of the preamplifiers is to amplify the weak ion current up to a sufficiently high signal level, which is meant to bridge the remaining distance between trap and vacuum feedthroughs before further amplification is possible. A dedicated broadband ( $f_{max} = 50\text{ MHz}$ ) low-noise design has been implemented, incorporating high impedance input stages with GaAs (gallium-arsenide) field effect transistors and a subsequent buffer output stage (see figure 5.12). Since the ions represent a high impedance signal source, a field effect transistor input stage with low input current noise is required. The choice of gallium-arsenide active semiconductor components fulfills these conditions and provides the advantage of full cryogenic operability even in high magnetic fields up to many Teslas. A disadvantage is caused by the fact that strong selection of

Characteristic	
Mounting flange size	CF-160
Baking temperature	150°C
# of MCPs in stack	2
Outer diameter	46 mm
Active diameter	42 mm
Aspect ratio (Length-to-Diameter ratio)	80:1
Thickness	1 mm
Pore size	12.5 $\mu\text{m}$
Center-to-center spacing	32 $\mu\text{m}$
Bias angle	$13^\circ \pm 1^\circ$
Open area ratio	>60%
Operating temperature range	-50 to 70°C
Operating pressure	<2·10 <sup>-6</sup> mbar

Table 5.1: MCP specification list given by the manufacturer.

components is necessary to obtain sufficiently low-noise in the low frequency region below 3 MHz because of so-called  $1/f$ -noise. The preamplifiers are auto-biased, which means that only a single supply line ( $3.9 \text{ V}_{DC}$ ) is needed to operate them. A picture of one of the preamplifiers can be seen in figure 5.13(a).

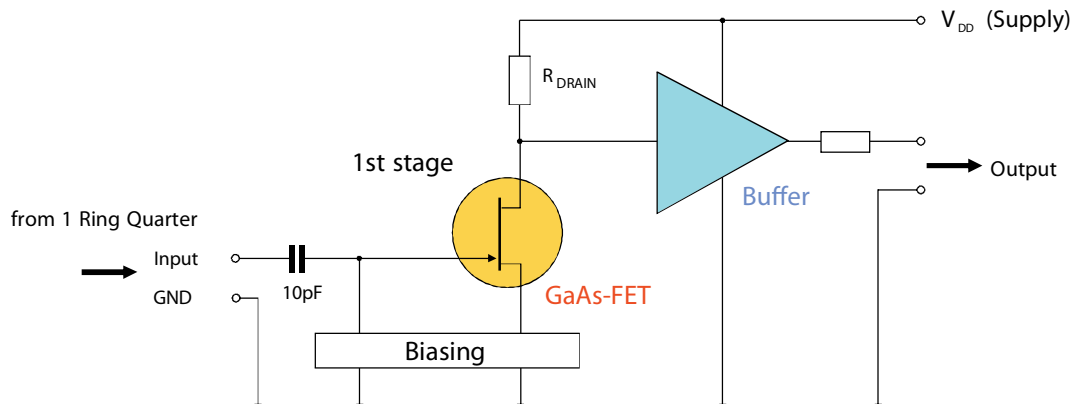


Figure 5.12: Simplified diagram of one preamplifier channel. Courtesy of Stefan Stahl.

The main preamplifier characteristics are listed below:

Frequency Range (-3 dB): 0.5 to 50 MHz

Voltage Amplification (w/o termination): typ. x 6

Power Amplification : 45 dB @ 5 MHz

Input Impedance :  $1\text{ M}\Omega // 6\text{ pF}$

Output Impedance :  $75\text{ }\Omega$

Input Voltage Noise Density : typ.  $1\text{ nV}/\sqrt{\text{Hz}}$  @ 5 MHz, 300 K

Power Dissipation : typ. 15 mW per channel

## Postamplifier

After the low-level ICR ion signals have been amplified by the in-vacuum preamplifier stage directly at the ion trap and are transported through coaxial lines to vacuum feedthroughs, a second amplifier stage follows (shown in figure 5.13(b)). Most of the (voltage) amplification factor can be credited to this second amplifier stage rather than the trap stage. It is implemented in high-frequency silicon technology and allows for a 100-fold voltage amplification (open output measurement). Corresponding to the two pickup electrodes at the trap, two independent channels are provided, which are located directly at the metal base of the vacuum feedthroughs in order to minimize possible influence of external noise. In case a dipolar pickup signal will be analyzed, a passive differential-to-single-ended converter forms a differential signal from the two individual channels. The postamplifiers can withstand moderate magnetic fields (max. up to 25 mT) and were shaped into two different case styles, to best suit the test setup in Heidelberg, or finally the setup at the KATRIN beam line. Both versions show nearly identical electrical characteristics but differ in their outline geometry. Apart from signal amplification, the purpose of this room temperature stage is to supply the in-vacuum preamplifiers with operating power and to monitor their correct working point. The latter is indicated by green light on a LED indicator for each channel, in case the output offset of the trap preamplifier stages reside within a certain voltage interval. A lack of this test signal gives the user a first hint on possible malfunctions. The postamplifiers are supplied by a standard external  $+/-5\text{ V}$  voltage source and need no further adjustments.

Main characteristics:

Frequency Range (-3 dB): 0.25 to 60 MHz

Voltage Amplification (w/o termination): typ.  $\times 100$

Power Amplification: 26 dB @ 5 MHz ( $50\text{ }\Omega/50\text{ }\Omega$ )

Input/Output Impedance:  $50\text{ }\Omega$  nominally

Input Voltage Noise Density: typ.  $1.6\text{ nV}/\sqrt{\text{Hz}}$  @ 5 MHz, 300 K

Number of channels: 2

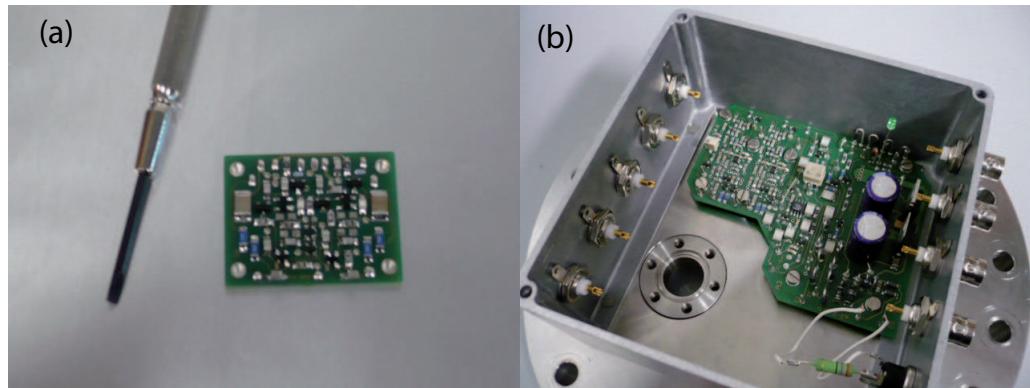


Figure 5.13: Photos of the preamplifier (a) and the postamplifier (b).

## 5.6 Control system

The control of almost all the hardware components and the data acquisition system needed for the ion manipulation and detection is done remotely using a PC. For the results that will be presented in the next chapter two different control systems were used. The one used for the majority of the measurements is based on a transient recorder controlled via a self-developed LabVIEW program. The other one, used for the selected-ion-detection measurements, will be used in the KATRIN experiment, and uses a multichannel downconverter and a low frequency range fast Fourier transform analyzer. The external trigger controlling both control systems is done via a pulse delay generator which is not controlled automatically but manually. This pulse delay generator is used for controlling the complete timing sequence of the experiment. Both control systems will be described in the following.

### 5.6.1 Transient recorder control system

The control system described here uses a transient recorder for the data treatment, function generators for the ion motion excitation and a PC for monitoring. The core of this control system is a self-developed LabVIEW program which is used for controlling both the ion excitation and the ion detection. Figure 5.14 shows a flowchart of the full process that occurs since the ions are trapped until their monitoring, the steps are marked with letters in the diagram. The main functions of the program are the following.

- Controlling the function generators: steps (A) and (B) in figure 5.14.

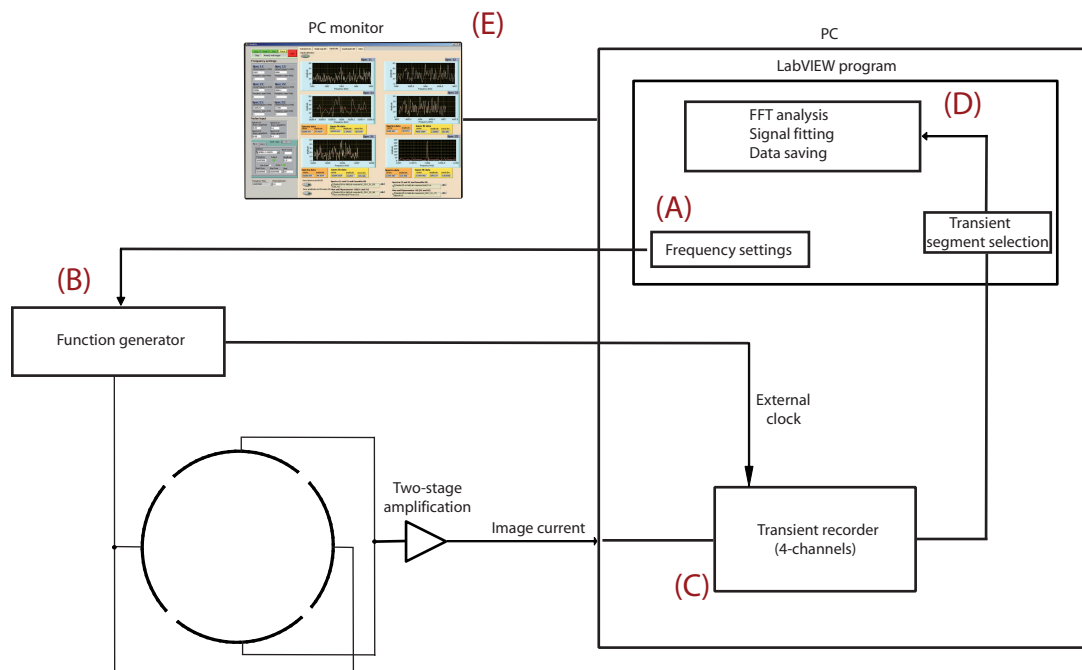


Figure 5.14: Flowchart of the process of the ion excitation and detection when using the transient recorder setup. For details see text.

- Setting the transient recorder parameters: step (C).
- Treatment of the ion signals and fast Fourier transformation: step (D).
- Data saving and plotting: step (D) and (E).

In figure 5.15 a screenshot of the graphical users interface of the program is shown, numbers are added on it for a better understanding of the explanatory text. The program contains five different tabs each of them with a specific function.

- **Transient recorder tab.** The two signals coming from each of the channels of the postamplifier are fed into two different channels of the four channel PCI-based transient recorder (FastCom Tec<sup>4</sup>, model M2i.3026). The length of the transient signal, the trigger settings, the clock speed and the sampling rate can be chosen here.

---

<sup>4</sup>FAST ComTec Communication Technology GmbH Grünwalder Weg 28A, 82041 Oberhaching, Germany.

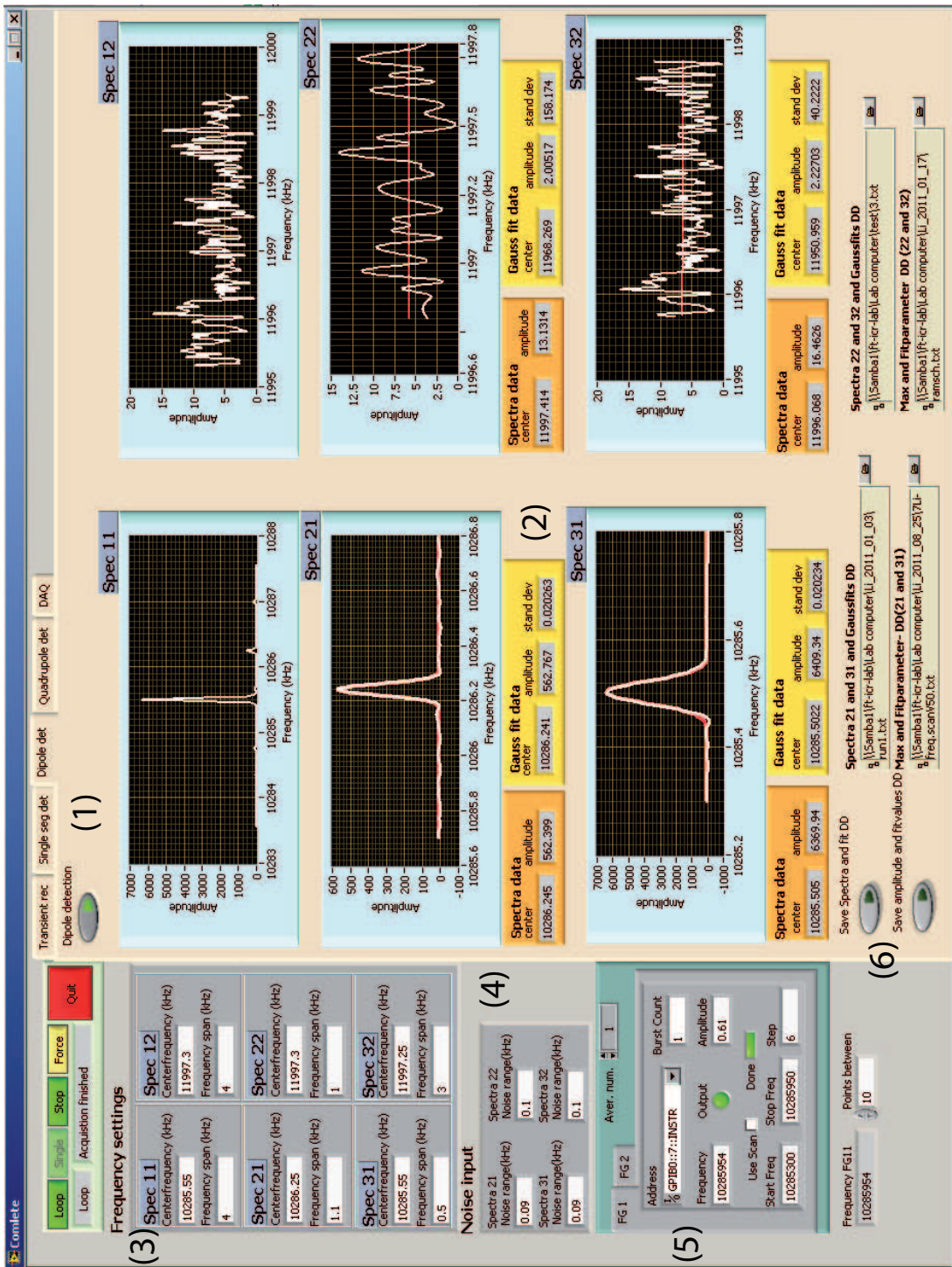


Figure 5.15: Graphical user interface screenshot. See text for more details.

- **Single segment detection tab.** Within this tab it is possible to see the induced image current in each of the detection segments separately.
- **Dipolar detection tab.** The induced image current fed into two channels of the transient recorder are subtracted here, and thus a dipolar detection is done.
- **Quadrupolar detection tab.** The induced image current fed into two channels of the transient recorder are added here, and thus a quadrupolar detection is done.
- **Controlling the function generators.** The function generators used for exciting the trapped ions are controlled remotely via the LabVIEW program.

Each of the tabs can be activated or deactivated independently affording then that only the desired action is processed.

The program has six different plot panels (shown as (1) in figure 5.15) used for monitoring the FT-ICR signals (white line in the graphs shown in figure 5.15) and provides also a Gaussian fit (red line in the graphs in figure 5.15). Four of those plot panels have an indicator (number (2) in the figure) showing the center frequency and the amplitude of the maximum peak in each panel. The center frequency and the span shown in each of the panels are chosen via the “Frequency settings” (shown as (3)) control that can be found in the upper left part of the window. We are then able to choose the transient segment we are interested in. This way, the FFT can be done there without working with the whole transient length.

The “Noise input” control (shown as (4)) in the middle left of the window is used to assign a noise base line to the Gaussian fit thus making the fit to converge faster.

In the lower left corner of the window, a control for the function generators can be found (marked as (5)). Here the program can be used to control two different devices. It is possible to set the duration of the excitation pulse, its amplitude and its frequency, and also to perform frequency (amplitude) scans, setting the initial and the final frequency (amplitude) and the step size.

Finally in the lower middle and right part of the program window two different option for saving the data is shown (marked as (6)). One of them saves the whole spectra and their fit, while the other saves the center frequency and the maximum amplitude for both the spectra and their Gaussian fit.

### 5.6.2 Downconverter control system

For the ion selected measurements performed in this thesis and, most important, the selected-ion-excitation/detection measurements that will be performed in the KATRIN experiment a different control system than the one previously described will be used. This control system is described in the following.

Figure 5.16 shows a complete scheme of the excitation and detection procedure for these measurements. In this case the excitation of the ion motion is done via SWIFT (as it was already explained in chapter 2), a function generator TABOR WW1071 is used for that purpose. With a self-developed user program one can choose the frequencies that want to be excited, the span and the amplitude of the excitation.

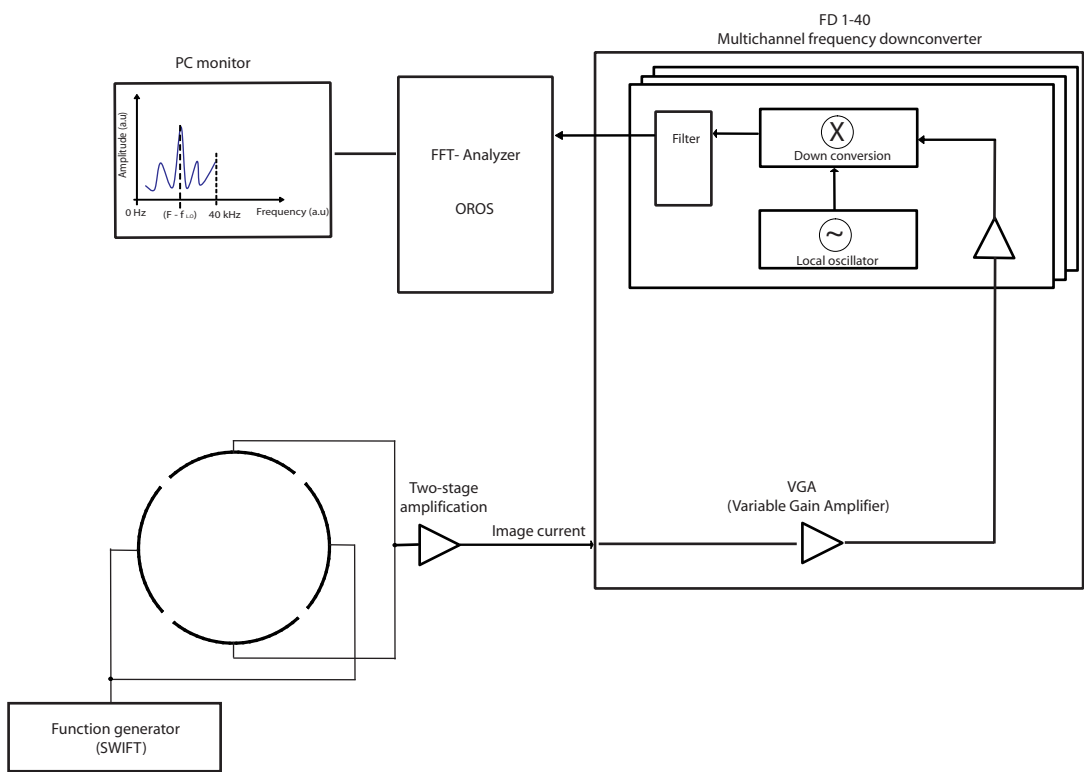


Figure 5.16: Flowchart of the process of the ion excitation and detection when using the downconverter setup. For details see text.

In order to read out the induced image current signal created by the trapped ions a multichannel frequency downconverter and an FFT analyzer are used. The frequency down converter (FD 1-40 developed by Stahl Elec-

tronics) is intended to downconvert the high frequency signals down to a lower frequency range (from 2 to 40 kHz). The amount of frequency offset is defined by internal local oscillator (L.O.) frequencies. A scheme of this process is shown in figure 5.17. The device consists of 2 input and 8 output channels, meaning that up to eight different ion species can be monitored simultaneously using this method. The downconverter is connected to a low frequency fast Fourier transform analyzer (OR35 from OROS<sup>5</sup>). This FFT analyzer covers a range from 0 to 40 kHz, for that reason the eight channels of the FFT analyzer are fed with the low frequency signals coming from the downconverter. A PC with the commercial software NVGATE is used for monitoring the signals in the frequency range provided by the FFT analyzer.

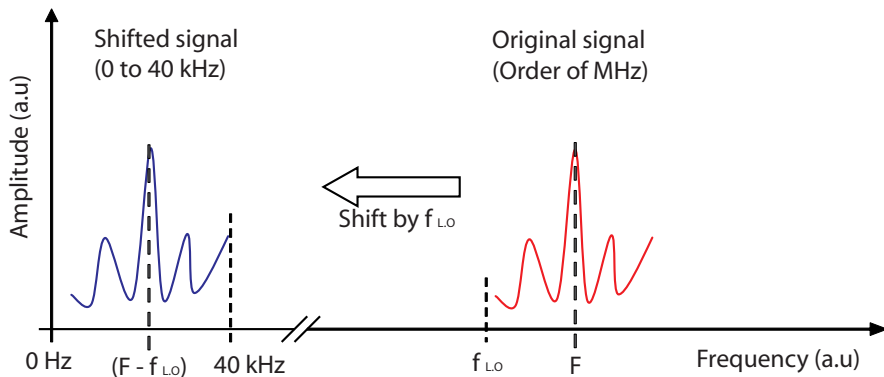


Figure 5.17: Illustration of the downconversion process. The original detected signal is shifted by an amount corresponding to the chosen local oscillator (L.O) frequency.

---

<sup>5</sup>OROS Inc. 23 Chemin Prés 38240 Meylan, France



# Chapter 6

## Results from the commissioning setup in Heidelberg

The characterization of the Penning-trap system that will be installed in the KATRIN experiment was done in the setup described in the previous chapter. It is important to characterize the system before its final installation in the KATRIN beamline since there will be no possibility of doing it afterwards. The characterization of the used amplifiers, the relation between the number of ions and the amplitude of the FT-ICR signal and the simultaneous detection of several ion species are, among others, some of the results presented here.

### 6.1 Preamplifier and postamplifier tests

The amplifier system described in section 5.5.3 was used to obtain the results shown in the following sections of this chapter. Prior installation of the electronics for the ion image current amplification, the behavior of both the pre- and the postamplifier was tested at different frequencies. Within this section the obtained results of these tests will be discussed.

Figure 6.1 shows the voltage amplification for each of the amplifiers as a function of frequency between 0.1 and 50 MHz. The amplification of the preamplifier (left panel) is about 6.5 for frequencies between 1 and 70 MHz. The postamplifier (right panel) shows a voltage amplification of a factor of 27 in the region between 1 and 11 MHz. Both amplifiers show the expected value and they provide sufficient amplification, when enough number of ions, to observe an FT-ICR signal in the range of frequencies of interest for the tests performed here.

Figure 6.2 shows the results of the noise tests performed for the pream-

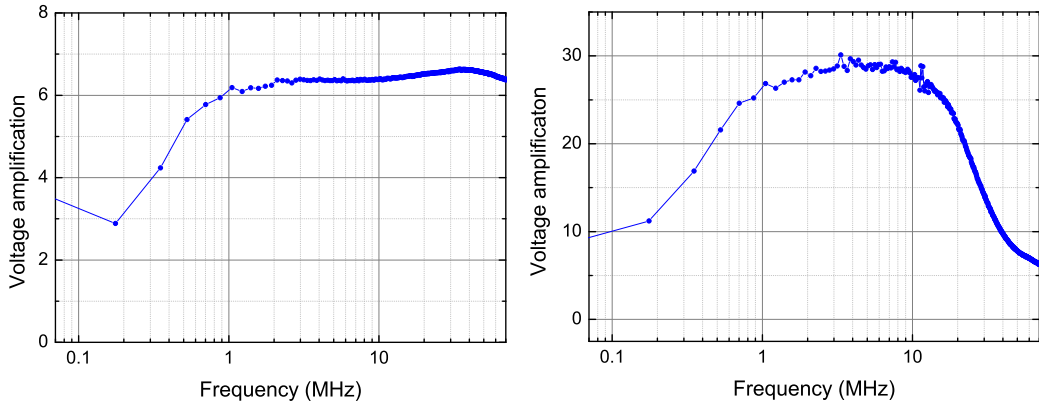


Figure 6.1: Voltage amplification factor as a function of frequency for the preamplifier (left) and the postamplifier (right).

plifier, each of the panels shows the results for the two different channels of the preamplifier. The left panel in figure 6.2 shows the results for the voltage noise density as a function of the frequency, yielding a value of  $\approx 1 \text{ nV}/\text{Hz}^{1/2}$  around 10 MHz. An expected  $1/f$  behavior is observed. The step appearing between 7 and 10 MHz is due to some external noise and not from the amplifier itself. Unfortunately it was not possible to identify the source of the noise. The current noise density as a function of the frequency is illustrated in the right panel. These curves show a  $f^{1/2}$  behavior and a value of  $\approx 100 \text{ fA}/\text{Hz}^{1/2}$  around 1 MHz. The falling down behavior appearing around 3 MHz is due to a low pass filter inserted in front of the spectrum analyzer in order to avoid reflections at high frequencies.

Electronics tests were satisfactory by showing an amplification high enough and a noise level low enough for performing the desired tests.

## 6.2 Excitation and detection scheme

Before showing the results for the characterization of the Penning trap system, it is important to describe the timing sequence in the experiment. Figure 6.3 shows the general timing sequence for one measurement cycle. For the different results presented in this chapter the measurement cycle will look different. For that reason only a general description of the measurement cycle will be given here while the details will be given in each section.

After the ions are produced in the source and guided to the Penning trap by using the einzel lenses (see figure 5.1), they have to be captured in

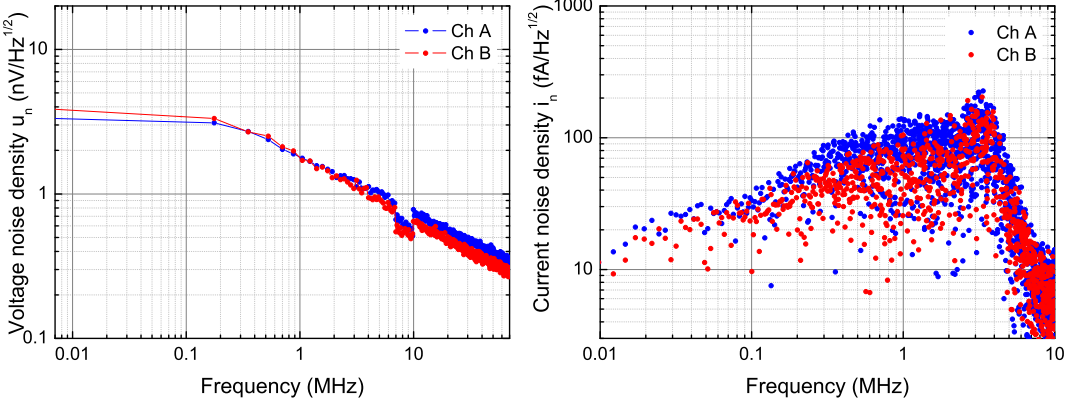


Figure 6.2: Voltage noise density  $u_n$  (left) and current noise density  $i_n$  (right) as a function of frequency for both channels (A and B) of the preamplifier.

flight in the Penning trap. To this purpose a certain voltage is first applied to the second endcap of the Penning trap, that is the endcap closer to the detector side (strong side of the magnet in figure 5.1). After a certain time called injection time, a time in which the trap is being loaded with ions, the same voltage is also applied to the first endcap (the one closer to the ion source). Once the electrostatic potential is created by the endcaps, a certain delay time could be introduced before an rf signal around one of the motional frequencies of the trapped ions is applied for the excitation of the ion motion. A delay time is introduced before the FT-ICR detection in order to avoid induced noise coming from the excitation signal. When the FT-ICR detection of the ion signal is done, the voltage applied to the second endcap is switched off. At that point the ejection of the ions occurs, meaning that they freely follow the magnetic field lines in their path to the detector. Once the ejection time has passed and the trap has been emptied, the first endcap is also brought to zero volts. The measurement cycle repeats as many times as desired.

The duration of each of the steps illustrated in figure 6.3 will be explained in each subsection depending on the performed measurement.

### 6.3 Characterization of the FT-ICR signals

First step once the ions are confined inside the trap is the characterization of the FT-ICR signal, which means finding the values of the frequencies, the amplitude and the length of the excitation that should be applied for having

## 60 Chapter 6: Results from the commissioning setup in Heidelberg

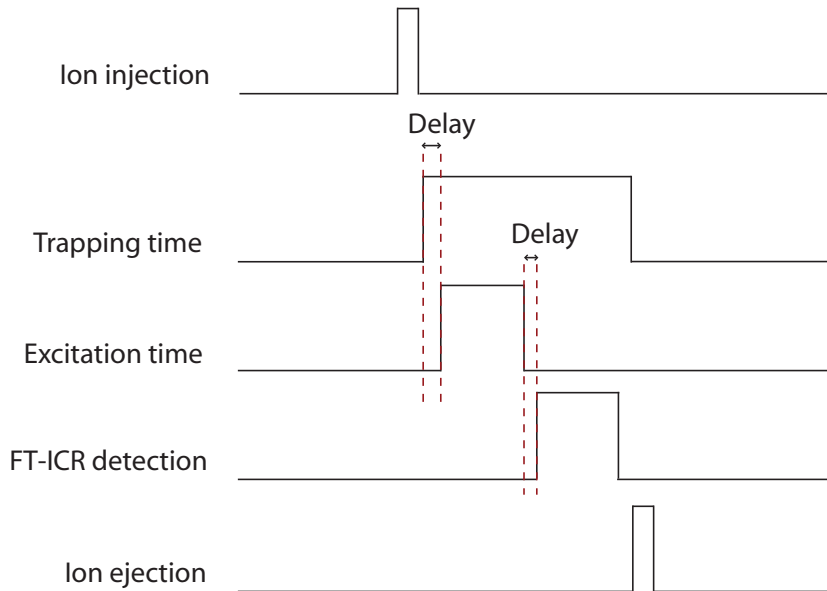


Figure 6.3: Timing scheme for trapping, excitation and detection. The size of the pulses is not drawn to scale. See text for more details.

a proper signal. To this end several scans need to be done. The scans are performed around the expected modified cyclotron frequency of the trapped ions, in this case the cycle presented in figure 6.3 is repeated several times applying in each of the cycles a different excitation frequency. The excitation amplitude is then scanned in small steps from  $1\text{ V}_{pp}$  to  $10\text{ V}_{pp}$  using a fixed excitation frequency on resonance. Measurements with different excitation times are also performed until the most convenient is found.

Figure 6.4 [64] shows the results of frequency scans for two different ions species,  ${}^4\text{He}^+$  and  $\text{H}_2\text{O}^+$ . The ions were created using the electron impact ion source described in section 5.2.2 together with an electronic gas inlet system used for flushing the system with the desired gas to ionize ( ${}^4\text{He}$ ). For these two measurements the endcap voltage was kept at 60 V and the frequency step size was 50 Hz. In these measurements the injection had a duration of  $100\text{ }\mu\text{s}$ , the trapping time was 100 ms and the ejection was  $100\text{ }\mu\text{s}$ . The acquisition time of the image current signal was 5 ms.

The amplitude of the induced FT-ICR signal at the modified cyclotron frequency  $\nu_+$  was recorded every cycle for the corresponding  $\nu_{exc}$  frequency. The duration of the excitation in each cycle was  $\approx 1.1\text{ ms}$  for  ${}^4\text{He}^+$  and  $\approx 5\text{ ms}$  for  $\text{H}_2\text{O}^+$ . The sidebands in both figures arise from the finite excitation period which has in the time domain a rectangular shape.

The mass resolving power  $m/\Delta m$  with  $\Delta m$  being the full-width-half-

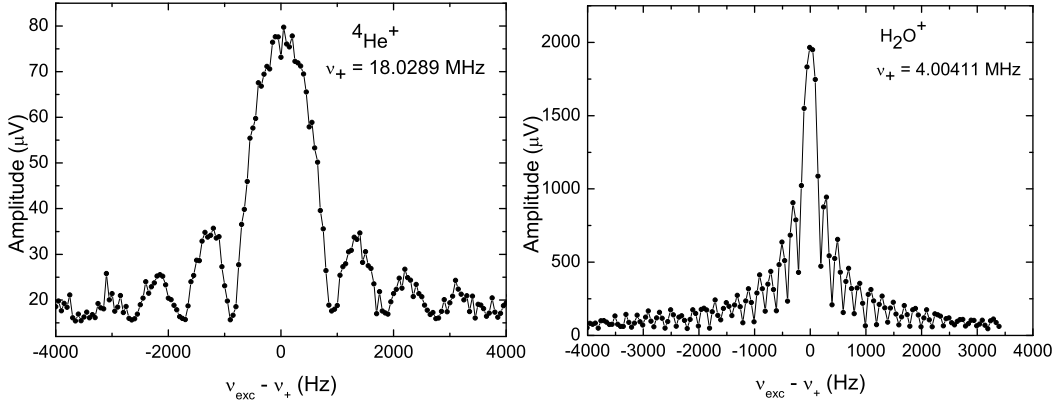


Figure 6.4: Left: amplitude of the FT-ICR signal versus excitation frequency for  ${}^4\text{He}^+$  ions ( $\Delta\nu_{FWHM}=1095 \text{ Hz}$ ). Right: amplitude of the FT-ICR signal versus excitation frequency for  $\text{H}_2\text{O}^+$  ions ( $\Delta\nu_{FWHM}=276 \text{ Hz}$ ). For more details see text.

maximum is  $1.6 \times 10^4$  for  ${}^4\text{He}^+$  ions and  $1.5 \times 10^4$  for  $\text{H}_2\text{O}^+$  ions, respectively. Measurements with  ${}^4\text{He}^+$  were also performed for a longer excitation time of  $\approx 5.5 \text{ ms}$ , resulting in a resolving power of  $7.2 \times 10^4$ . A resolving power of  $1.6 \times 10^5$  will be required in the KATRIN experiment to distinguish  $\text{T}^+$  from  ${}^3\text{He}^+$  ions in the frequency spectrum. This will be possible by choosing a proper excitation time of about 10 ms in case the rest gas pressure at the trap position allows it. Measurements on the coherence time as a function of the pressure will be discussed later. The modified cyclotron frequencies  $\nu_+$  for the two ion species shown in figure 6.4 are  $18.0289(11) \text{ MHz}$  for  ${}^4\text{He}^+$  ions and  $4.00411(28) \text{ MHz}$  for  $\text{H}_2\text{O}^+$  ions.

This process for the characterization of the FT-ICR signal was done for each of the used ion species presented in this thesis.

## 6.4 Magnetic field measurement with trapped ions

One of the most important measurements performed was the measurement of the magnetic field seen by the trapped ions. In this case the ions were created using the electron impact ion source and flushing the system with  ${}^4\text{He}$  gas. The length of the excitation and the trapping time were the same ones as in the previous section, as both measurements were taken in consecutive days.

In order to perform this measurement the FT-ICR signal at  $\nu_{\text{exc}} = \nu_+$

## 62 Chapter 6: Results from the commissioning setup in Heidelberg

was recorded for different potentials  $U$  applied to the endcap electrodes. Figure 6.5 shows the modified cyclotron frequency for  ${}^4\text{He}^+$  as a function of the voltage applied to the endcaps. The red solid line is the result of a least-square linear fit following the relationship:

$$\nu_+ = \nu_c - \nu_- = \frac{q \cdot B}{2\pi m} - \frac{U}{4\pi d^2 B}, \quad (6.1)$$

which is obtained from equation (2.11) by substituting  $\nu_c$  and  $\nu_-$ .

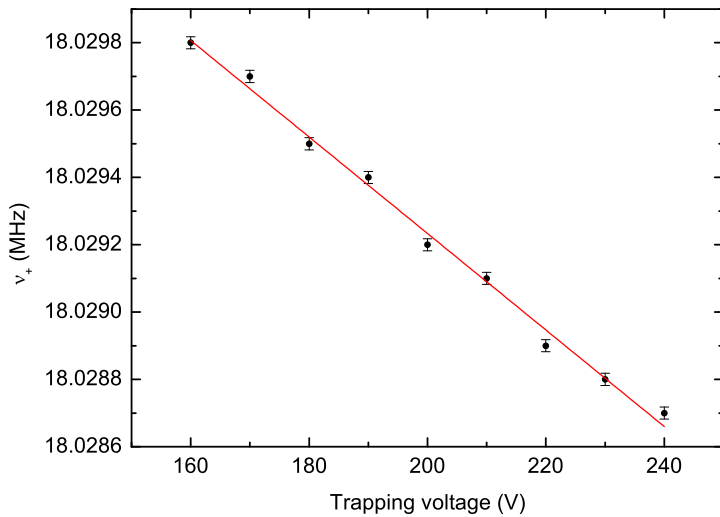


Figure 6.5: Modified cyclotron frequency for  ${}^4\text{He}^+$  ions as a function of the trapping voltage. A relative uncertainty of  $10^{-6}$  due to the magnetic field inhomogeneities and due to the large motional radii of the ions was added to the modified cyclotron frequencies.

Applying a linear fit to the data shown in figure 6.5 and using the mass value for  ${}^4\text{He}^+$  given by [65], one can obtain the magnetic field from the first term in equation (6.1) as  $B_{He} = 4.6995(2)$  T. This calculated value agrees very well to the obtained value from the NMR measurement shown in section 5.1, which has a value of  $B_{NMR} = 4.6993(2)$  T. The characteristic parameter  $d$  of the trap can be calculated from the second term in equation (6.1), resulting in a value of  $d_{He} = 3.43(2)$  cm.

The same measurements as above were performed using water ions yielding to the following values,  $B_{H_2O} = 4.6996(6)$  T for the magnetic field and  $d_{H_2O} = 3.48(2)$  cm for the characteristic parameter.

Table 6.4 shows a summary of the obtained data for the magnetic field value calculated from the trapped ions as well as from the NMR measurement. The characteristic parameter  $d$  is listed as well.

Table 6.1: Values obtained for the magnetic field  $B$  from cyclotron frequency measurements with trapped ions. The calculated characteristic parameter  $d$  is also given.

	${}^4\text{He}^+$	$\text{H}_2\text{O}^+$	NMR
B (T)	4.699 5(2)	4.6996(6)	4.699 3(2)
$d$ (cm)	3.43(2)	3.48(2)	—

Additional studies of the ion frequency response to different trapping potentials were done at this setup and results were presented in [66].

This same measurement can be done in the KATRIN experiment in order to monitor the magnetic field provided by the coils at the trap position. As the idea is to test the Penning trap in the KATRIN beamline first using a test ion source (see section 5.2.3), a magnetic field measurement at the trap position will be done using ion species with well known mass (e.g.  ${}^4\text{He}^+$  or  $\text{N}_2^+$ ). After this measurement the magnetic field at each of the trap positions will be well known making more suitable the calculation of the reduced cyclotron frequencies for the expected ion species coming from the tritium source.

## 6.5 Coherence time measurements

When the trapped ions are excited at one of their eigenfrequencies the ion cloud moves coherently. After a certain time the cloud loses its coherent motion due to several reasons, such as the magnetic field inhomogeneities, the ion-ion interaction and collisions with the rest gas. For how long the ions remain excited and moving with a coherent motion inside the trap is called coherence time.

The study of the length of the coherent motion done as a function of the pressure inside the vacuum chamber and as a function of the excitation time is presented in this section. These measurements will guide the users of the Penning trap system in the KATRIN experiment to choose a suitable detection time depending on the pressure condition at each of the trap positions.

Figure 6.6 shows a scheme of how these measurements were performed. First the ion motion is excited around the frequency  $\nu_+$  for a certain time,

## **64 Chapter 6: Results from the commissioning setup in Heidelberg**

after that and before reading the image current induced by the trapped ions (ion response in figure 6.6), a delay is applied. Varying this delay we are able to see how the amplitude of the FT-ICR decreases with time.

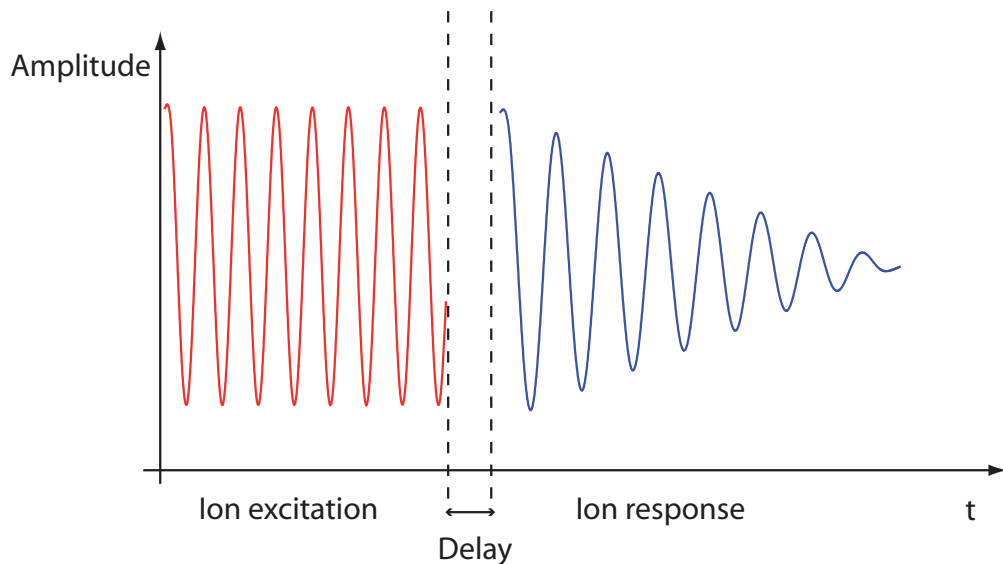


Figure 6.6: Sketch showing how the coherence time measurements were done. After the ion excitation a delay time is introduced before the signal acquisition. The ion coherence decays exponentially with time.

In this section results of the coherence time varying two different parameters, namely the pressure and the excitation time, will be presented.

Figure 6.7 shows the coherence time results for two different excitation times for  ${}^7\text{Li}^+$  ions, using for their creation the surface ion source. During these measurements the pressure inside the vacuum chamber was  $2 \times 10^{-7}$  mbar. In these measurements the ion motion was excited at the reduced cyclotron frequency ( $\approx 10.2855$  MHz) with an amplitude of  $2.5 \text{ V}_{pp}$ , no magnetron excitation was applied. The loss of the coherence was calculated by fitting the experimental data with an exponential decay (red solid line in figure 6.7), and the decoherence time is given by the decay constant in the fitting function. When the ion motion is excited for 6.8 ms the coherence time is  $\approx 28$  (2) ms, and when the excitation length is 10.7 ms the coherence time is  $\approx 25$  (1) ms. The faster loss of coherence for longer excitation times could be explained by the fact that longer excitation times result in an increased motional radius of the ion cloud thus resulting in a larger number of collisions with the rest gas.

The measurement of the coherence time of the ion motion at different pressures is a measurement of utmost importance for the future installation

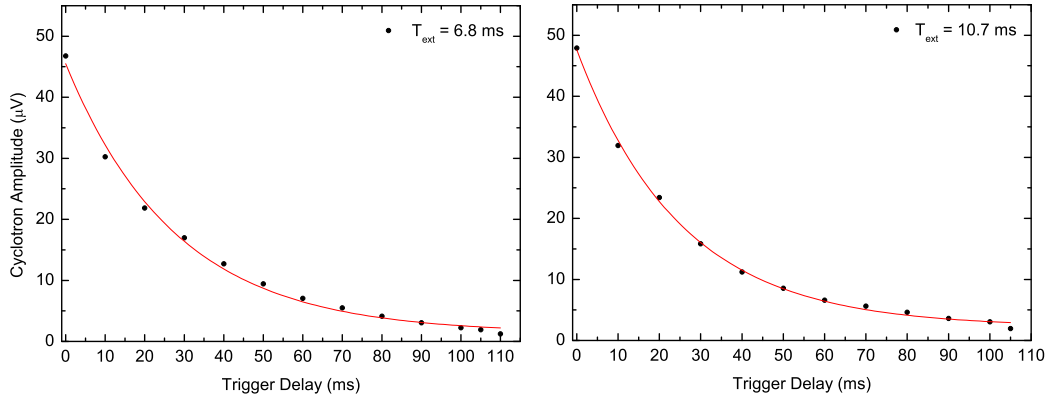


Figure 6.7: Coherence time measured for different excitation times using  ${}^7\text{Li}^+$  ions. For the measurement with an excitation duration of 6.8 ms (left panel) the coherence time is 28 (2) ms. With an excitation length of 10.7 ms (right panel) the coherence time is 25 (1) ms. Both measurements were done at a pressure of  $2 \times 10^{-7}$  mbar.

of the Penning trap system inside the KATRIN experiment. At the positions where the Penning traps will be installed in the KATRIN experiment a range of pressures between  $10^{-5}$  and  $10^{-9}$  mbar is expected. In order to study how the ions inside the Penning trap behave as a function of the pressure, the procedure shown in figure 6.6, was repeated for different pressures.

Figure 6.8 shows the coherence time measurement done at a pressure lower than  $5 \times 10^{-9}$  mbar<sup>1</sup>. For these measurements first the magnetron motion of the ions was excited for 24 ms and after that the reduced cyclotron frequency for  ${}^7\text{Li}^+$  ions was applied during 38 ms. Making an exponential decay fit (red solid line in figure 6.8) of the obtained data one gets a coherence time of  $\approx 172$  (15) ms for this pressure value.

Since the two Penning traps that are planned to be installed in the KATRIN beamline will be placed at different positions and thus at different pressures, additional coherence time measurements were done in order to find the highest pressure limit at which it is still possible to work with an FT-ICR signal, results are shown in figure 6.9. For these measurements the ions were created using the photocathode ion source (see section 5.2.3) and flushing the system with nitrogen gas until the desired pressure is achieved. The red solid line in both plots shows an exponential decay fit to the data.

<sup>1</sup> $5 \times 10^{-9}$  mbar is the lowest value that can be detected by the pressure gauge used in the experiment, so is not possible to give a precise value of the pressure for this measurement.

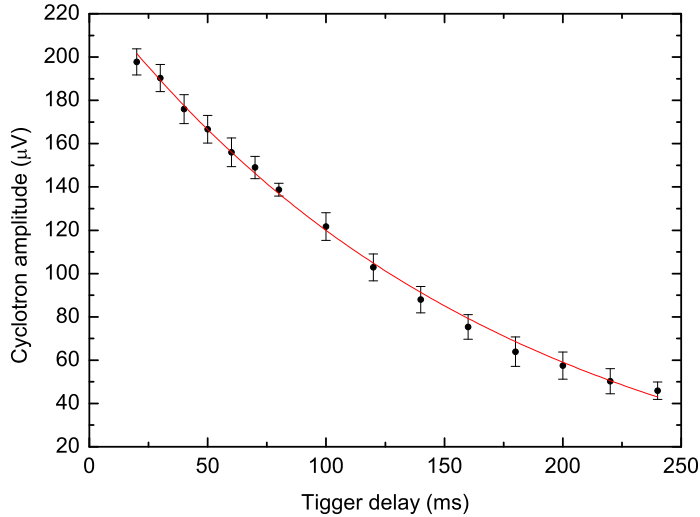


Figure 6.8: Coherence time at a pressure  $< 5 \times 10^{-9}$  mbar. The ion coherence time was found to be  $\approx 172$  (15) ms in this measurement using an exponential fit.

These two measurements simulate the pressures expected at the traps positions in the KATRIN experiment. Measurements were done at  $\approx 2 \times 10^{-5}$  and  $\approx 8 \times 10^{-6}$  mbar, giving decay times of 1.5 (0.1) and 3.0 (0.1) ms respectively. As it was expected the coherence time shortens when the pressure inside the chamber increases. This behavior can be explained by the collisions of the ions with the rest gas inside the vacuum chamber.

## 6.6 Selected-ion-detection

Selected-ion-detection tests were done in order to prove that it is possible to explore a wide range of frequencies at the same time, as it is planned to be done at the KATRIN experiment. The data presented here covers a low as well as a high range of frequencies. To achieve this the ions were created with different ion sources for each of the measurements. For one set of data the ions were created using the photocathode ion source described in section 5.2.3 together with an electronic gas inlet system used for injecting nitrogen gas inside the chamber. The other data set was taken using the surface ion source with a mixed pellet containing  ${}^6\text{Li}^+$  and  ${}^7\text{Li}^+$  ions with natural isotropic abundance.

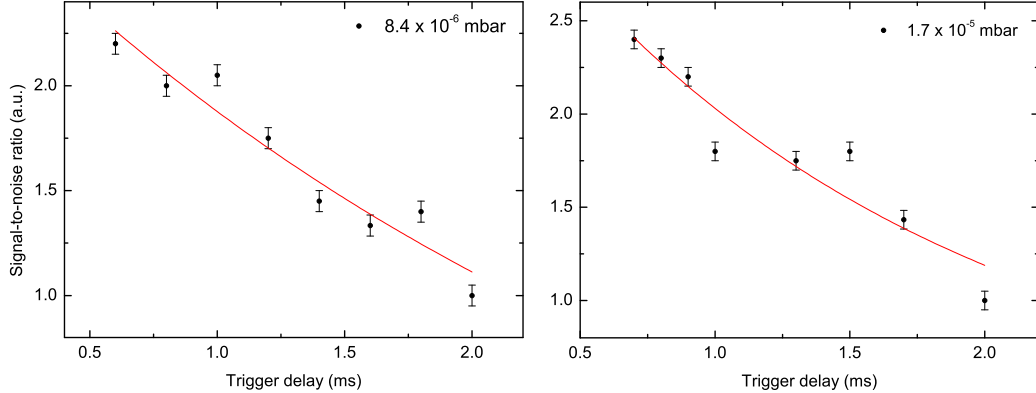


Figure 6.9: Coherence time measured at two different pressures. At  $\approx 8 \times 10^{-6}$  mbar (right panel) a coherence time of  $\approx 3.0$  (0.1) ms was found. And at  $\approx 2 \times 10^{-5}$  mbar (left panel) a coherence time of  $\approx 1.5$  (0.1) ms was measured. The red lines in both panels represent an exponential fit of the data.

In figure 6.10 one can see the data obtained using the photocathode ion source, and exciting the ions via the already mentioned SWIFT method. The data was recorded using the down converter and the low-range spectrum analyzer described in section 5.6.2, as it will be done at KATRIN. The detected ion species are coming from the flushed gas ( $N_2$ ) and from the outgassing of the vacuum chamber itself. The measured frequencies  $\nu_+$  for the different ion species detected in figure 6.10 are 4.020 01(14) MHz for  $H_2O^+$ , 3.800 27(33) MHz for  $H_3O^+$ , 2.597 51(11) MHz for  $N_2^+$  and 2.265 83(16) MHz for  $O_2^+$ . A pressure of  $1.7 \times 10^{-6}$  mbar was present inside the chamber when the measurements were performed. During these measurements a 200 V trapping potential was used. The storage time of the ions was 100 ms and the injection and ejection time was 100  $\mu$ s. The different ion species were excited between 1.3 and 2.2 ms, respectively.

Using the surface ion source with a mixed  ${}^6Li^+$  and  ${}^7Li^+$  pellet, a clean beam of ions was achieved in order to perform a broad range frequency measurement at higher frequencies than those presented in figure 6.10. Both ion species were excited simultaneously using two different function generators, each of them for exciting one of the ion species. The FT-ICR signal was recorded using the transient recorder system. The result is shown in figure 6.11. For these measurements the ions were trapped in a 60 V potential well during 180 ms, and the injection and ejection time were set to be 200  $\mu$ s. In a first step ions were excited for 5 ms at their magnetron frequency, 781 Hz,

## 68 Chapter 6: Results from the commissioning setup in Heidelberg

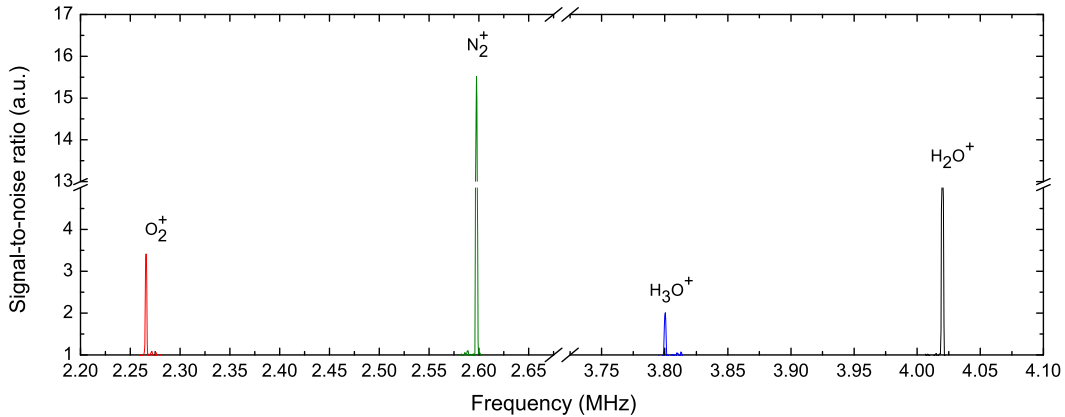


Figure 6.10: Broad-band FT-ICR spectrum obtained using the photocathode ion source and flushing the system with nitrogen gas. Four different ion species were excited with the SWIFT method and detected simultaneously.

with a  $2.3 \text{ V}_{pp}$  amplitude. Between the trapping of the ions and the magnetron excitation a delay of  $4 \text{ ms}$  was applied. Later, the  ${}^6\text{Li}^+$  ions were excited with an amplitude of  $2.6 \text{ V}_{pp}$  during  $9.1 \text{ ms}$  and the  ${}^7\text{Li}^+$  ions were excited with an amplitude of  $1.7 \text{ V}_{pp}$  during  $8.7 \text{ ms}$ . The measured reduced cyclotron frequencies are  $10.285\,518(4) \text{ MHz}$  for  ${}^7\text{Li}^+$  and  $11.997\,263(2) \text{ MHz}$  for  ${}^6\text{Li}^+$ . The spectrum also shows a third peak at  $\approx 10.285\,8 \text{ MHz}$  which was not possible to identify as a different ion species. This not identify peak might be due to a large trapped ion cloud of  ${}^7\text{Li}^+$  ions at different radius, meaning that ions at different radius respond at different frequencies.

Within this section results coming from two different excitation and detection methods were shown. The first method, the selected-ion-excitation and detection method, will be the one used in the KATRIN experiment. The results presented in figure 6.10 were done using the softwares and hardwares meant to be used in the KATRIN final setup. For the second method (results shown in figure 6.11) ions were excited simultaneously using two different function generators synchronized to each other, and the detection was done using a PC-based transient recorder. This second method is the one frequently used at the MPIK setup.

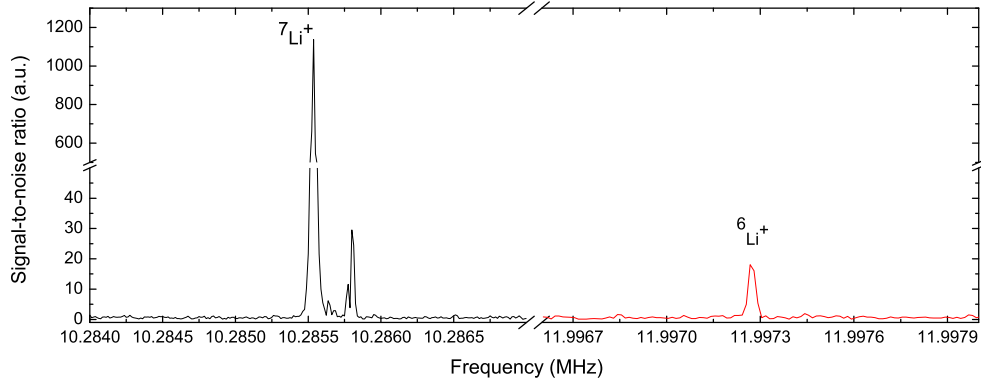


Figure 6.11: FT-ICR spectrum obtained by using the surface ion source with a pellet mixture of  ${}^6\text{Li}^+$  and  ${}^7\text{Li}^+$ . Both ion species were excited and detected simultaneously.

## 6.7 Detection limit for different ion species

A very important measurement for the characterization of the Penning trap system is the determination of its detection limit, which means the determination of the minimum number of ions needed inside the trap in order to have a visible FT-ICR signal. In the test setup at the MPIK one can use the image current detection method together with the time-of-flight method, finding that way a relation in between the amplitude of the FT-ICR signal and the number of trapped ions [67]. These detection limit measurements were performed for several ion species.

A first detection limit test was done within this thesis for  ${}^4\text{He}^+$  ions [64]. Ions were created using the photocathode ion source together with an electronic gas inlet system. The vacuum chamber was flushed with  ${}^4\text{He}$  gas in order to create the ions. After the FT-ICR detection the ions were released from the trap and detected with an MCP detector. In order to avoid the saturation of the MCP two attenuation grids were mounted in front of the detector resulting in an intensity reduction by a factor of 100. The attenuation factor of 100 was determined with transmitted laser light using a photodiode. The voltage signal from the photodiode was measured using a multimeter for both situations, *i.e.* with and without the attenuation grids in front of the MCP detector.

Figure 6.12 shows the result for the measurement with  ${}^4\text{He}^+$  ions. For this measurement the ions were excited during  $\approx 1.1$  ms around the  $\nu_+$  frequency and with an amplitude of  $2\text{ V}_{pp}$ . The y-axis of the plot shows the signal-to-

noise ratio averaged for 100 measurements and the x-axis shows the number of trapped ions per shot. The number of detected ions was corrected for the MCP efficiency of 30(5) % [61], and also for the attenuation factor of 100 coming from the grids.

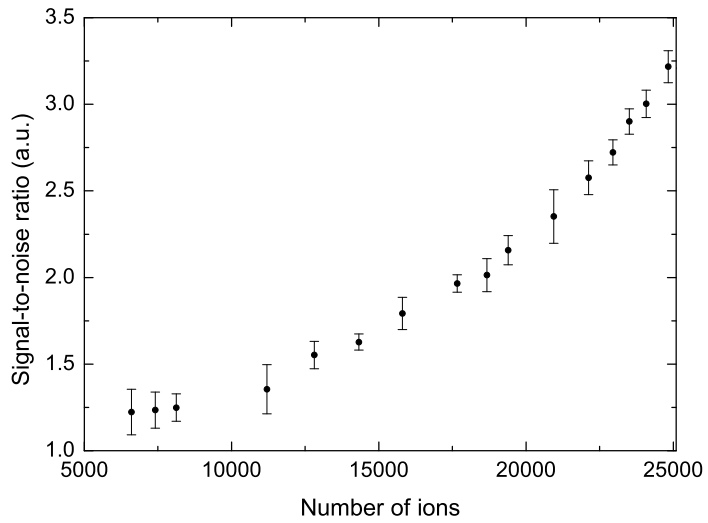


Figure 6.12: Signal-to-noise ratio versus number of ions extracted from the trap. The system was tuned so that only  ${}^4\text{He}^+$  ions were observed in the time-of-flight spectrum [64].

Figure 6.12 shows a detection limit for  ${}^4\text{He}^+$  of around 6 000 ions, meaning that a trapped ion cloud with a lower number of ions is not visible using the induced image charge method. A saturation effect on the MCP detector is observed for bunches containing more than 20 000 ions, explaining the exponential-like shape appearing in the plot. This saturation effect could be avoided by adding more attenuation grids in front of the MCP detector.

A detection limit measurement for  ${}^6\text{Li}^+$  and  ${}^7\text{Li}^+$  ions was also performed. For these measurements ions were created using the surface ion source producing  ${}^6\text{Li}^+$  and  ${}^7\text{Li}^+$  ions. After the ions were released from the trap they were detected with a Faraday cup (FC) together with the quick charge amplifier already described in section 5.5.1. In front of the FC a grid was mounted to repel the electrons possibly created on the FC. The electron current amplified by the charge amplifier was recorded with an oscilloscope. For these measurements the Faraday cup was placed  $\approx 5$  cm away from the trap in order to avoid the loss of ions on their way to the detector. The induced image

current was measured using the downconverter control system previously described in section 5.6.2. A pressure of  $\approx 7 \times 10^{-8}$  mbar was measured at the vacuum chamber during these tests.

Figure 6.13 shows the averaged measured ion voltage pulse from the trapped ions as a function of their time of flight. Each curve represents a different ion source heating current. The maximum of the voltage pulse for different currents appears always at the same time of flight, namely at  $\approx 55 \mu\text{s}$ .

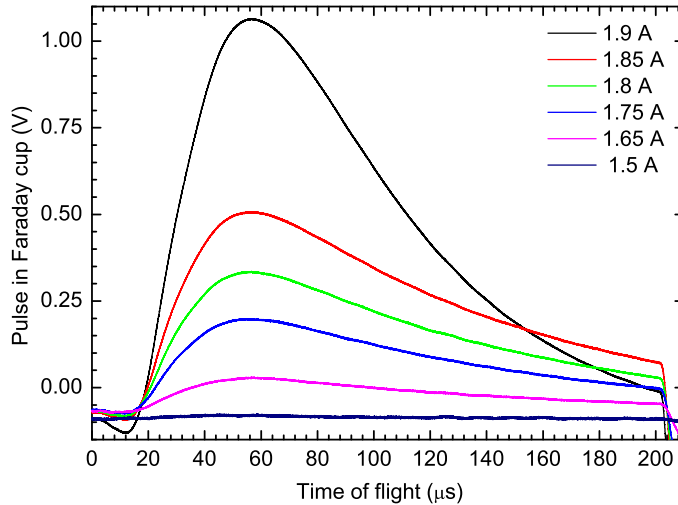


Figure 6.13: The induced amplified signal from the FC as a function of time of flight for different ion source heating currents.

From the calibration of the charge amplifier is known that  $\approx 10\,000 \text{ e}^-$  corresponds to  $\approx 5.4 \text{ mV}_{pp}$ . Thus, from the measured voltage in figure 6.13, the number of ions was calculated by considering the  $10\,000 \text{ e}^- / 5.4 \text{ mV}_{pp}$  ratio. For the smallest heater current shown in figure 6.13, which is 1.5 A, the detection limit for the charge amplifier was reached, meaning that such a low number of ions cannot be detected. The steps appearing in figure 6.13 at around  $15 \mu\text{s}$  and around  $200 \mu\text{s}$  are coming from the switching of the endcaps.

For each of the currents applied the FT-ICR signal was measured and once the ions were released the pattern shown in 6.13 was measured, from there one can obtain an ion number for each of the currents.

Figure 6.14 shows the results for the measured FT-ICR signal-to-noise ratios of  ${}^6\text{Li}^+$  and  ${}^7\text{Li}^+$  as a function of the number of ejected ions per cy-

## 72 Chapter 6: Results from the commissioning setup in Heidelberg

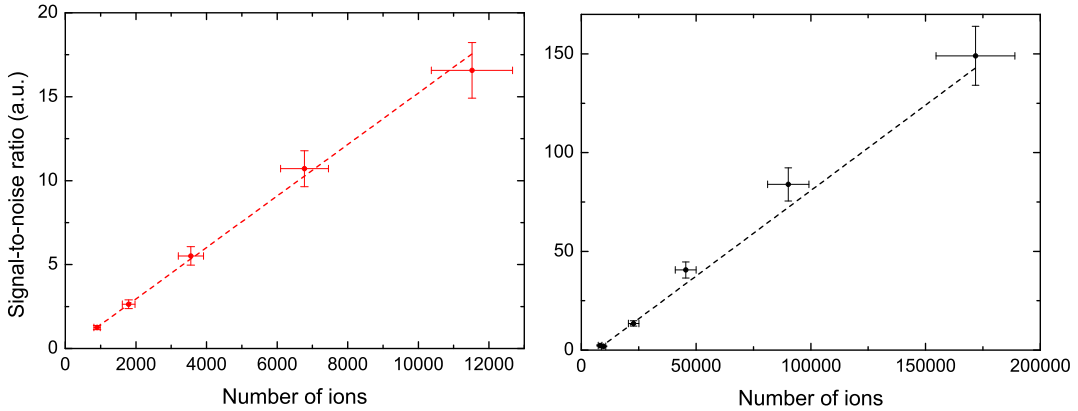


Figure 6.14: Relative amplitude of the FT-ICR signal for  ${}^6\text{Li}^+$  (left) and  ${}^7\text{Li}^+$  (right) as a function of the number of trapped ions. The linear fit is illustrated with a dashed line. An uncertainty of 10 % was added to both the relative amplitude and the number of ions.

cle. The ions were trapped in a 60 V potential well during 180 ms, and the injection and ejection time was set to be 200  $\mu\text{s}$ . In a first step ions were excited for 5 ms at their magnetron frequency, 770 Hz, with a  $0.2 \text{ V}_{pp}$  amplitude. Between the trapping of the ions and the magnetron excitation a delay of 4 ms was applied. The  ${}^6\text{Li}^+$  ions were excited for 15 ms at  $\nu_+$  with an amplitude of  $1.9 \text{ V}_{pp}$  and the  ${}^7\text{Li}^+$  ions were excited for 17 ms with an amplitude of  $1.2 \text{ V}_{pp}$ . The dashed lines in figure 6.14 show a linear fit of the data. The number of ions detected on the FC was corrected with the natural abundances of lithium ( ${}^6\text{Li}^+$  7.59% and  ${}^7\text{Li}^+$  92.41%) in order to calculate the amount of each of the ion species. One measured point in figure 6.14 corresponds to a certain heater current. As seen from figure 6.14, a detection limit of  $\approx 800$  ions was found for  ${}^6\text{Li}^+$ . In the case of  ${}^7\text{Li}^+$  we cannot present a proper detection limit measurement. The reason for that comes from the fact that the sensitivity limit of the Faraday cup charge amplifier is, in this case, reached before losing the ion signal (i.e., one still has a visible FT-ICR signal but is not possible to measure such small amount of ions with the charge amplifier).

From the measurements shown in this section one can get an idea about the needed minimum number of ions stored in the Penning trap to get still a detectable FT-ICR signal. In the range of interest for the KATRIN experiment an upper detection limit of  $\approx 6\,000$  ions for  ${}^4\text{He}^+$  and a lower detection limit of  $\approx 800$  ions for  ${}^6\text{Li}^+$  was achieved. In a lower range of frequencies (higher mass) a detection limit of  $\approx 1\,000$  ions was found for  $\text{H}_2\text{O}^+$  ions [64].

The detection limit at KATRIN will improve due to the cryogenic temperatures, which will result in a reduction in the thermal noise of the electronics and thus the sensitivity of the measurements will increase.

## 6.8 Mass measurements

The Penning trap used for all the tests presented here is not a high-precision measurement device as it does not contain correction electrodes. In order to determine the accuracy of the system being used as a Penning trap spectrometer mass measurements have been performed. The measurements were done using the surface ion source with a pellet containing  ${}^6\text{Li}^+$  and  ${}^7\text{Li}^+$  ions. As the mass for  ${}^7\text{Li}$  has been well determined at SMILETRAP [68],  ${}^7\text{Li}^+$  ions were used as reference ions and  ${}^6\text{Li}^+$  as the ion of interest. For performing this measurement first the ions were excited at their magnetron frequency, after that a dipole excitation was applied to both ion species simultaneously. A quadrupolar detection of the ion motion was done in order to observe the real cyclotron frequency  $\nu_c$ , which depends only on the charge-to-mass ratio of the ion species and the magnetic field at the ion position. The  $\nu_c$  frequency of both ion species was then measured simultaneously. By doing this one can assure that the magnetic field fluctuations that may appear during the measurement will affect both ion species the same way, meaning that for the final mass calculation the magnetic field term will cancel. One of the obtained spectra for both ion species is shown in figure 6.15. The ratio of the obtained amplitudes observed in figure 6.15 does not correspond to the natural abundance ratio of  ${}^6\text{Li}^+$  and  ${}^7\text{Li}^+$ . The amplitude of each of the ion species depends on the applied excitation amplitude, for these measurements the FT-ICR signal of both ion species was characterized in such a way that both species were visible and that the peaks were in a proper shape, without paying attention to the signals amplitudes.

A long term measurement of the center frequency of both ion species has been performed. The result of this long term measurement is shown in figure 6.16.

The mass of the ion of interest is calculated by measuring the real cyclotron frequencies of the two different ion species. One can calculate the frequency ratio of these two species using equation (2.1), obtaining  $R = \nu_{c,ref}/\nu_{c,ioi} = m_{ioi}/m_{ref}$ , for ions with the same charge states. For obtaining the atomic mass one has to correct this formula for the missing electrons, each of them with mass  $m_e$ , obtaining finally the expression:

$$m_{ioi} = \frac{\nu_{c,ref}}{\nu_{c,ioi}}(m_{ref} - m_e) + m_e, \quad (6.2)$$

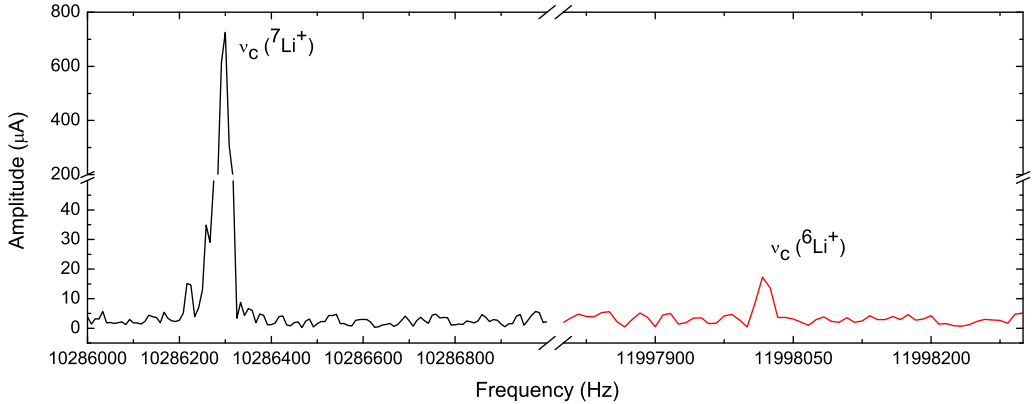


Figure 6.15: Spectrum showing the  $\nu_c$  frequency for both trapped ion species,  $^6\text{Li}^+$  and  $^7\text{Li}^+$ , using the quadrupolar detection method. For more details see text.

where the index *ref* refers to the reference ion,  $^7\text{Li}^+$  in our study, and the index *ioi* refers to the ion of interest,  $^6\text{Li}^+$  in our case. The electron mass  $m_e$  is  $5.485\,799\,094\,5(24) \times 10^{-4}$  u [69]. The  $^7\text{Li}$  atomic mass is  $7.016\,003\,425\,6(45)$  u [68]. By applying this formula to the data we obtained a mass value for  $^6\text{Li}$  of  $6.015\,140\,(5)(36)$  u. The first error shown in the obtained mass value corresponds to the statistical error. The second error shown refers to the systematic error. The systematic error was calculated taking into account the magnetic field inhomogeneities.

Comparing our result with the literature value of the  $^6\text{Li}$  mass which is  $6.015\,122\,795(16)$  u [65], one can conclude that the Penning trap system used in our studies has an accuracy of  $3 \times 10^{-6}$  which can be considered an acceptable result taking into account the limitations in the geometry of the used Penning trap and in the experimental setup itself, as well as that the measurement has been performed on an ion cloud and not on a single ion.

## 6.9 Residual gas analysis at cryogenic temperatures

Since contaminations inside the KATRIN beamline are a source of uncertainties it is a must that the Penning trap system itself is not outgassing and thus becoming a new source of uncertainties. To this end the materials were carefully chosen, see discussion of the Penning trap materials in section 5.4.

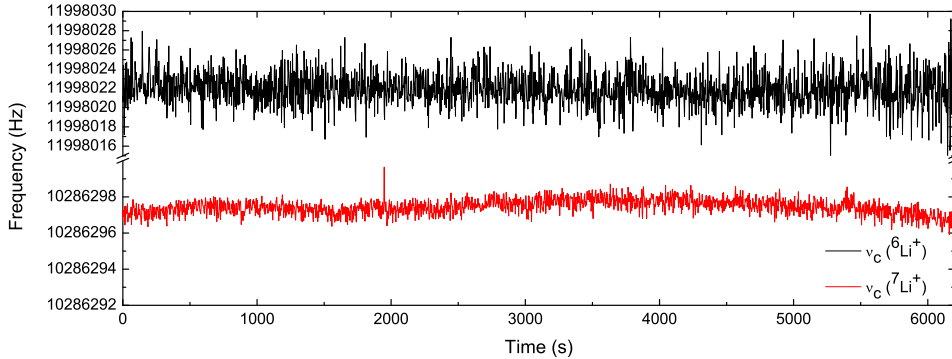


Figure 6.16: Long term measurement of the true cyclotron frequency  $\nu_c$  for  ${}^6\text{Li}^+$  and  ${}^7\text{Li}^+$  ions simultaneously. The ratio of these two frequencies is used for the  ${}^6\text{Li}^+$  mass determination. See text for details.

In order to check the outgassing produced by the trap and its electronics at cryogenic temperatures a cryogenic test setup, shown in figure 6.17, was design and built. The cryogenic setup consists mainly of a vacuum chamber where the Penning trap system was inserted, a commercial residual gas analyzer system used for the studies and a turbo molecular pump to create the vacuum.

A commercial rest gas analyzer, Spectra Satellite quadrupole mass spectrometer distributed by MKS [70], operating in the mass range from 0 to 100 u was used for these tests. The residual gas analyzer system consists of four main components: (1) An *ionizer* with ion optics is used to ionize the residual gas and transport it to the mass filter. (2) A *quadrupole filter* which separates the ion beam created by the ionizer according to their mass-to-charge ratio. (3) A *collector*, used for the ion current detection. (4) The ion current is amplified by the system electronics and then displayed by the *commercial software* installed on a laptop.

The Penning trap with the electronics attached to it was installed inside the vacuum chamber. Thus the materials inside the chamber were: the Al-Mg outer structure of the Penning trap, the goldplated copper electrodes, the PEEK spacers, all the needed screws for mounting one of the Penning traps and two electronic boards made out of FR4-type (glass fiber filled epoxy resin). The chamber was heated up to 110 °C in order to evaporate the water inside of it, during the heating period the pressure inside the chamber increases. After the heating is done and the chamber goes back to room temperature the pressure is expected to be reduced. Once this step is done and once the chamber was back to room temperature the Dewar was filled

## 76 Chapter 6: Results from the commissioning setup in Heidelberg

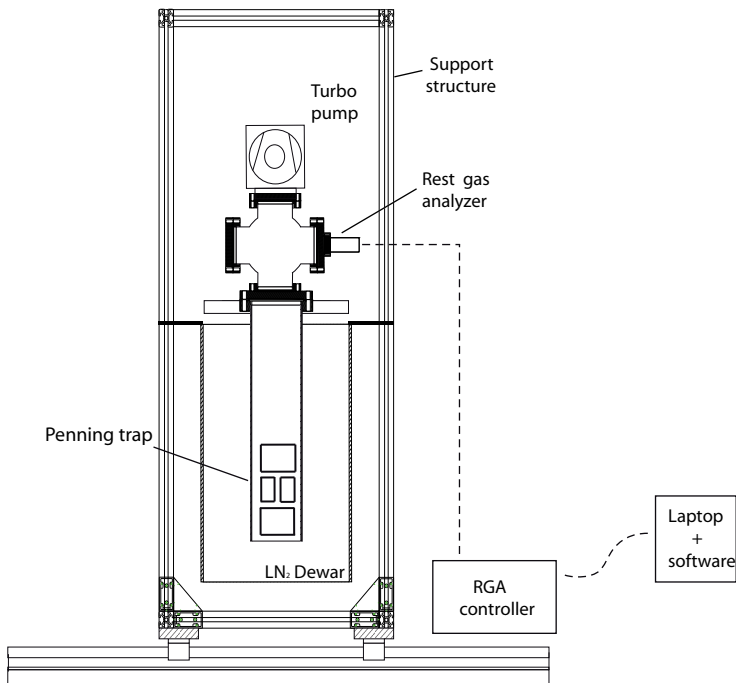


Figure 6.17: Scheme of the cryogenic setup used for the outgassing test of the Penning trap and its electronics. See text for details.

with liquid nitrogen and the cooling of the Penning trap system started. At the end of the cooling process with a final temperature of 77 K, a pressure bellow  $1 \times 10^{-8}$  mbar was reached.

Figure 6.18 shows the results of these tests for eight different gases. The plot shows the partial pressure for each of the gases inside the chamber as a function of time. At room temperature the major component that can be seen in the test is water, which is probably coming from the water on the air or the vacuum chamber walls. Three of the gases shown in the graph are named as hydrocarbons, these substances were not possible to be identified but are expected to be a sort of composition of carbon and hydrogen ions, basically something not harmful for our system. The biggest contribution on the outgassing test at cryogenic temperatures is coming from carbon dioxide which can come from the welding of the vacuum chamber itself. The step appearing for some of the gases at around 28 h is due to the existence of a small leak in the vacuum chamber. The step appears at the time when the upper flange of the chamber was covered by the liquid nitrogen.

According to the KATRIN vacuum experts the results show that the Penning trap system that will be installed in the KATRIN beamline is not producing any critical outgassing which should concern the KATRIN exper-

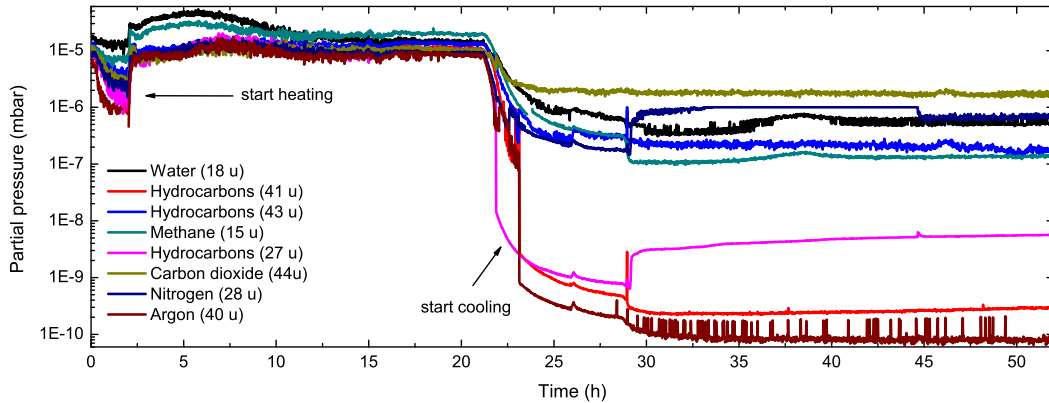


Figure 6.18: Results of the outgassing test of the Penning trap system and its electronics for eight different gases with different masses.

iment.

## 6.10 Conclusion

Within this chapter the characterization of the Penning trap system that will be installed in the KATRIN beamline was presented. The electronics used for the presented results was characterized showing an amplification of a factor of 6 for the preamplifier and a factor of 27 for the postamplifier. A voltage noise density of  $1 \text{ nV}/\text{Hz}^{1/2}$  was measured for the preamplifier in the range of frequencies of interest for the performed tests. The timing sequence and how to characterize an FT-ICR signal were discussed. The FT-ICR signal at  $\nu_+$  was studied as a function of the trapping voltage, by doing that one can calculate the magnetic field at the position of the trapped ions. The obtained value agreed very well with the one measured with the NMR probe and discussed in chapter 5.

The ion cloud loses its coherent motion after a certain time which is called coherence time. The coherence time was studied as a function of the excitation time and as a function of the pressure inside the vacuum chamber. Measurements at the pressures expected in the KATRIN beamline were done, which shows that it will still be possible to see an FT-ICR signal in these conditions. The selected-ion excitation and detection methods that will be used in the KATRIN experiment were tested at the MPIK setup by showing that several ion species can be detected simultaneously.

## **78 Chapter 6: Results from the commissioning setup in Heidelberg**

---

An important step in the characterization of the Penning trap system was the determination of the detection limit, which is the minimum number of ions needed in the trap in order to have a visible FT-ICR signal. These measurements will be of great help to the KATRIN experiment in order to determine an approximation of the number of trapped ions in each of the traps.

A mass measurement of  ${}^6\text{Li}$  was done using  ${}^7\text{Li}$  as mass reference in order to determine the accuracy of the Penning trap mass spectrometer. The relative uncertainty of the measured  ${}^6\text{Li}$  was  $3 \times 10^{-6}$  and the value agreed with the literature value. This accuracy can be considered an acceptable value taking into account that the used Penning trap system was not designed to be a high-precision device.

A residual gas analysis of the Penning trap and its electronics was done at cryogenic temperatures (77 K). To this purpose a commercial residual gas spectrometer was used. The results from these tests show no critical outgassing produced by the Penning trap system, as it was expected.

Several studies on the interaction of ions with one- and two-pulse (Ramsey) quadrupolar excitation fields were as well performed using this setup. These studies will be discussed in detail in the PhD thesis of Michael Heck [71].

# Chapter 7

## Future commissioning in KATRIN

The installation and on-line commissioning of the two Penning trap systems in the KATRIN beamline are planned to be done in the year 2012. An overview of this future commissioning is given in this chapter. The position of the traps in the beamline, the magnetic field at the trap position, a possible cable choice for the trap wiring and the detection electronics for the KATRIN project will be discussed.

### 7.1 Position of the traps

As it was already mentioned in chapter 4, the two Penning trap systems will be installed at the entrance and at the exit of the differential pumping section (DPS). These two traps will be installed at the center of two of the five tube segments composing the DPS (see figure 4.2 (left)). Each of these tube segments of the beamline has the geometry shown in figure 7.1, with a bellow in the center. The traps will be installed in the center of the tubes. The ring electrode of the Penning traps will be installed in the center of the bellow. The position of the Penning trap was chosen by taking into account the magnetic field profile along the DPS. The homogeneous region of the magnetic field provided by the superconducting coils coincides with the center of the bellows. Section 7.2 shows the measured magnetic field in one of the DPS modules.

The Penning trap geometry already explained in chapter 5 had to be slightly modified due to some issues only found when the DPS was delivered to the Karlsruhe Institute of Technology (KIT), where the KATRIN experiment is being installed and commissioned. As expected, the inner diameter of

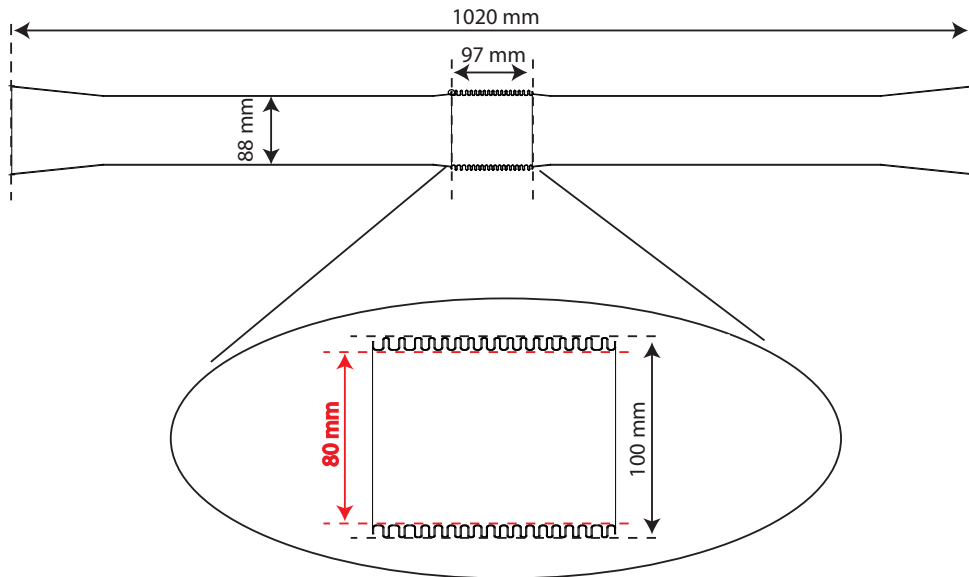


Figure 7.1: The upper figure shows one of the differential pumping section tubes, the bellow can be seen in the middle of it. The lower picture shows a zoom of the bellow with the dimensions labeled.

the DPS vacuum chambers was 88 mm. The same value was expected for the inner diameter in the bellow part. Instead, the inner diameter at the bellow position was found to be 80 mm. When the Penning traps were designed and constructed (middle 2007) the outer diameter was set to be 83 mm in order to fulfill the KATRIN beamline requirements, thus the new bellow diameter of 80 mm found after its delivery to the KIT (2010) created an inconsistency since the traps were not fitting at the desired positions.

In order to solve this problem the outer structure of the Penning trap was modified. This modification does not affect the results of the characterization shown in chapter 6 because the inner diameter of the trap, and thus the ring and the endcap electrodes, remain the same size. The Penning trap structure was modified in such a way that only the outer diameter is asymmetric. One third of the trap length has the original diameter (83 mm) while the other two thirds have a diameter of 79 mm, providing a reduced diameter to fit into the bellow. Figure 7.2 (up) shows the design of the new trap with the mentioned reduced diameter. By using this geometry the two thirds of the Penning trap with the reduced diameter will be placed inside the bellow and the rest will be fixed on the vacuum tube using feet. These feet are shown in figure 7.2 (down). Due to this reduction in diameter other small details had to be modified as well. In the part of the trap with larger diameter several

feet will be mounted in order to center the trap at the KATRIN beamline and avoid that it moves. The guidance of the electronics and voltage cables is implemented by following the grooves made in the PEEK spacers shown in figure 7.2 (down). At the moment of writing this thesis the Penning traps are being built at the MPIK mechanical workshop and they will be ready at the end of 2011. An asymmetric structure was already inserted inside the KATRIN beamline in order to test its viability. The structure fits as expected in the bellow and is sufficiently stable and centered (less than 1 mm off-center).

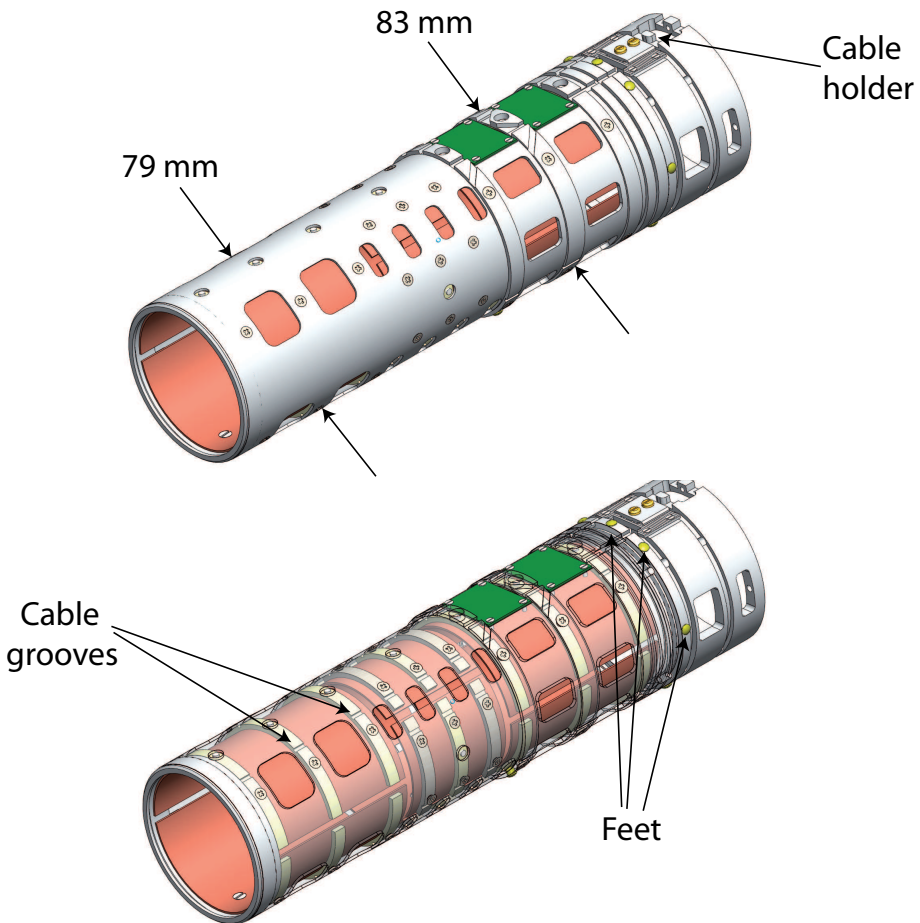


Figure 7.2: The upper drawing points out the two different diameters and the cable holder. The lower drawing shows the grooves for the cable guiding and the added feet for supporting the structure to the KATRIN beamline. Drawing courtesy of the MPIK construction workshop.

The position of the traps in the bellows may create some external source

of uncertainties. As the bellow will contract during the cooling down of the DPS, this may produce some misalignment in the trap position with respect to the magnetic field, producing frequency shifts which can impair the identification of different ion species. The bellow movements during the cooling down could also create forces into the trap cabling. In order to avoid that the cables disconnect or break due to this force a cable holder which clamps the cables (shown also in figure 7.2 (right)) was added.

## 7.2 Magnetic field at the DPS

The magnetic field created by one of the coils at the differential pumping section has been measured using a Hall probe. Up to now only the field provided by one of the coils has been measured but the same results are expected from the other coils since all of them have the same dimensions and characteristics. The results obtained from this magnetic field measurement are shown in figure 7.3 [72].

Figure 7.3 shows the measured magnetic field along the axis in one of the DPS modules. A value of around 5.2 T in the homogeneous region was measured. The inset in figure 7.3 depicts a zoom of the homogeneous region of the magnetic field, showing a homogeneity better than 0.01 % around the center of the module. In this homogeneous region, one of the Penning trap systems will be installed. One can conclude that the homogeneity and the strength of the field are sufficient for operating the Penning traps with the FT-ICR method since the magnetic field values are very similar to those used at the MPIK.

A long-term magnetic field measurement was also done using to this purpose an NMR probe. The magnetic field was measured for a period of 60 days and a decay in the magnetic field of 0.01 % was found [72]. From these results it is possible to conclude that the magnetic field at the DPS is stable enough for the Penning trap use and of course for the KATRIN data taking.

## 7.3 Cabling

For the off-line characterization of the Penning trap system at the MPIK setup the cabling for trapping, ion excitation and ion detection at the Penning trap was in a first approach implemented using copper cables with Teflon isolation. Due to the risk of corrosion of Teflon in the presence of tritium atoms [73], the use of the Teflon material is prohibited inside the KATRIN beamline. In order to find a suitable cable that accomplishes the

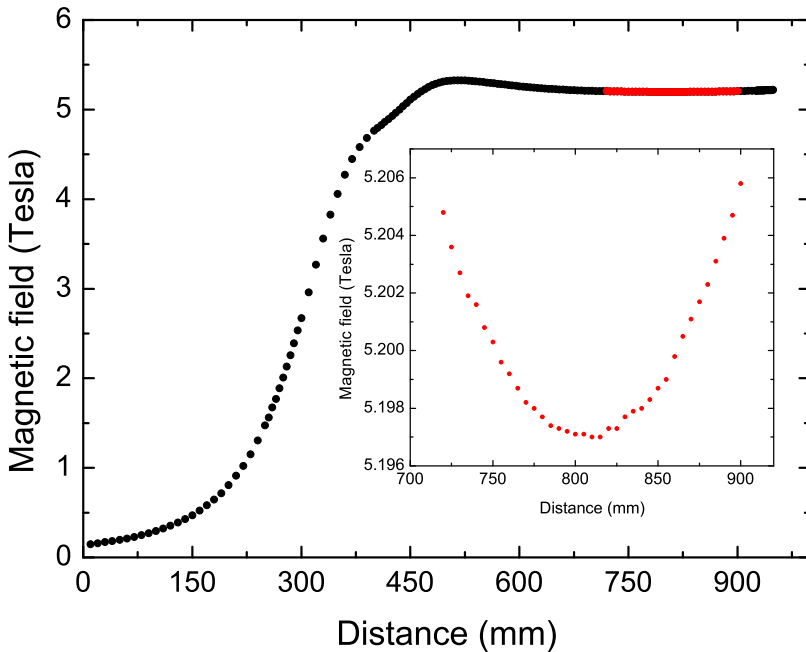


Figure 7.3: Magnetic field measured in one of the DPS modules showing a value of around 5.2 T in its homogeneous region. The inset of the figure shows a zoom of the region where one of the Penning traps will be installed [72].

KATRIN requirements, several Teflon-free cables were tested. The needed cable must be basically pick-up noise free, *i.e.* the cable must be well isolated and shielded to avoid that any external noise is picked up and the ion signal is disturbed.

A 50 Ohm impedance coaxial cable with a copper inner conductor and Kapton isolation from Draka Fileca [74] was tested and specified for its use for the traps wiring at KATRIN. The inner conductor of the cable has a diameter of 0.15 mm and the thickness of the cable is 1.14 mm. A transfer function test of the cable was done to prove that no reflections or signal attenuation occurs in the range of frequencies of interest for KATRIN. The transfer function measurement was done in a frequency range between 0 and 1 000 MHz at both 77 and 300 K temperature. Results for a cable of  $\approx 5$  m length are shown in figure 7.4 (left).

Large reflections in the cable are mostly observed at high frequencies, appearing at  $\approx 600$  MHz. In the range of interest for KATRIN, up to 100 MHz,

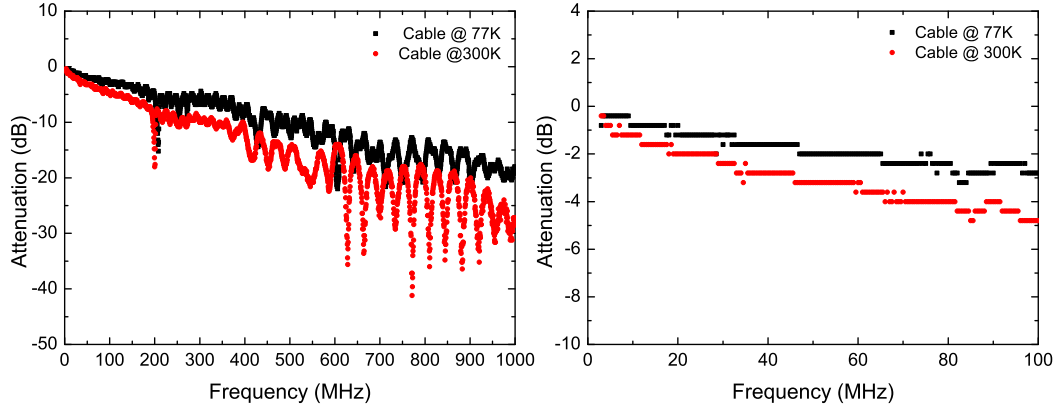


Figure 7.4: Transfer function of the  $\approx 5$  m coaxial cable from Draka Fileca. Left panel shows the transfer function from 0 to 1 000 MHz, reflections appear at  $\geq 600$  MHz. Right panel shows the same results as in the left panel but in the range of frequencies of interest for KATRIN, mainly from 0 to 100 MHz.

see figure 7.4 (right), the signal attenuation is rather low, down to -5 dBm at 300 K and to -3 dBm at 77 K, the operating temperature of the KATRIN beamline.

From this short studies one can conclude that the coaxial cable is a possibly good choice for the Penning trap cabling inside the KATRIN experiment and its used is recommended for the final commissioning.

## 7.4 Electronics

The amplifier system (pre- and postamplifiers) that will be used at the KATRIN experiment has the same characteristics as the one used for the tests presented in chapter 5. The preamplifiers will be used at cryogenic temperatures when installed in the KATRIN beamline, the tests of these preamplifiers at 77 K are presented in this section. The postamplifiers that will be used in KATRIN will exhibit the same features as the one used at the MPIK. Since these final postamplifiers are not existing yet, only a sketch of them and their specifications will be presented.

### 7.4.1 Preamplifier

The two preamplifier boards that will be used at KATRIN were tested at the MPIK in a cryogenic environment. Each of the amplifier boards has two

different channels. In this section only the results for one channel of one of the preamplifiers is presented. The same behavior is measured for the second channel.

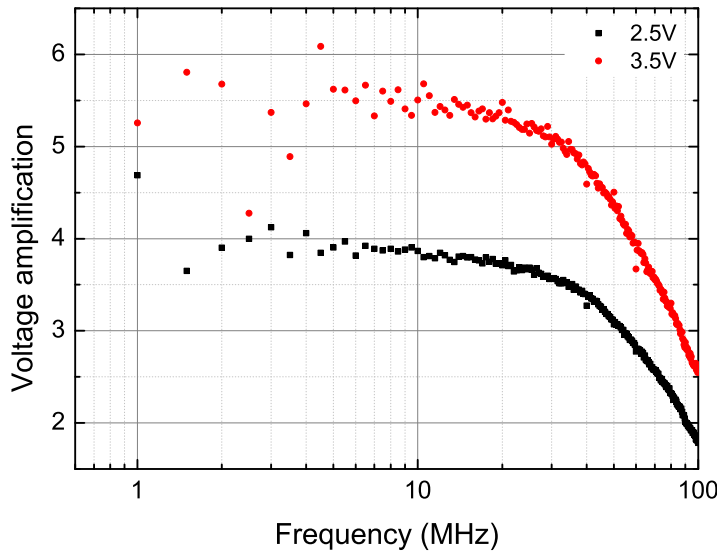


Figure 7.5: Amplification results for one of the KATRIN preamplifiers at 77 K. The amplification is shown for two different supply voltages. See text for details.

For the voltage amplification tests of the preamplifiers the measurements were done at two different supply voltages, namely 2.5 V and 3.5 V, since the final voltage that will be used at KATRIN has not been decided yet. Figure 7.5 shows the gain of one of the preamplifiers in a range of frequencies from 0 to 100 MHz for the two applied supply voltages. A voltage amplification of  $\approx 3.7$  for 2.5 V and  $\approx 5.5$  for 3.5 V between 1 and 30 MHz was measured. The obtained curves behave as expected and the preamplifiers will provide, together with the postamplifier, enough amplification for the induced image current of the trapped ions to have a visible FT-ICR signal.

Figure 7.6 shows the results of the noise tests performed for one of the KATRIN preamplifiers at 77 K. The left panel in figure 7.6 is the result for the voltage noise density as a function of frequency, showing a value of  $\approx 500 \text{ pV/Hz}^{1/2}$  around 10 MHz. The step appearing between 7 and 10 MHz is due to some external noise and not from the amplifier itself. Unfortunately it was not possible to identify and eliminate the source of the noise. The trend of the voltage noise density curve shows as expected a  $f^{-1/2}$  be-

havior. The current noise density as a function of the frequency is illustrated in the right panel, showing a value of  $\approx 50 \text{ fA}/\text{Hz}^{1/2}$  around 1 MHz. The current noise density curve shows a  $f^{1/2}$  behavior. The falling down behavior appearing around 3 MHz is due to a low pass filter inserted in front of the spectrum analyzer in order to avoid reflections at high frequencies. The noise measurement does not significantly change with the applied voltage, so only the results for one applied supply voltage (2.5 V) is shown.

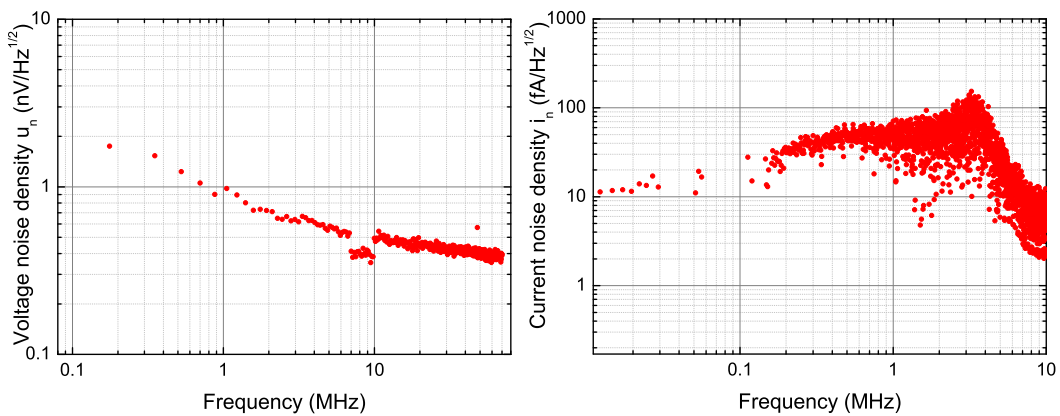


Figure 7.6: Noise test for one of the KATRIN preamplifiers at 77K. Left panel shows the voltage noise density as a function of frequency. Right panel shows the current noise density as a function of frequency.

### 7.4.2 Postamplifier

The two postamplifiers that will be used at the KATRIN experiment are still in development. Each of them will be installed in a CF-40 or CF-63 flange (the exact position is not decided yet). Each of those amplifiers will feature exactly the same characteristics as the one used at the MPIK and only its geometry will be modified in order to place them in a smaller flange than the one used at the MPIK setup.

The main characteristics of the postamplifiers are:

Frequency Range (-3 dB): 0.25 to 60 MHz

Voltage Amplification (w/o termination): typ.  $\times 100$

Power Amplification: 26 dB @ 5 MHz ( $50\Omega/50\Omega$ )

Input/Output Impedance:  $50\Omega$  nominally

Input Voltage Noise Density: typ.  $1.6 \text{ nV}/\sqrt{\text{Hz}}$  @ 5 MHz, 300 K

Number of channels: 2

A sketch of how the final postamplifier will be mounted in one of the DPS flanges is shown in figure 7.7. For a good grounding connection and to avoid grounding loops the amplifier will be placed in one of the DPS flanges. As the flange should also contain one feedthrough for the signal feeding and detection of the Penning trap, the amplifier will be placed in perpendicular to the flange, as shown in figure 7.7. An aluminum box will surround the post amplifier and the feedthrough to isolate them as much as possible from external noise. The completion of the postamplifiers construction will be done as soon as the size of the flanges where they will be installed is decided.

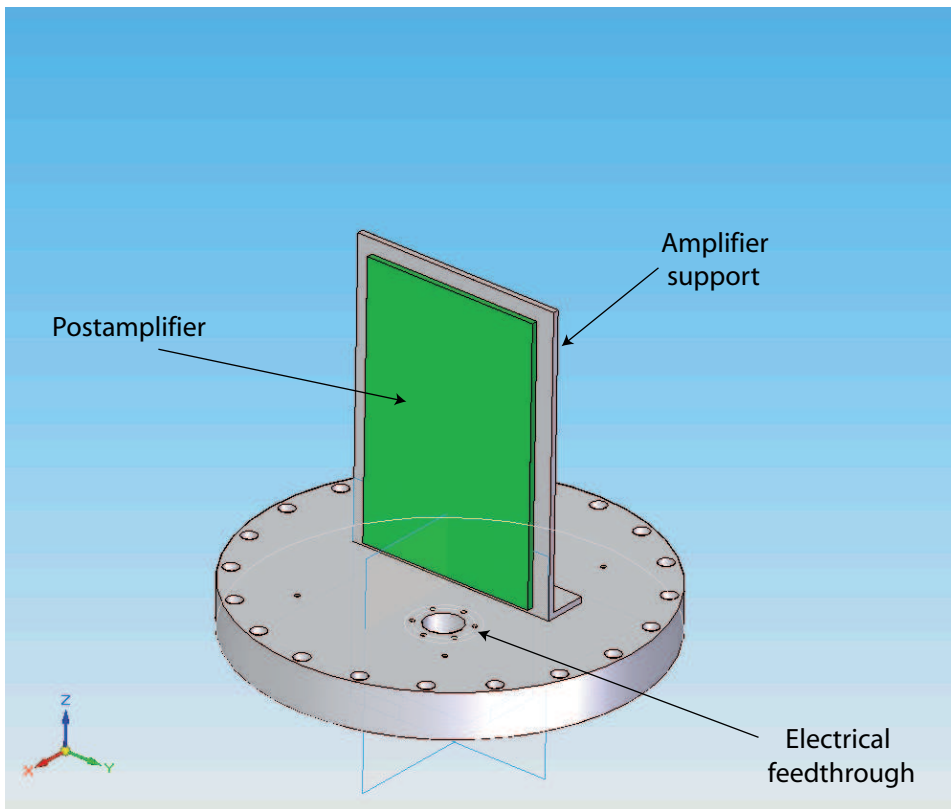


Figure 7.7: Design of the postamplifier geometry that will be used in KATRIN. Refer to text for more details.

## 7.5 Status and conclusion

Within this chapter a general perspective of the future Penning trap commissioning at the KATRIN beamline has been given. The position of the Penning traps inside the KATRIN beamline was shown. A modification of

the outer structures of the Penning traps was done in order to place them at the DPS bellow positions. The magnetic field of one of the DPS modules was measured by the KIT team. Results of the magnetic field at one of the traps positions reveals a magnetic field of  $\approx 5.2$  T at the center of the trap with a homogeneity of 100 ppm/10 mm<sup>2</sup>, fulfilling the requirements for FT-ICR detection.

Due to the possibility of corrosion of Teflon in the presence of tritium a Teflon-free cable must be used inside the KATRIN beamline. The transfer function of a coaxial cable with Kapton isolation was studied at both cryogenic and room temperature, in order to determine whether reflections or signal attenuation occurs. The results were satisfactory and one can conclude that the cable is suitable for its usage in KATRIN.

The cryogenic preamplifiers that will be used in KATRIN for the first stage amplification of the induced image current of the trapped ions were tested at liquid nitrogen temperature. The noise tests revealed a voltage noise density of 500 pV/Hz<sup>1/2</sup> around 10 MHz, which is sufficient for the planned applications. The postamplifiers that will be used in KATRIN are not yet developed. Therefore only their expected characteristics have been described.

The final commissioning of the Penning traps into the KATRIN beamline is planned to be done in 2012.

# Chapter 8

## Conclusion and outlook

Within this thesis the off-line characterization of a Penning trap system planned to be installed in the KArlsruhe TRItium Neutrino experiment (KATRIN) experiment has been presented. The KATRIN experiment is based on the tritium  $\beta$ -decay and will examine the shape of the  $\beta$  spectrum at the highest electron energies. A source of systematic uncertainty in the KATRIN experiment is the existence of ions and molecules created along the  $\beta$ -decay having a different  $\beta$ -decay endpoint than tritium, such as  $T_2^+$  and  $T_3^+$ . The reduction of contaminants in the KATRIN beamline will be done by using a differential and a cryogenic pumping system. The monitoring of the contaminations inside the KATRIN beamline before and after the pumping system is planned to be done by using two identical Penning trap spectrometers at two different positions of the KATRIN beamline. The off-line characterization of one of these Penning trap systems utilizing the broad-band Fourier Transform-Ion Cyclotron Resonance (FT-ICR) detection method has been performed at the Max-Planck-Institute for Nuclear Physics (MPIK) in Heidelberg. Results have been presented in this thesis.

A dedicated setup was built at the MPIK for the characterization of the Penning trap system. The characterized spectrometer is a 3-pole cylindrical Penning trap designed to fulfill the KATRIN requirements of fitting into the KATRIN beamline and not to interfere with the  $\beta$ -electrons. The most important component of the setup, besides of the tested trap, is the superconducting magnet. The magnetic field plot of the used magnet shows that it provides enough strength and stability to perform the desired tests.

A very important component of the tested Penning trap system is the electronic amplifiers needed to perform FT-ICR. Two set of amplifiers were tested and results were presented. One set of amplifiers is used at the MPIK setup. The other set of amplifiers will be used in the KATRIN experiment at cryogenic temperature (77 K). Both amplifier systems were tested and results

show that enough amplification is provided in the range of frequencies of interest.

A calculation of the magnetic field seen by the trapped ions was performed by changing the endcap voltage and measuring the center frequency of the ion response. The measurement was done with different ion species and the obtained values agreed with the magnetic field measured when using an NMR probe. Measuring the magnetic field using the trapped ions is one of the tests that will be performed at the KATRIN experiment to characterize the traps at their beamline position.

The coherent time of the trapped ion cloud was studied as a function of the excitation time and the rest gas pressure. The coherent time measurements at different pressures were done in order to determine the signal decay due to collisions with rest gas particles. The expected pressures inside the KATRIN beamline at the different positions of the traps were investigated. Results assure that at the pressure conditions inside the KATRIN beamline the operation of the traps and application of the FT-ICR detection technique is possible.

The test setup built at the MPIK gave us the possibility of combining the FT-ICR detection method with the time-of-flight (TOF) detection method. By doing that is possible to find a relation between the amplitude of the induced image current and the number of trapped ions by counting them with either a Faraday cup or a microchannel-plate detector. This measurement will not be possible to be done at the KATRIN beamline since it will not be possible to install a detector for counting the trapped particles. Measurements with different ion species were done in order to find out the trap detection limit, *i.e.* the minimum number of ions needed in the trap in order to have a visible FT-ICR signal. As an example, a detection limit for  ${}^6\text{Li}^+$  of about 800 ions was measured.

The Penning traps that will be installed in KATRIN were not designed as devices for high-precision mass measurements. In order determine how precise is the tested trap, a mass measurement was done. An accuracy of  $3 \times 10^{-6}$  was found when measuring the  ${}^6\text{Li}$  mass and using  ${}^7\text{Li}$  as a reference mass. This accuracy can be considered an acceptable value taking into account the frequency shifts produced by the electric field inhomogeneities due to the trap geometry as well as ion-ion interactions.

After the tests performed and presented along this work, it can be conclude that the Penning trap systems fulfill the KATRIN requirements and their installation in KATRIN is possible. Since the commissioning of the beamline section where the traps will be installed is still in progress at the Karlsruhe Institute of Technology, the installation of the Penning traps will not be done until probably the middle of 2012. Until then, the characteri-

zation of the Penning trap system will continue at the MPIK. The resolving power of the Penning trap system and the determination of the space charge limit, among others, are some of the tests that will be performed by a new diploma student at the MPIK.



# Bibliography

- [1] W. Pauli. *Open Letter to Radioactive Persons* (1930).
- [2] C. Cowan, F. Reines, F. Harrison, H. Kruse, A. McGuire. *Detection of the Free Neutrino: a Confirmation.* Science, **124**, (1956) 103–104.
- [3] J. Sakurai. *Modern quantum mechanics.* Reading, MA: Addison Wesley,— c1985, edited by Tuan, San Fu, **1**.
- [4] E. Gawiser, J. Silk. *Extracting primordial density fluctuations.* Science, **280**, (1998) 1405.
- [5] B. Pontecorvo. *Mesonium and antimesonium.* Zhur. Eksptl'. i Teoret. Fiz., **33**.
- [6] Y. Fukuda, T. Hayakawa, E. Ichihara, K. Inoue, K. Ishihara, H. Ishino, Y. Itow, T. Kajita, J. Kameda, S. Kasuga, *et al.* *Evidence for oscillation of atmospheric neutrinos.* Phys. Rev. Lett., **81**, (1998) 1562–1567.
- [7] Q. Ahmad, R. Allen, T. Andersen, J. Anglin, G. Bühler, J. Barton, E. Beier, M. Bercovitch, J. Bigu, S. Biller, *et al.* *Measurement of the Rate of  $\nu_e + d \rightarrow p + p + e^-$  Interactions Produced by  $^8B$  Solar Neutrinos at the Sudbury Neutrino Observatory.* Phys. Rev. Lett., **87**, (2001) 71301.
- [8] Q. Ahmad, *et al.* *SNO Collaboration.* Phys. Rev. Lett, **89**, (2002) 89.
- [9] E. Fermi. *An attempt of a theory of beta radiation.* Z. phys, **88**, (1934) 161.
- [10] E. W. Otten, C. Weinheimer. *Neutrino mass limit from tritium  $\beta$ -decay.* Rep. Prog. Phys., **71**, (2008) 086201 (36pp).
- [11] J. Angrik, T. Armbrust, A. Beglarian, U. Besserer, J. Blümer, J. Bonn, R. Carr, B. Bornschein, L. Bornschein, T. Burritt, *et al.* *KATRIN Design Report 2004.* Wissenschaftliche Berichte FZKA, **7090**.

- [12] R. Van Dyck Jr, D. Farnham, P. Schwinberg. *Tritium–helium-3 mass difference using the Penning trap mass spectroscopy*. Phys. Rev. Lett., **70**, (1993) 2888–2891.
- [13] S. Nagy, T. Fritioff, M. Björkhage, I. Bergström, R. Schuch. *On the Q-value of the tritium beta-decay*. Europhys. Lett., **74**, (2006) 404–410.
- [14] D. Pinegar, S. Zafonte, R. Van Dyck. *The UW-PTMS*. Hyperfine Interact., **174**, (2007) 47–53.
- [15] C. Diehl, K. Blaum, M. Höcker, J. Ketter, D. Pinegar, S. Streubel, R. Van Dyck. *Progress with the MPIK/UW-PTMS in Heidelberg*. Hyperfine Interact., pages 1–10.
- [16] C. Kraus, B. Bornschein, L. Bornschein, J. Bonn, B. Flatt, A. Kovalik, B. Ostrick, E. Otten, J. Schall, T. Thummller, *et al.* *Final results from phase II of the Mainz neutrino mass searchin tritium decay*. The European Physical Journal C-Particles and Fields, **40**, (2005) 447–468.
- [17] V. Lobashev, V. Aseev, A. Belesev, A. Berlev, E. Geraskin, A. Golubev, O. Kazachenko, Y. Kuznetsov, R. Ostroumov, L. Rivkis, *et al.* *Direct search for neutrino mass and anomaly in the tritium beta-spectrum: Status of Troitsk neutrino mass experiment*. Nuclear Physics B-Proceedings Supplements, **91**, (2001) 280–286.
- [18] K. Blaum. *High-accuracy mass spectrometry with stored ions*. Phys. Rep., **425**, (2006) 1–78.
- [19] K. Blaum, Y. Novikov, G. Werth. *Penning traps as a versatile tool for precise experiments in fundamental physics*. Contemporary Physics, **51**, (2010) 149–175.
- [20] L. Brown, G. Gabrielse. *Geonium theory: Physics of a single electron or ion in a Penning trap*. Reviews of Modern Physics, **58**, (1986) 233–311.
- [21] H. Dehmelt. *Experiments with an isolated subatomic particle at rest*. Reviews of modern physics, **62**, (1990) 525.
- [22] A. Kruithof, F. Penning. *Determination of the Townsend ionization coefficient  $\alpha$  for pure argon*. Physica, **3**, (1936) 515–533. ISSN 0031-8914.
- [23] W. Paul. *Electromagnetic traps for charged and neutral particles*. Reviews of modern physics, **62**, (1990) 531.

- [24] M. Mukherjee, D. Beck, K. Blaum, G. Bollen, J. Dilling, S. George, F. Herfurth, A. Herlert, A. Kellerbauer, H. Kluge, *et al.* *ISOLTRAP: An on-line Penning trap for mass spectrometry on short-lived nuclides.* The European Physical Journal A-Hadrons and Nuclei, **35**, (2008) 1–29.
- [25] M. Block, D. Ackermann, K. Blaum, C. Droese, M. Dworschak, S. Eliseev, T. Fleckenstein, E. Haettner, F. Herfurth, F. Hessberger, *et al.* *Direct mass measurements above uranium bridge the gap to the island of stability.* Nature, **463**, (2010) 785–788.
- [26] J. Ketelaer, J. Kramer, D. Beck, K. Blaum, M. Block, K. Eberhardt, G. Eitel, R. Ferrer, C. Geppert, S. George, *et al.* *TRIGA-SPEC: A setup for mass spectrometry and laser spectroscopy at the research reactor TRIGA Mainz.* Nucl. Instrum. Methods Phys. Res., Sect. A, **594**, (2008) 162–177.
- [27] P. Dawson. *Quadrupole Mass Spectrometry and Its Applications.* Amer Inst of Physics (1995).
- [28] L. Brown, G. Gabrielse. *Precision spectroscopy of a charged particle in an imperfect Penning trap.* Physical Review A, **25**, (1982) 2423–2425.
- [29] P. Anderson. *Theory of Flux Creep in Hard Superconductors.* Phys. Rev. Lett., **9**, (1962) 309–311.
- [30] P. Anderson, Y. Kim. *Hard superconductivity: theory of the motion of Abrikosov flux lines.* Reviews of Modern Physics, **36**, (1964) 39–43.
- [31] D. J. Wineland, H. G. Dehmelt. *Principles of the stored ion calorimeter.* J. Appl. Phys., **46**, (1975) 919–930.
- [32] H. Hasse, S. Becker, G. Dietrich, N. Klisch, H. Kluge, M. Lindinger, K. Lützenkirchen, L. Schweikhard, J. Ziegler. *External-ion accumulation in a Penning trap with quadrupole excitation assisted buffer gas cooling.* Int. J. Mass Spectrom., **132**, (1994) 181–191.
- [33] A. Marshall, M. Comisarow. *Fourier Transform Ion Cyclotron Resonance (FT-ICR) Spectroscopy.* Chem. Phys. Lett, **25**, (1974) 282–283.
- [34] M. Comisarow, A. Marshall. *The early development of Fourier transform ion cyclotron resonance (FT-ICR) spectroscopy.* J. Mass Spectrom., **31**, (1996) 581–5.
- [35] M. Comisarow, A. Marshall. *Fourier transform ion cyclotron resonance spectroscopy.* Chem. Phys. Lett., **25**, (1974) 282–283. ISSN 0009-2614.

- [36] M. Comisarow, A. Marshall. *Frequency-sweep fourier transform ion cyclotron resonance spectroscopy*. Chem. Phys. Lett., **26**, (1974) 489–490. ISSN 0009-2614.
- [37] A. Marshall, C. Hendrickson, G. Jackson. *Fourier transform ion cyclotron resonance mass spectrometry: a primer*. Mass Spectrom. Rev, **17**, (1998) 1–35.
- [38] L. Chen, T. C. L. Wang, T. L. Ricca, A. G. Marshall. *Phase-modulated stored waveform inverse Fourier transform excitation for trapped ion mass spectrometry*. Anal. Chem., **59**, (1987) 449–454.
- [39] A. Marshall, T. Wang, T. Ricca. *Tailored excitation for Fourier transform ion cyclotron mass spectrometry*. J. Am. Chem. Soc., **107**, (1985) 7893–7897. ISSN 0002-7863.
- [40] G. Savard, S. Becker, G. Bollen, H.-J. Kluge, R. Moore, T. Otto, L. Schweikhard, H. Stolzenberg, U. Wiess. *A new cooling technique for heavy ions in a Penning trap*. Phys. Lett. A, **158**, (1991) 247–252.
- [41] P. Ghosh, P. Ghosh. *Ion traps*. Clarendon press (1995).
- [42] A. Griffin, D. Snoke, S. Stringari. *Bose-Einstein Condensation*. Cambridge Univ Pr (1996).
- [43] W. Ketterle, N. Van Druten. *Evaporative cooling of atoms*. Adv. At. Mol. Opt. Phys, **37**, (1996) 127–155.
- [44] I. Bergström, C. Carlberg, T. Fritioff, G. Douyset, J. Schönfelder, R. Schuch. *SMILETRAP-A Penning trap facility for precision mass measurements using highly charged ions*. Nucl. Instrum. Methods Phys. Res., Sect. A, **487**, (2002) 618 – 651. ISSN 0168-9002.
- [45] M. Hobein, A. Solders, M. Suhonen, Y. Liu, R. Schuch. *Evaporative Cooling and Coherent Axial Oscillations of Highly Charged Ions in a Penning Trap*. Phys. Rev. Lett., **106**, (2011) 013002.
- [46] M. König, G. Bollen, H. Kluge, T. Otto, J. Szerypo. *Quadrupole excitation of stored ion motion at the true cyclotron frequency*. Int. J. Mass Spectrom., **142**, (1995) 95–116.
- [47] G. Gräff, H. Kalinowsky, J. Traut. *A direct determination of the proton electron mass ratio*. Zeitschrift für Physik A Hadrons and Nuclei, **297**, (1980) 35–39.

- [48] S. Guan, A. Marshall. *Ion traps for Fourier transform ion cyclotron resonance mass spectrometry: principles and design of geometric and electric configurations.* Int. J. Mass Spectrom., **146**, (1995) 261–296.
- [49] A. Picard, H. Backe, H. Barth, J. Bonn, B. Degen, T. Edling, R. Haid, A. Hermanni, P. Leiderer, T. Loeken, *et al.* *A solenoid retarding spectrometer with high resolution and transmission for keV electrons.* Nuclear Instruments and Methods in Physics Research Section B, **63**, (1992) 345–358.
- [50] V. Lobashev, P. Spivak, I. Preprint. *P-0291 (Moscow, 1983).* Nucl. Instr. Meth. A, **240**, (1985) 305.
- [51] A. Windberger. *Dipl. Thesis. Berechnungen und Simulationen zum Verhalten von Ionen in der differenziellen Pumpstrecke des KATRIN-Experiments.* Karlsruhe Institute of Technology (2011).
- [52] F. Glueck. *Private communication.*
- [53] I. Rabi, J. Zacharias, S. Millman, P. Kusch. *A new method of measuring nuclear magnetic moment.* Physical Review, **53**, (1938) 318–318.
- [54] E. Ramsden. *Hall-effect sensors: theory and applications.* Elsevier/Newnes (2006).
- [55] P. Anderson. *Theory of flux creep in hard superconductors.* Phys. Rev. Lett., **9**, (1962) 309–311.
- [56] S. Lukic, B. Bornschein, G. Drexlin, F. Glueck, O. Kazachenko, M. Schoeppner, C. Weinheimer, M. Zoll. *Ion source for tests of ion behavior in the Karlsruhe tritium neutrino experiment beam line.* Rev. Sci. Instrum., **82**, (2011) 3303. ISSN 0034-6748.
- [57] H. Iwabuchi, M. Nomura, K. Iio, Y. Fujii, T. Suzuki. *Surface ionization mechanism of alkali halides.* Vacuum, **47**, (1996) 501–504.
- [58] *Axial molecular beam ionizer user manual.* ABB Automation Inc. Analytical division - Extrel.
- [59] G. Gabrielse, L. Haarsma, S. Rolston. *Open-endcap Penning traps for high precision experiments.* Int. J. Mass Spectrom., **88**, (1989) 319–332.
- [60] G. Gabrielse, F. Mackintosh. *Cylindrical Penning traps with orthogonalized anharmonicity compensation.* Int. J. Mass Spectrom., **57**, (1984) 1–17.

- [61] J. Wiza. *Microchannel plate detectors*. Nucl. Instrum. Methods, **162**, (1979) 587–601.
- [62] R. Ferrer. *PhD. Thesis. Mass measurements on neutron-deficient nuclides at SHIPTRAP and commissioning of a cryogenic narrow-band FT-ICR mass spectrometer*. Johannes Gutenberg University Mainz (2007).
- [63] <http://www.sciner.com/MCP/MCP.htm>.
- [64] M. Ubieto-Díaz, D. Rodriguez, S. Lukic, S. Nagy, S. Stahl, K. Blaum. *A broad-band FT-ICR Penning trap system for KATRIN*. Int. J. Mass Spectrom., **288**, (2009) 1–5.
- [65] G. Audi, A. Wapstra, C. Thibaulta. *The AME2003 atomic mass evaluation*. Nucl. Phys. A, **729**, (2003) 337–676.
- [66] M. Heck, K. Blaum, R. Cakirli, D. Rodríguez, L. Schweikhard, S. Stahl, M. Ubieto-Díaz. *Dipolar and quadrupolar detection using an FT-ICR MS setup at the MPIK Heidelberg*. Hyperfine Interact., pages 1–9.
- [67] D. Rodríguez, K. Blaum, R. Cakirli, M. Heck, L. Schweikhard, S. Stahl, M. Ubieto-Díaz. *Broad-Band FT-ICR MS for the Penning-Trap Mass Spectrometer MATS*. In *AIP Conference Proceedings*, volume 1265, page 483 (2010).
- [68] S. Nagy, T. Fritioff, M. Suhonen, R. Schuch, K. Blaum, M. Björkhage, I. Bergström. *New Mass Value for  $^7\text{Li}$* . Phys. Rev. Lett., **96**, (2006) 163004.
- [69] P. Mohr, B. Taylor. *CODATA recommended values of the fundamental physical constants: 2002*. Reviews of Modern Physics, **77**, (2005) 1.
- [70] *Spectra Satellite user manual*. MKS Spectra Products.
- [71] M. Heck, K. Blaum, R. Cakirli, M. Kretzschmar, G. Marx, D. Rodríguez, L. Schweikhard, S. Stahl, M. Ubieto-Díaz. *One- and two-pulse quadrupolar excitation schemes investigated with FT-ICR detection*. Applied Physics B.
- [72] W. Gil, *et al.* *Status of the electron transport and tritium pumping sections for KATRIN*. In preparation.
- [73] G. Frankel. *Pitting corrosion of metals: A review of the critical factors*. J. Electrochem. Soc., **145**, (1998) 2186–2198.

[74] <http://www.draka-fileca.fr/>.



# And the Oscar goes to...

At this point comes one of the most important parts of the thesis and the only one that some people will ever read...the acknowledgments!



First of all (see figure above) I would like to thank Klaus Blaum for the confidence placed on me over the years of my thesis. And for all the support given in all possible aspects.

Also thanks to Wolfgang Quint for accepting being the second corrector of this thesis.

As external collaborators I would like to mention the help provided by Lutz Schweikhard, Stefan Stahl and Daniel Rodriguez, all the time you have spent with us in the lab was of great help. Also thanks to Daniel for hosting me during several weeks at the University of Granada.

To Michi, because I cannot think of a better lab partner. Sharing all this time with you was great. Also to Burcu, because all her questions always made me think and improve.

Thanks to Tommi, Jochen, Julia and Christine for the corrections and translations, respectively.

Beside of the working friends I also want to mention the people I usually hang out with. Emma and Eva, for the cigarettes, the coffees and the week-

ends...there are still more to come! To Mikhail, for all the beers, cigarettes and conversations shared in a warm bench watching the snow fall. And of course to Michael, for being there even when he was not around...and also thanks for not talking too much about your trip to Indonesia. Here I want to make a special mention to Martin and Hermine for several reasons, but especially because they helped much more than they can imagine during the hard moments this year.

Por supuesto a mis padres y a mis hermanos, a los que quiero y sin los que no habría llegado hasta aquí.

Thanks to all those I do not mention above. It is not that I forgot some people, but I just do no think that the acknowledgments should be longer than the thesis itself.

And finally, I would like to end in a more serious note. I want to dedicate this thesis and all the time and effort invested in it, to the memory of a friend who sometimes was more present in my thoughts than the sentences I was writing, David Pinegar: an exceptional person, worth knowing. I feel lucky that I ever met him, spent time together with him and got to know him while he was in Heidelberg. I will always remember you, boy!